NAVAL POSTGRADUATE SCHOOL
Monterey, California

AD-A224 118

THESIS

NUMERICAL PULSE PROPAGATION STUDIES
USING TWO CLASSICAL OCEAN WAVEGUIDE MODELS

by

Marinos P. Markopoulos

December 1989

Thesis Advisor: Lawrence J. Ziomek

Approved for public release; distribution is unlimited

90 07 17 031

REPORT DOCUMENTATION PAGE

1a. REPORT SECURITY CLASSIFICATION UNCLASSIFIED			1b. RESTRICTIVE MARKINGS			
2a. SECURITY CLASSIFICATION AUTHORITY			3. DISTRIBUTION/AVAILABILITY OF REPORT Approved for public release; distribution is unlimited			
2b. DECLASSIFICATION/DOWNGRADING SCHEDULE						
4. PERFORMING ORGANIZATION REPORT NUMBER(S)			5. MONITORING ORGANIZATION REPORT NUMBER(S)			
6a. NAME OF PERFORMING ORGANIZATION Naval Postgraduate School	6b. OFFICE SYMBOL (If applicable) 62		7a. NAME OF MONITORING ORGANIZATION Naval Postgraduate School			
6c. ADDRESS (City, State, and ZIP Code) Monterey, California 93943-5000			7b. ADDRESS (City, State, and ZIP Code) Monterey, California 93943-5000			
8a. NAME OF FUNDING/SPONSORING ORGANIZATION	8b. OFFICE SYMBOL (If applicable)		9. PROCUREMENT INSTRUMENT IDENTIFICATION NUMBER			
8c. ADDRESS (City, State, and ZIP Code)			10. SOURCE OF FUNDING NUMBERS			
			PROGRAM ELEMENT NO	PROJECT NO.	TASK NO	WORK UNIT ACCESSION NO

11. TITLE (Include Security Classification) NUMERICAL PULSE PROPAGATION STUDIES USING TWO CLASSICAL OCEAN WAVEGUIDE MODELS

12. PERSONAL AUTHOR(S) MARKOPOULOS, Marinos P.

13a. TYPE OF REPORT Master's Thesis	13b. TIME COVERED FROM _____ TO _____	14. DATE OF REPORT (Year, Month, Day) 1989 December	15. PAGE COUNT 90

16. SUPPLEMENTARY NOTATION The views expressed in this thesis are those of the author and do not reflect the official policy or position of the Department of Defense or the US Government.

17	COSATI CODES		18. SUBJECT TERMS (Continue on reverse if necessary and identify by block number)
FIELD	GROUP	SUB-GROUP	Normal modes; pulse propagation in shallow water;
			rigid and fluid bottom ocean waveguide models

19. ABSTRACT (Continue on reverse if necessary and identify by block number)

Numerical pulse propagation studies using two classical ocean waveguide models are performed. The first model is a pressure-release surface with a rigid bottom. The second model is a pressure-release surface with a fluid bottom. The analysis of the two models is based on normal mode theory assuming a constant speed of sound in the ocean. The magnitude and phase of the complex acoustic pressure field as a function of frequency is calculated across a planar array of hydrophones. The time-domain output electrical pulse from the center element in the array is also computed. The computer simulation results for the two models are compared and discussed. Keywords: wave propagation; ocean surface; hydrophones; ocean bottom; equations of motion. (CR)

20. DISTRIBUTION/AVAILABILITY OF ABSTRACT		21. ABSTRACT SECURITY CLASSIFICATION
☒ UNCLASSIFIED/UNLIMITED ☐ SAME AS RPT ☐ DTIC USERS		UNCLASSIFIED
22a. NAME OF RESPONSIBLE INDIVIDUAL ZIOMEK, Lawrence J.	22b. TELEPHONE (Include Area Code) 408-646-3206	22c. OFFICE SYMBOL 62Zm

i

thesis

Numerical Pulse Propagation Studies using Two Classical Ocean Waveguide Models

by

Marinos P. Markopoulos
Lieutenant, Hellenic Navy
B.S, Hellenic Naval Academy, 1980

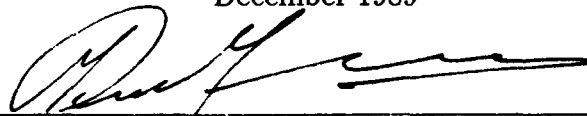Submitted in partial fulfillment of the
requirements for the degree of

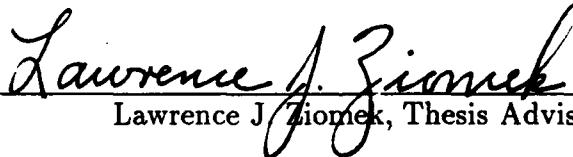MASTER OF SCIENCE IN ELECTRICAL ENGINEERING

from the

NAVAL POSTGRADUATE SCHOOL
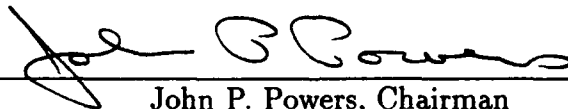
December 1989

Author: _____
Marinos P. Markopoulos

Approved by: _____
Lawrence J. Ziomek, Thesis Advisor

_____
Hung-Mou Lee, Second Reader

_____
John P. Powers, Chairman
Department of Electrical and Computer Engineering

ABSTRACT

Numerical pulse propagation studies using two classical ocean waveguide models are performed. The first model is a pressure-release surface with a rigid bottom. The second model is a pressure-release surface with a fluid bottom. The analysis of the two models is based on normal mode theory assuming a constant speed of sound in the ocean. The magnitude and phase of the complex acoustic pressure field as a function of frequency is calculated across a planar array of hydrophones. The time-domain output electrical pulse from the center element in the array is also computed. The computer simulation results for the two models are compared and discussed.

Accession For	
NTIS GRA&I	☒
DTIC TAB	☐
Unannounced	☐
Justification	

| By |
| Distribution/ |

Availability Codes	
	Avail and/or
Dist	Special
A-1	

TABLE OF CONTENTS

LIST OF TABLES

LIST OF FIGURES

ACKNOWLEDGMENT

I. INTRODUCTION

In this thesis two classical ocean waveguide models are examined and compared in order to draw conclusions concerning their differences. The two models that are examined are the following:

a. pressure-release surface with a rigid bottom, and

b. pressure-release surface with a fluid bottom.

It is well known that the first model (i.e., the rigid bottom model) is not a realistic one. Although the assumption of a pressure-release surface is valid, the assumption of a rigid bottom is not. Therefore, the main purpose of this thesis is to verify how differently this model performs compared to the second one (i.e., the fluid bottom model) which is theoretically a more realistic model. The complete theoretical analysis of these two models is well known and is presented in detail, for example, in Refs. 1, 2, or 3. Based on these references, an overview or sur . ¬y of the analytical expressions and relations used in the computer simulation program is included in Chapter II. Chapter II provides the necessary information and theoretical background on the way the waveguide models are approached and implemented in the computer program. Discussion concerning the way some problems encountered during the implementation of the models have been resolved is also included in Chapter II.

In order to be able to compare the two models and to decide on the effectiveness of each one, the models are examined under a relatively wide range of different cases. The models are tested for various transmitted signals, that is, Hamming-envelope and rectangular-envelope continuous wave (CW) and linear-frequency-modulated (LFM) pulses. The location of the receiver is varied also, that is, the receiver is located at different ranges from the source (short-range and long-range) and also at differ-

1

ent depths (above and below the source). The source is an omnidirectional point source, located at the rectangular coordinates $(0, 0, z_0)$ where z_0 is the depth. The receiver used for all the investigated cases is a 9x9 planar array of point elements (hydrophones), where the center element has the coordinates (x_R, y_R, z_R).

The computer simulation results for each model and for the various cases are presented and analyzed in Chapter III. The computer simulation results which are used in order to compare the two models are (i) the resulting output time-domain electrical pulse from the center element in the receive array and (ii) the characteristics of the complex acoustic pressure field (magnitude and phase as a function of frequency at each point of the field) when various input electrical signals at the source are transmitted through each model. The benefit of having these output results accurately and correctly calculated is that they can directly support studies in the area of target localization (i.e., estimating the range and the depth of the source) based on matched-field processing techniques [e.g., see Refs. 4 and 5].

The two models are compared based on the computer simulation results and the differences between them and some concluding remarks are included in Chapter IV.

II. TWO CLASSICAL OCEAN WAVEGUIDE MODELS

In this chapter the two classical ocean waveguide models are presented and explained from a theoretical point of view. A simple ocean waveguide model is illustrated in Fig. 2.1. Note that the ocean surface and bottom are assumed to be flat.

The notation used for the presentation of the models is as follows:

Medium I: Air

Medium II: Sea Water

Medium III: Ocean Bottom

ρ_i, i=1,2,3: the constant densities $\left(\frac{kg}{m^3}\right)$ of the three fluid media.

c_i, i=1,2,3: the constant speeds of sound $\left(\frac{m}{sec}\right)$ of the three fluid media.

$\rho_1 c_1$, $\rho_2 c_2$, $\rho_3 c_3$: the characteristic impedances $\left(\text{in rayls} = \frac{Pa \cdot sec}{m}\right)$ of the three fluid media.

An omnidirectional, time-harmonic, point source is located in medium II at $r = 0$ and depth $z = z_0$ meters. The ocean depth is D meters. For both models, the boundary at $z = 0$ (i.e., the ocean surface) is treated as an ideal pressure-release boundary, which implies that no acoustic field will be present in medium I due to the source located in medium II. Both transmitter and receiver are stationary (not in motion). The analysis of the models is based on normal mode theory with the assumption of a constant speed of sound in the ocean.

3
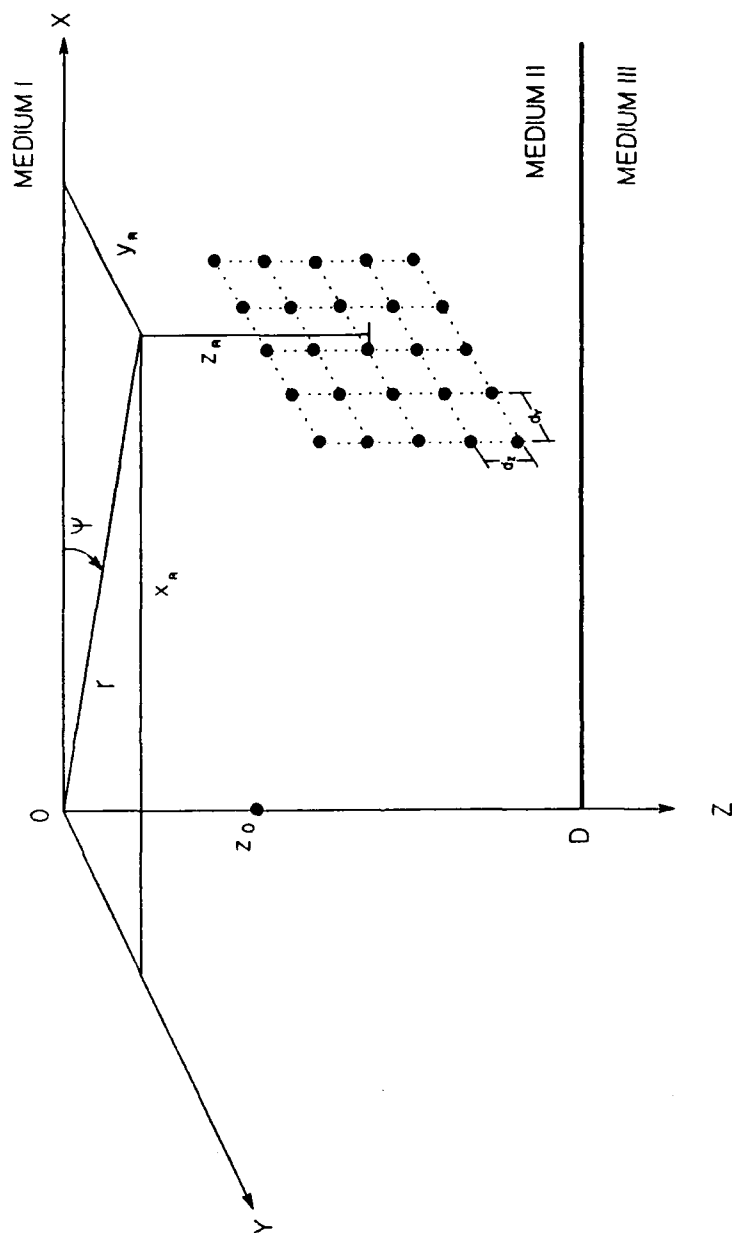
Figure 2.1 Ocean waveguide model.

A. PRESSURE-RELEASE SURFACE WITH A RIGID BOTTOM

This is the simplest of the two models, where the boundary at $z = D$ (i.e., the ocean bottom) is treated as an ideal rigid boundary, which implies that no acoustic field will be present in medium III due to the source located in medium II. For this model, the acoustic field due to the source located in medium II will be present only in medium II and no acoustic field will exist in media I and III.

The complete derivation of the expressions for the velocity potential and the acoustic pressure in medium II for this waveguide model is well known and can be found, for example, in Refs. 1, 2, or 3. In this thesis the equations and notation presented in Ref. 3 are used. A *summary* of the results of the analysis is presented and briefly discussed below:

The complete normal mode solution for the time-harmonic acoustic pressure in medium II at a point of cylindrical coordinates (r, ψ, z) is given by

$$p_2(t, r, \psi, z) = -j\frac{P_0}{2D} \sum_{n=0}^{N_p-1} \sin(k_{z_{2,n}} z_0) H_0^{(2)}(k_{r_{2,n}} r) \sin(k_{z_{2,n}} z) e^{+j2\pi ft} \qquad (2-1)$$

where the zeroth-order Hankel function of the second kind for the far-field case (i.e., $k_{r_{2,n}} r \gg 1$) is approximated by

$$H_0^{(2)}(k_{r_{2,n}} r) \approx \sqrt{\frac{2}{\pi k_{r_{2,n}} r}} e^{-j\left(k_{r_{2,n}} r - \frac{\pi}{4}\right)} , \qquad k_{r_{2,n}} r \gg 1 \qquad (2-2)$$

and P_0 is the peak acoustic pressure amplitude in pascals at the omnidirectional point source. The pulse propagation solution for this waveguide model shall be obtained by using Eq. (2–1) as the starting point and will be discussed in Section C.

The wave number k_2, in radians per meter, is given by

$$k_2 = \frac{2\pi f}{c_2} = \frac{2\pi}{\lambda_2} \qquad (2-3)$$

where f is the frequency of the source in hertz. The propagation vector component in the z-direction, which is only allowed certain discrete values, is given in radians

per meter by

$$k_{z_2} = k_{z_2,n} = \frac{(2n+1)\pi}{2D} \ , \quad n = 0, 1, 2, ... \qquad (2-4)$$

The set of functions $\sin\left(k_{z_2,n} z\right)$, $n = 0, 1, 2, ...$, are referred to as the eigenfunctions or normal modes and the set of values $k_{z_2,n}$, $n = 0, 1, 2, ...$, are referred to as the eigenvalues. The normal modes describe the natural modes of vibration within the waveguide.

The propagation vector component in the radial direction for the nth normal mode, in radians per meter, is given by

$$k_{r_2} = k_{r_2,n} = \begin{cases} k_2\sqrt{1 - \left(\frac{f_n}{f}\right)^2} & , f \geq f_n \\ -jk_2\sqrt{\left(\frac{f_n}{f}\right)^2 - 1} & , f < f_n \end{cases} \qquad (2-5)$$

where f_n is the *cutoff frequency* for the nth mode, in hertz and is given by

$$f_n = \frac{(2n+1)c_2}{4D} \ , \quad n = 0, 1, 2, ... \qquad (2-6)$$

For a given value of source frequency f, the nth mode will be a propagating mode only if $f > f_n$. If $f < f_n$, then the nth mode is an evanescent mode (i.e., a decaying exponential). The total number of propagating modes N_p excited by a source frequency of f hertz, is given by

$$N_p = \text{INT}\left[\frac{1}{2}\left(\frac{4Df}{c_2} - 1\right)\right] + 1 \qquad (2-7)$$

where INT[•] means form an integer by simply truncating the decimal portion of the real number inside the square brackets. One is added to the result since the first or lowest mode is mode $n = 0$. Additional information concerning this model is given next.

The angle of propagation for the nth normal mode is given by

$$\theta_{2,n} = \sin^{-1}\left[\sqrt{1 - \left(\frac{f_n}{f}\right)^2}\right] \ , \qquad f \geq f_n \ , \quad n = 0, 1, 2, ... \qquad (2-8)$$

6
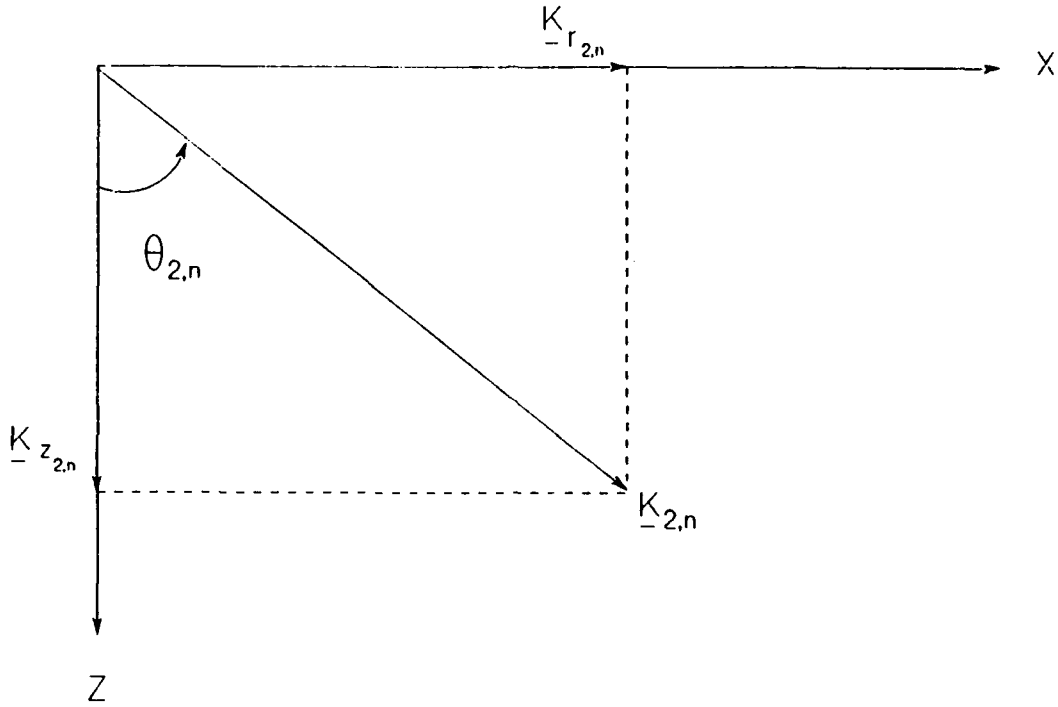
Figure 2.2 Propagation vector components of the nth normal mode.

where f_n is given by Eq. (2-6). The relationship between the propagation vector components $k_{z2,n}$ and $k_{r2,n}$, the wave number k_2, and the angle of propagation $\theta_{2,n}$ for the nth mode is shown in Fig. 2.2.

The group speed in the radial direction of the nth propagating mode, in meters per second, is given by

$$c_{g_{r2,n}} = c_2\sqrt{1 - \left(\frac{f_n}{f}\right)^2} , \qquad f \geq f_n , \quad n = 0, 1, 2, ... \qquad (2-9)$$

The radial group speed is the speed at which energy propagates in the radial direction and is a function of frequency f. Therefore, the energy associated with different frequency components will propagate at different speeds. As a result, for a particular mode n with cutoff frequency f_n, the high frequency components from a transmitted pulse will arrive at a receiver ahead of the low frequency components. Therefore, due to this dispersion of energy, the shape of the transmitted pulse will be distorted at

7

the receiver.

Finally, the energy E_n contained in the nth eigenfunction is given by

$$E_n = \frac{D}{2} \,, \quad n = 0, 1, 2, ... \qquad (2-10)$$

and the time of arrival, in seconds, at the receiver of the nth propagating normal mode is given by

$$t_{r_{2,n}} = \frac{r}{c_{g_{r_{2,n}}}} \qquad (2-11)$$

where r is the horizontal (polar) range between source and field points.

B. PRESSURE-RELEASE SURFACE WITH A FLUID BOTTOM

In this model the boundary at $z = D$ is treated as a boundary between two different fluid media—which is more realistic—instead of as an ideal rigid surface. For the fluid bottom model an acoustic field will, in general, be present in medium III due to the sound source located in medium II.

Once again, the complete derivation of the expressions for the velocity potential and the acoustic pressure in medium II for this waveguide model is well known and can be found, for example, in Refs. 1, 2, or 3. In this thesis, we shall use the equations and notation developed in Ref. 3. The analysis is based on the assumption that $c_3 > c_2$ and some of the results, which are used by the computer simulation program, are briefly *summarized* below:

The complete normal mode solution for the time-harmonic acoustic pressure in medium II at a point of cylindrical coordinates (r, ψ, z) is given by

$$p_2(t, r, \psi, z) = -j\frac{P_0}{4} \sum_{n=0}^{N_t-1} E_n^{-1} \sin(k_{z_{2,n}} z_0) H_0^{(2)}(k_{r_{2,n}} r) \sin(k_{z_{2,n}} z) e^{+j2\pi ft} \qquad (2-12)$$

8

where E_n is the energy contained in the nth eigenfunction and is given by

$$
E_n = \begin{cases} \dfrac{D}{2}, & \theta_{2,n} = \theta_c, \quad n = 0, 1, 2, \ldots \\[2ex] \dfrac{2Dk_{z_{2,n}} - \sin\left(2k_{z_{2,n}}D\right) - 2\left(\dfrac{\rho_2}{\rho_3}\right)\tan\left(k_{z_{2,n}}D\right)\sin^2\left(k_{z_{2,n}}D\right)}{4k_{z_{2,n}}}, & \theta_c \leq \theta_{2,n} < \dfrac{\pi}{2} \end{cases}
$$

$$(2-13)$$

and $H_0^{(2)}(k_{r_{2,n}})$ is approximated by Eq. (2-2).

For a given value of source frequency f, the allowed directions of propagation in medium II correspond to the roots $\theta_2 = \theta_{2,n}$, $n = 0, 1, 2, \ldots$, of the following transcendental equation:

$$
\tan\left(\frac{2\pi f}{c_2}D\cos\theta_2\right) + \frac{\rho_3 c_3 \cos\theta_2}{\rho_2 c_2 \sqrt{\left(\frac{\sin\theta_2}{\sin\theta_c}\right)^2 - 1}} = 0, \qquad c_3 > c_2, \qquad \theta_c \leq \theta_2 < \frac{\pi}{2}
$$

$$(2-14)$$

where θ_c is the critical angle of incidence at the ocean bottom and is given by

$$
\theta_c = \sin^{-1}\left(\frac{c_2}{c_3}\right), \qquad c_3 > c_2. \tag{2-15}
$$

Once the angles (roots) $\theta_{2,n}$ are calculated, then the propagating normal modes are known since the propagation vector for the nth propagating mode in medium II can be expressed as a function of the components $k_{r_{2,n}}$ and $k_{z_{2,n}}$ in the r and z directions given by

$$
k_{r_{2,n}} = k_2 \sin\theta_{2,n}, \tag{2-16}
$$

and

$$
k_{z_{2,n}} = k_2 \cos\theta_{2,n}. \tag{2-17}
$$

Note that for $\theta_2 = 90^0$, the plane-wave mode is defined. In reality, there is no plane-wave mode propagating, since for $\theta_2 = 90^0$ in Eq. (2-17), we obtain $k_{z_{2,n}} = 0$ and, therefore, $\sin(k_{z_{2,n}}) = 0$ in Eq. (2-12). As a result, the contribution of this mode to the acoustic pressure in medium II is zero. The pulse propagation solution for this

waveguide model shall be obtained by using Eq. (2-12) as the starting point and will be discussed in Section C.

The normal modes corresponding to the roots $\theta_{2,n}$, $n = 0, 1, 2, ...$ of Eq. (2-14) are known as trapped modes. These modes are "trapped" in medium II since (i) the complex reflection coefficient at the ideal pressure-release ocean surface has a magnitude of unity, for every value of the angle of incidence, and (ii) the complex reflection coefficient at the fluid ocean bottom also has a magnitude of unity, for the angles of incidence in the range $\theta_c \leq \theta_i = \theta_{2,n} \leq 90^\circ$, where θ_i refers to the angle of incidence. The cutoff frequency f_n, in hertz, for the nth trapped normal mode is given by

$$f_n = \frac{(2n+1)c_2}{4D\cos\theta_c} \ , \quad n = 0, 1, 2, ... \qquad (2-18)$$

The total number of trapped normal modes N_t excited by a source frequency f hertz is given by

$$N_t = \text{INT}\left[\frac{1}{2}\left(\frac{4Df\cos\theta_c}{c_2} - 1\right)\right] + 1. \qquad (2-19)$$

Finally, the group speed in the radial direction, in meters per second, of the nth trapped mode is given by

$$c_{g_{r2,n}} = \frac{c_2{}^2 k_{r2,n}}{2\pi f} \ , \qquad f \geq f_n \ , \quad n = 0, 1, 2, ... \qquad (2-20)$$

and the time of arrival at the receiver of the nth trapped mode in seconds is given by Eq. (2-11).

C. COMPUTER IMPLEMENTATION OF THE MODELS

In order to examine and compare the two ocean waveguide models by using a computer simulation approach, the models are implemented by a computer program written in the Fortran 77 programming language. The basic techniques used by the program are (i) discrete time representation (sampling) of continuous time signals and

10

(ii) using complex envelope representations for the transmitted and received signals. The computer program is constructed using the block structure approach and it is composed of subprograms which are used to perform the computations involved in the various steps of the problem. Among these subprograms, the most important are (i) the signal generator for the transmitted electrical signal, (ii) the resulting time-domain output electrical pulse from the center element in the receive array, and (iii) the calculation of the roots of the transcedental equation for the fluid bottom model.

The signal generator subroutine was developed and tested during a previous related thesis work [Ref. 6]. It is used as a tool in this thesis and it has been included in the computer program structure with no changes. However, care has been taken in order to create a more accurate representation of rectangular-envelope pulses by increasing the number of the harmonics involved in the computations in the signal generator.

The pulse propagation solution for the complex acoustic pressure field and the resulting output time-domain pulse at the center element of the receive array due to all transmitted frequency components is discussed next.

The expression for the time-harmonic acoustic pressure at time t and spatial location $\underline{r}$ can be written as

$$p(t,\underline{r}) = P(f,\underline{r})e^{+j2\pi ft} \ . \tag{2-21}$$

If we compare Eq. (2-21) with Eqs. (2-1) and (2-12), then

$$P(f,\underline{r}) = -j\frac{P_0}{2D} \sum_{n=0}^{N_p-1} \sin(k_{z_{2,n}} z_0) H_0^{(2)}(k_{r_{2,n}} r) \sin(k_{z_{2,n}} z) \tag{2-22}$$

for the pressure-release surface with a rigid bottom model and

$$P(f,\underline{r}) = -j\frac{P_0}{4} \sum_{n=0}^{N_t-1} E_n^{-1} \sin(k_{z_{2,n}} z_0) H_0^{(2)}(k_{r_{2,n}} r) \sin(k_{z_{2,n}} z) \tag{2-23}$$

11

for the pressure-release surface with a fluid bottom model. Therefore, the complex acoustic pressure field at time t and position $\underline{r}$ due to a transmitted pulse is given by

$$p(t,\underline{r}) = \int_{-\infty}^{+\infty} X(f)P(f,\underline{r})e^{+j2\pi ft}df \qquad (2-24)$$

where the term $P(f,\underline{r})e^{+j2\pi ft}$ is the time-harmonic solution and $X(f)$ is the complex frequency spectrum of the real transmitted bandpass signal $x(t)$. The frequency spectrum $X(f)$ is related to the complex frequency spectrum $\tilde{X}(f)$ of the complex envelope $\tilde{x}(t)$ as follows :

$$X(f) = \frac{1}{2}\{\tilde{X}(f - f_c) + \tilde{X}^*[-(f + f_c)]\} \qquad (2-25)$$

where f_c is the carrier frequency of the transmitted signal [Ref. 7:pp. 187-188].

The signal generator represents the complex envelope $\tilde{x}(t)$ by a finite Fourier series

$$\tilde{x}(t) = \sum_{q=-K}^{K} c_q e^{+j2\pi q f_0 t} , \qquad |t| \leq \frac{T_0}{2} \qquad (2-26)$$

where c_q is the complex Fourier coefficient at harmonic q, f_0 is the fundamental frequency in hertz of the transmitted pulse, and $T_0 = 1/f_0$ is the fundamental period in seconds [Ref. 6]. The integer K defines the highest harmonic number required to represent the baseband complex envelope of the transmitted signal.

With the use of Eq. (2-26), the complex frequency spectrum $\tilde{X}(f)$ of the complex envelope is given by

$$\tilde{X}(f) = \sum_{q=-K}^{K} c_q \delta(f - qf_0) \qquad (2-27)$$

and, as a result,

$$\tilde{X}(f - f_c) = \sum_{q=-K}^{K} c_q \delta[f - (f_c + qf_0)] . \qquad (2-28)$$

The complex conjugate frequency spectrum $\tilde{X}^*(f)$ of the complex envelope is given by

$$\tilde{X}^*(f) = \sum_{q=-K}^{K} c_q^* \delta(f - qf_0) \qquad (2-29)$$

12

and, as a result,

$$\tilde{X}^*[-(f + f_c)] = \sum_{q=-K}^{K} c_q^* \delta[f + (f_c + qf_0)] \qquad (2-30)$$

since

$$\delta[-(f + f_c + qf_0)] = \delta[f + (f_c + qf_0)] . \qquad (2-31)$$

Next, by using Eqs. (2-25), (2-27) and (2-30) in Eq. (2-24), it can be written as

$$
\begin{aligned}
p(t,\underline{r}) &= \frac{1}{2}\int_{-\infty}^{+\infty} \sum_q c_q \delta[f - (f_c + qf_0)]P(f,\underline{r})e^{+j2\pi ft}df \\
&\quad + \frac{1}{2}\int_{-\infty}^{+\infty} \sum_q c_q^* \delta[f + (f_c + qf_0)]P(f,\underline{r})e^{+j2\pi ft}df
\end{aligned} \qquad (2-32)
$$

or

$$
\begin{aligned}
p(t,\underline{r}) &= \frac{1}{2}\sum_q c_q P(f_c + qf_0,\underline{r})e^{+j2\pi qf_0 t}e^{+j2\pi f_c t} \\
&\quad + \frac{1}{2}\sum_q c_q^* P[-(f_c + qf_0),\underline{r}]e^{-j2\pi qf_0 t}e^{-j2\pi f_c t} .
\end{aligned} \qquad (2-33)
$$

Since it can be shown that

$$P[-(f_c + qf_0),\underline{r}] = P^*(f_c + qf_0,\underline{r}) , \qquad (2-34)$$

by using Eq. (2-34) in Eq. (2-33), it can be written as

$$p(t,\underline{r}) = \frac{1}{2}\sum_q \left\{ c_q P(f_c + qf_0,\underline{r})e^{+j2\pi qf_0 t}e^{+j2\pi f_c t} + \left[c_q P(f_c + qf_0,\underline{r})e^{+j2\pi qf_0 t}e^{+j2\pi f_c t} \right]^* \right\}$$

$$(2-35)$$

or

$$p(t,\underline{r}) = Re\left\{ \sum_q c_q P(f_c + qf_0,\underline{r})e^{+j2\pi qf_0 t}e^{j2\pi f_c t} \right\} \qquad (2-36)$$

since for any arbitrary complex quantity Z, it is known that

$$Re\{Z\} = \frac{1}{2}(Z + Z^*) . \qquad (2-37)$$

Finally, the pulse propagation solution for the complex acoustic pressure field due to all transmitted frequency components is given by

$$p(t,\underline{r}) = Re\left\{ \tilde{p}(t,\underline{r})e^{+j2\pi f_c t} \right\} \qquad (2-38)$$

13

where

$$\tilde{p}(t,\underline{r}) = \sum_{q=-K}^{K} c_q P(f_c + qf_0, \underline{r})e^{+j2\pi qf_0 t} . \qquad (2-39)$$

The function of an individual point-element (hydrophone) in a receive array is to convert an acoustic pressure signal into an electrical output signal. For the purposes of this thesis, the resulting output electrical signal is assumed to be

$$y(t,\underline{r}) = p(t,\underline{r}) \qquad (2-40)$$

which implies that there are no losses in the conversion from acoustic to electric power at the receiving element (hydrophone).

The peak acoustic pressure amplitude P_0 at the omnidirectional point source, which is involved in Eqs. (2-1) and (2-12) for the calculation of the time-harmonic complex acoustic pressure field for both models, is set equal to one pascal, that is, $P_0 = 1$ Pa. This implies that a single frequency component of f hertz with amplitude of 1 volt produces a peak acoustic pressure of 1 pascal at the source. The information concerning the amplitudes of the various frequency components contained in the transmitted electrical signal $x(t)$ is accounted for in the Fourier coefficients of the complex envelope $\tilde{x}(t)$.

In order to implement the pressure-release surface with a fluid bottom model, the roots of the transcendental equation given by Eq. (2-14) must be calculated numerically. For that purpose, the IMSL (MATH/LIBRARY) routine ZBREN/DZBREN was used. The transcendental equation given by Eq. (2-14) is defined as a function of θ_2 where $\theta_c \leq \theta_2 < \frac{\pi}{2}$. A graphical representation of the transcendental equation and the location of the zero crossings, which are the roots, are shown in Fig. 2.3 for two typical cases. The use of the IMSL routine ZBREN/DZBREN will be discussed next.
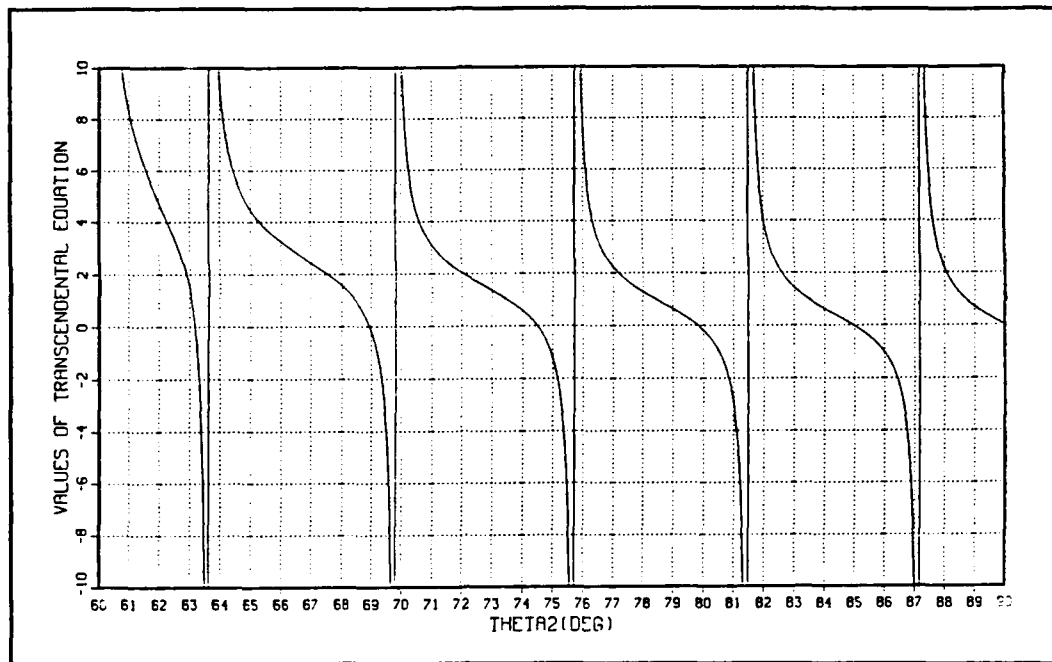
(a) $f = 76\ Hz$, $D = 100\ m$, $\theta_c = 60.1^0$, $N_t = 5$ Trapped Modes
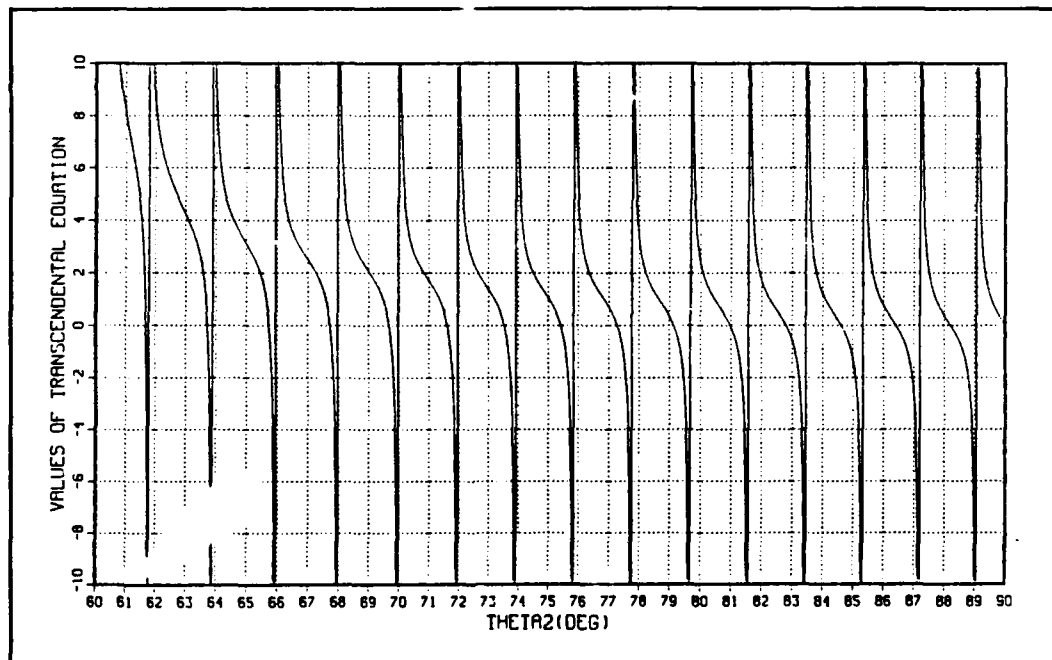
(b)$f = 230\ Hz$, $D = 100\ m$, $\theta_c = 60.1^0$, $N_t = 15$ Trapped Modes

Figure 2.3 Representation of the transcendental equation.

15

First, the left-hand side of the transcendental equation

$$T(\theta_2) = \tan\left(\frac{2\pi f}{c_2} D \cos\theta_2\right) + \frac{\rho_3 c_3 \cos\theta_2}{\rho_2 c_2 \sqrt{\left(\frac{\sin\theta_2}{\sin\theta_c}\right)^2 - 1}} \ , \qquad c_3 > c_2 \ , \qquad \theta_c \leq \theta_2 < \frac{\pi}{2}$$

$$(2-41)$$

is sampled with the first sample taken very close to θ_c. The reason for this is to eliminate the possibility of missing a root very close to θ_c. The sampling is terminated with the last one taken at 90^0. The sampled values of the function $T(\theta_2)$ are stored in an array. Next, the program checks the sign of each sample in the array in order to find two consecutive samples with opposite signs. These two values are then passed to the DZBREN routine. The DZBREN routine is a double precision routine and it is able to find a zero of a real function which changes sign in a given interval. The routine calculates the root which is included in the given interval to the accuracy specified by the user. After the first root of the function $T(\theta_2)$ is calculated, the next array element to be put through the checking procedure is increased by a step size whose value corresponds to the distance $\Delta\theta_2 = (90^0 - \theta_c)/N_t$. This distance gives an estimation, in degrees, of how much apart the roots are located. The above mentioned step is calculated as $\text{INT}[\Delta\theta_2/2d]$, where d is the interval between the samples of the $T(\theta_2)$ function. This is done to avoid wasting the computer's time in performing unnecessary sign checking. After a new root has been calculated, the algorithm checks if the total number of the expected roots N_t has been reached. The procedure is followed until all the roots are calculated. The total number of roots should be equal to the value of N_t , where the root $\theta_2 = 90^0$ is not included, since this normal mode does not contribute to the total acoustic field. The first root, which corresponds to the normal mode $n = 0$, is the one closest to 90^0.

16

The computer simulation program for both models has been developed by incorporating the mathematical equations discussed in Sections A and B, and the supplementary information of the present section.

III. COMPUTER SIMULATION RESULTS

In this chapter, the computer simulation results for each model are presented and discussed. The models were examined under a relatively wide range of different cases. Both of the models were tested for various transmitted signals, that is, Hamming-envelope and rectangular-envelope continuous wave (CW) and linear-frequency-modulated (LFM) pulses. The models were also tested for various locations of the receiver, that is, the receiver was located at different ranges (short-range and long-range) and also at different depths (above and below the source). For all the test cases, that are presented in this thesis, the source is an omnidirectional point source located at the rectangular coordinates $(0,0,z_0)$, where the depth z_0 is set to $z_0 = 30$ m. The receiver is a 9x9 planar array of point elements (hydrophones) and it is shown in Fig. 3.1. The receive array is was placed at two different ranges (i.e., short-range: $X_R = 1000$ m, and long-range: $X_R = 10000$ m) and also at two different depths (i.e., above the source: $Z_R = 20$ m, and below the source: $Z_R = 80$ m). The depth of the ocean was set to $D = 100$ m.

The transmitted signals for the test cases are well known and they are briefly summarized as follows:

A continuous-wave (CW) pulse is described by [Ref. 7:pp. 193-195]

$$x(t) = a(t)\cos(2\pi f_c t) , \qquad |t| \leq \frac{T_P}{2} \qquad (3-1)$$

where T_P is the pulse length in seconds, f_c is the carrier frequency in hertz, and $a(t)$ is the amplitude modulating signal.

A linear-frequency-modulated (LFM) pulse is described by [Ref. 7:pp. 195-197]

$$x(t) = a(t)\cos[2\pi f_c t + \theta(t)] , \qquad |t| \leq \frac{T_P}{2} \qquad (3-2)$$
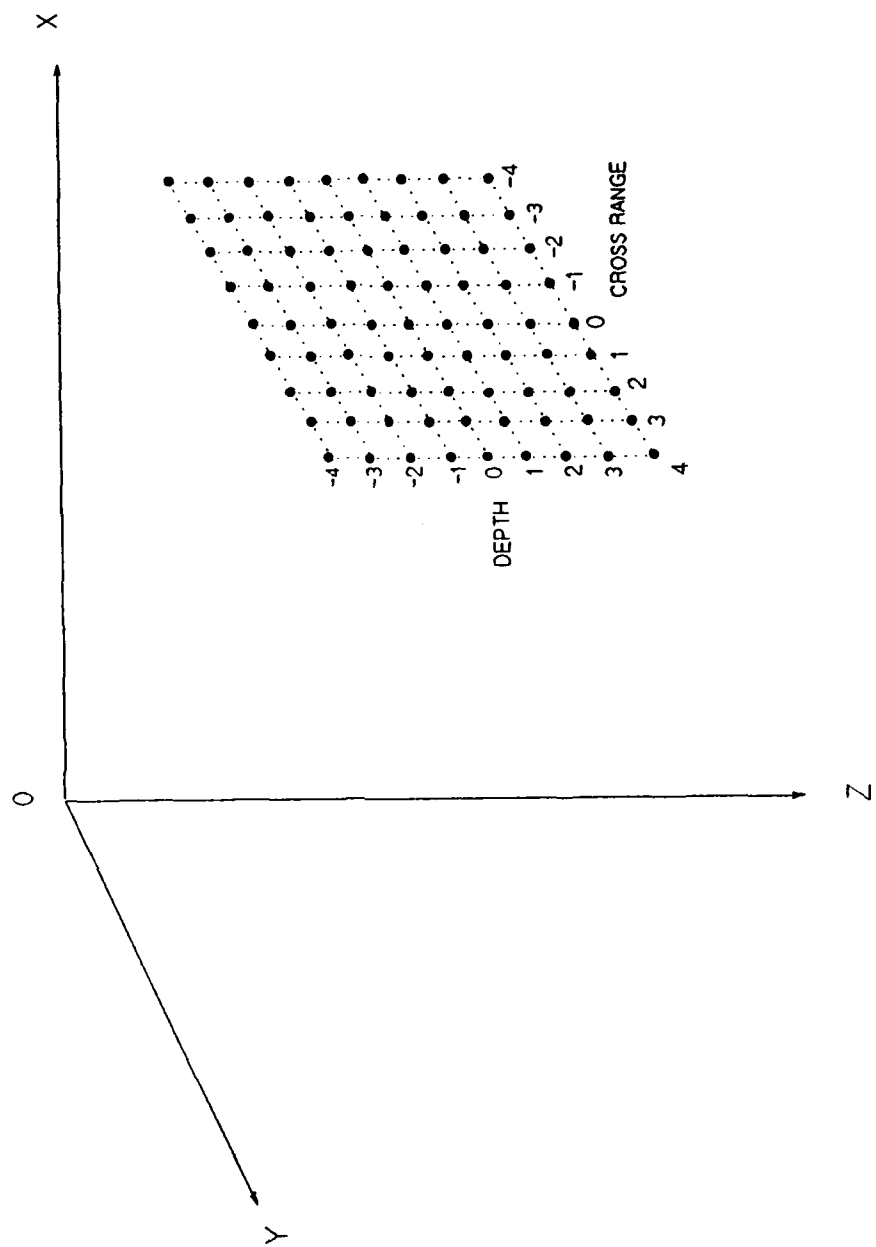
Figure 3.1 Receive array.

where the angle-modulating signal or phase deviation $\theta(t)$ is given by

$$\theta(t) = bt^2 \qquad\qquad (3-3)$$

where b is the phase-deviation constant, in radians per square second. When $b > 0$, the LFM pulse is called an "up chirp" and when $b < 0$ it is called a "down chirp". The quantity bT_P/π is referred to as the *swept bandwidth* in hertz.

The Hamming-envelope is a commonly used envelope and the corresponding amplitude modulating signal $a(t)$ is given by

$$a(t) = A\left(0.54 + 0.46\cos\frac{2\pi t}{T_P}\right) , \qquad |t| \le \tfrac{T_P}{2} \qquad\qquad (3-4)$$

where A (a constant) is the amplitude of the transmitted electrical pulse. For the rectangular-envelope case, the amplitude modulating signal is given by

$$a(t) = A , \qquad |t| \le \tfrac{T_P}{2} . \qquad\qquad (3-5)$$

The computer simulation results that are used in order to compare the two models for all the test cases are (i) the output time-domain electrical pulse from the center element in the receive array and (ii) the characteristics of the complex acoustic pressure field (magnitude and phase as a function of frequency at each point of the field) when the previously mentioned input electrical signals at the source are transmitted through each model. There are also some other simulation results, which give additional information about the propagation of the transmitted pulses through the two models. These additional simulation results for both models include (i) the group speed, time of arrival, etc., of the propagating modes for three characteristic frequencies (i.e., lowest, carrier, and highest) of the frequency spectrum of the transmitted pulse, and for the fluid bottom model, (ii) a graphical representation of the transcendental equation for these three frequencies. The results of the various test cases will be presented and discussed in the following order:

20

- Hamming-envelope CW pulse propagation using the rigid and the fluid bottom models in the short range (receiver located above and below the source).

- Hamming-envelope CW pulse propagation using the fluid bottom model in the long range (receiver located above and below the source).

- Hamming-envelope LFM pulse propagation using the rigid and the fluid bottom models in the short range (receiver located above and below the source).

- Hamming-envelope LFM pulse propagation using the fluid bottom model in the long range (receiver located above and below the source).

- Rectangular-envelope CW pulse propagation using the fluid bottom model in the long range (receiver located above and below the source).

- Rectangular-envelope LFM pulse propagation using the fluid bottom model in the long range (receiver located above and below the source).

A. HAMMING-ENVELOPE PULSES

1. Continuous-wave (CW) pulse

The transmitted electrical signal is a Hamming-envelope CW pulse and it is shown in Fig. 3.2. The transmitted pulse was generated by the signal generator subprogram [Ref. 6]. The characteristics of the pulse shown in Fig. 3.2 and the notation are as follows:

Amplitude $A = 10.0$

Pulse Length $T_P = 100.0$ msec

Carrier frequency $f_c = 250$ Hz

Pulse repetition frequency (PRF) or fundamental frequency $f_0 = $ PRF $=$
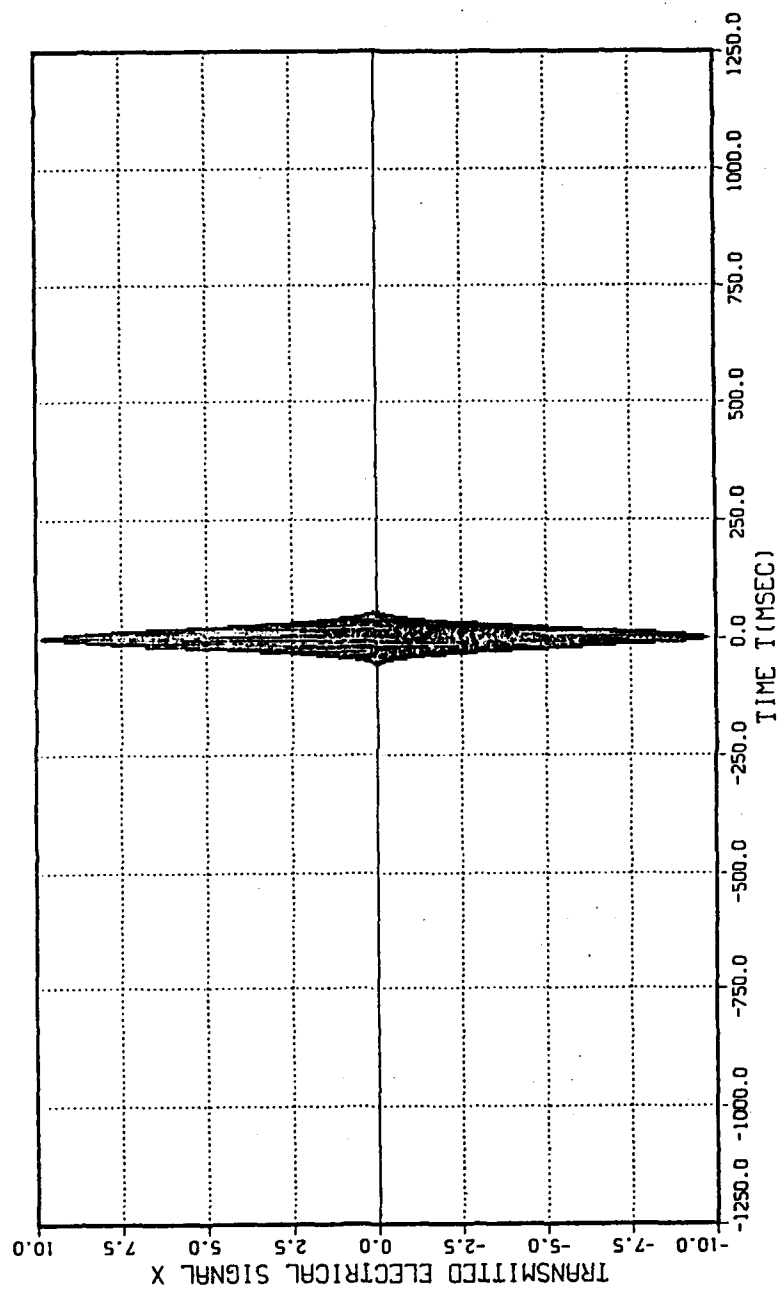
  0.4 Hz

Figure 3.2 Hamming-envelope CW pulse ($f_0 = 0.4$ Hz).

22

Number of harmonics NFREQ = 101

The parameter NFREQ defines the total number of harmonics required to represent the baseband complex envelope of the transmitted electrical signal in order to synthesize the pulse. The value of this parameter gives an indication about the expected complexity of the involved computations performed by the computer program, and about the size of the required computer memory. In other words, when the value of the parameter NFREQ is increased, then the computation time is longer and larger memory is required for the execution of the program. For the case shown in Fig. 3.2, the lowest frequency component of the set of harmonics required to represent the transmitted signal is $f = 230$ Hz, and the highest is $f = 270$ Hz.

The short range (i.e., $X_R = 1000$ m) results of the rigid bottom model are presented first. The numerical results computed by the program concerning the propagating modes of the lowest ($f = 230$ Hz), the carrier ($f = 250$ Hz), and the highest ($f = 270$ Hz) frequency components are shown in Tables 3.1, 3.2 and 3.3. These results are presented only once, that is, for this case only. The involved parameters and the notation used in these tables are as follows:

MODES: Total number of propagating modes N_p [see Eq. (2–7)]

K2: Wave number k_2 [see Eq. (2–3)]

N: Individual mode number

FN: Cutoff frequency f_n for the nth mode [see Eq. (2–6)]

THETA2N: Angle of propagation $\theta_{2,n}$ for the nth mode [see Eq. (2–8)]

KR2N: Propagation vector component $k_{r_{2,n}}$ in the radial direction for the nth mode [see Eq. (2–5)]

KZ2N: Propagation vector component $k_{z_{2,n}}$ in the z-direction for the nth mode [see Eq. (2–4)]

CGR2N: Group speed $c_{g_{r_{2,n}}}$ in the radial direction for the nth mode [see

DEPTH = 100.0 M   F = 230.0 HZ   MODES = 31   K2 = 0.96342 RAD/M

N	FN (HZ)	THETA2N (DEG)	KR2N (RAD/M)	KZ2N (RAD/M)	CGR2N (M/SEC)	EN	TR2N (SEC)
0	3.750	89.066	0.96329	0.01571	1499.801	50.000	0.666755
1	11.250	87.196	0.96227	0.04712	1498.205	50.000	0.667466
2	18.750	85.324	0.96022	0.07854	1495.007	50.000	0.668893
3	26.250	83.447	0.95713	0.10996	1490.199	50.000	0.671051
4	33.750	81.562	0.95299	0.14137	1483.763	50.000	0.673962
5	41.250	79.668	0.94780	0.17279	1475.679	50.000	0.677654
6	48.750	77.763	0.94153	0.20420	1465.919	50.000	0.682166
7	56.250	75.844	0.93417	0.23562	1454.449	50.000	0.687545
8	63.750	73.908	0.92567	0.26704	1441.230	50.000	0.693852
9	71.250	71.954	0.91603	0.29845	1426.211	50.000	0.701158
10	78.750	69.977	0.90519	0.32987	1409.336	50.000	0.709554
11	86.250	67.976	0.89312	0.36128	1390.537	50.000	0.719147
12	93.750	65.945	0.87976	0.39270	1369.735	50.000	0.730068
13	101.250	63.882	0.86505	0.42412	1346.837	50.000	0.742480
14	108.750	61.782	0.84892	0.45553	1321.734	50.000	0.756582
15	116.250	59.640	0.83130	0.48695	1294.297	50.000	0.772620
16	123.750	57.449	0.81208	0.51836	1264.376	50.000	0.790904
17	131.250	55.204	0.79115	0.54978	1231.788	50.000	0.811828
18	138.750	52.896	0.76837	0.58119	1196.316	50.000	0.835900
19	146.250	50.515	0.74357	0.61261	1157.695	50.000	0.863786
20	153.750	48.050	0.71653	0.64403	1115.598	50.000	0.896381
21	161.250	45.486	0.68699	0.67544	1069.614	50.000	0.934917
22	168.750	42.803	0.65462	0.70686	1019.217	50.000	0.981145
23	176.250	39.977	0.61898	0.73827	963.717	50.000	1.037649
24	183.750	36.974	0.57945	0.76969	902.170	50.000	1.108439
25	191.250	33.745	0.53517	0.80111	833.238	50.000	1.200137
26	198.750	30.216	0.48486	0.83252	754.902	50.000	1.324675
27	206.250	26.267	0.42637	0.86394	663.839	50.000	1.506389
28	213.750	21.667	0.35570	0.89535	553.808	50.000	1.805680
29	221.250	15.855	0.26321	0.92677	409.804	50.000	2.440192
30	228.750	5.976	0.10031	0.95819	156.173	50.000	6.403148

TABLE 3.1 Rigid bottom: Numerical results for the lowest frequency component.

DEPTH = 100.0 M   F = 250.0 HZ   MODES = 33   K2 = 1.04720 RAD/M

N	FN (HZ)	THETA2N (DEG)	KR2N (RAD/M)	KZ2N (RAD/M)	CGR2N (M/SEC)	EN	TR2N (SEC)
0	3.750	89.141	1.04708	0.01571	1499.831	50.000	0.666742
1	11.250	87.421	1.04614	0.04712	1498.480	50.000	0.667343
2	18.750	85.699	1.04425	0.07854	1495.775	50.000	0.668550
3	26.250	83.973	1.04141	0.10996	1491.708	50.000	0.670372
4	33.750	82.241	1.03761	0.14137	1486.268	50.000	0.672826
5	41.250	80.503	1.03284	0.17279	1479.440	50.000	0.675931
6	48.750	78.755	1.02709	0.20420	1471.205	50.000	0.679715
7	56.250	76.997	1.02035	0.23562	1461.538	50.000	0.684211
8	63.750	75.226	1.01258	0.26704	1450.412	50.000	0.689459
9	71.250	73.441	1.00377	0.29845	1437.791	50.000	0.695511
10	78.750	71.639	0.99389	0.32987	1423.638	50.000	0.702426
11	86.250	69.818	0.98290	0.36128	1407.904	50.000	0.710276
12	93.750	67.976	0.97078	0.39270	1390.537	50.000	0.719147
13	101.250	66.109	0.95747	0.42412	1371.475	50.000	0.729142
14	108.750	64.215	0.94293	0.45553	1350.646	50.000	0.740387
15	116.250	62.290	0.92710	0.48695	1327.966	50.000	0.753031
16	123.750	60.330	0.90990	0.51836	1303.339	50.000	0.767260
17	131.250	58.332	0.89127	0.54978	1276.653	50.000	0.783298
18	138.750	56.289	0.87111	0.58119	1247.776	50.000	0.801426
19	146.250	54.197	0.84931	0.61261	1216.550	50.000	0.821997
20	153.750	52.048	0.82574	0.64403	1182.791	50.000	0.845458
21	161.250	49.834	0.80025	0.67544	1146.274	50.000	0.872392
22	168.750	47.546	0.77264	0.70636	1106.727	50.000	0.905566
23	176.250	45.170	0.74268	0.73827	1063.811	50.000	0.940017
24	183.750	42.693	0.71007	0.76969	1017.101	50.000	0.983187
25	191.250	40.093	0.67443	0.80111	966.045	50.000	1.035148
26	198.750	37.345	0.63524	0.83252	909.914	50.000	1.099005
27	206.250	34.412	0.59181	0.86394	847.699	50.000	1.179664
28	213.750	31.240	0.54311	0.89535	777.942	50.000	1.285443
29	221.250	27.748	0.48757	0.92677	698.387	50.000	1.431872
30	228.750	23.794	0.42250	0.95819	605.181	50.000	1.652399
31	236.250	19.091	0.34251	0.98960	490.605	50.000	2.038298
32	243.750	12.839	0.23269	1.02102	333.307	50.000	3.000234

TABLE 3.2 Rigid bottom: Numerical results for the carrier frequency component.

25

DEPTH = 100.0 M   F = 270.0 HZ   MODES = 36   K2 = 1.13097 RAD/M

N	FN (HZ)	THETA2N (DEG)	KR2N (RAD/M)	KZ2N (RAD/M)	CGR2N (M/SEC)	EN	TR2N (SEC)
0	3.750	89.204	1.13086	0.01571	1499.855	50.000	0.666731
1	11.250	87.612	1.12999	0.04712	1498.697	50.000	0.667246
2	18.750	86.018	1.12824	0.07854	1496.379	50.000	0.668280
3	26.250	84.421	1.12562	0.10996	1492.894	50.000	0.669840
4	33.750	82.819	1.12210	0.14137	1488.235	50.000	0.671937
5	41.250	81.212	1.11770	0.17279	1482.391	50.000	0.674586
6	48.750	79.598	1.11239	0.20420	1475.347	50.000	0.677807
7	56.250	77.975	1.10616	0.23562	1467.087	50.000	0.681623
8	63.750	76.343	1.09900	0.26704	1457.589	50.000	0.686064
9	71.250	74.699	1.09088	0.29845	1446.830	50.000	0.691166
10	78.750	73.042	1.08180	0.32987	1434.780	50.000	0.696971
11	86.250	71.371	1.07172	0.36128	1421.408	50.000	0.703528
12	93.750	69.682	1.06061	0.39270	1406.674	50.000	0.710897
13	101.250	67.976	1.04844	0.42412	1390.537	50.000	0.719147
14	108.750	66.248	1.03518	0.45553	1372.947	50.000	0.728360
15	116.250	64.497	1.02078	0.48695	1353.846	50.000	0.738636
16	123.750	62.720	1.00519	0.51836	1333.171	50.000	0.750092
17	131.250	60.915	0.98835	0.54978	1310.846	50.000	0.762866
18	138.750	59.077	0.97021	0.58119	1286.785	50.000	0.777131
19	146.250	57.203	0.95069	0.61261	1260.890	50.000	0.793091
20	153.750	55.289	0.92969	0.64403	1233.045	50.000	0.811001
21	161.250	53.329	0.90713	0.67544	1203.114	50.000	0.831177
22	168.750	51.318	0.88287	0.70686	1170.937	50.000	0.854017
23	176.250	49.249	0.85677	0.73827	1136.324	50.000	0.880031
24	183.750	47.113	0.82866	0.76969	1099.045	50.000	0.909881
25	191.250	44.901	0.79833	0.80111	1058.817	50.000	0.944450
26	198.750	42.599	0.76551	0.83252	1015.291	50.000	0.984939
27	206.250	40.192	0.72987	0.86394	968.022	50.000	1.030035
28	213.750	37.658	0.69097	0.89535	916.430	50.000	1.091191
29	221.250	34.971	0.64823	0.92677	859.738	50.000	1.163145
30	228.750	32.089	0.60082	0.95819	796.858	50.000	1.254929
31	236.250	28.955	0.54753	0.98960	726.184	50.000	1.377061
32	243.750	25.474	0.48644	1.02102	645.161	50.000	1.550001
33	251.250	21.478	0.41411	1.05243	549.226	50.000	1.820744
34	258.750	16.598	0.32307	1.08385	428.478	50.000	2.333840
35	266.250	9.560	0.18784	1.11527	249.130	50.000	4.013962

TABLE 3.3 Rigid bottom: Numerical results for the highest frequency component.

26

Eq. (2-9)]

EN: Energy E_n of the nth mode [see Eq. (2-10)]

TR2N: Time of arrival $t_{r_2,n}$ of the nth mode [see Eq. (2-11)].

The numerical results shown in Tables 3.1, 3.2 and 3.3 characterize the way the allowed modes for the frequencies $f = 230$ Hz, $f = 250$ Hz and $f = 270$ Hz propagate through the model.

The complex acoustic pressure (magnitude and phase) across the elements of the receive array for the carrier frequency ($f = 250$ Hz) at the two locations of the receiver are presented by the 3-D plots in Fig. 3.3 and 3.4. Figures 3.3 and 3.4 show how different the magnitude of the resulting acoustic pressure field is, depending on the depth of the receiver for the same horizontal range.

In the rigid bottom model the allowed angle of propagation for the nth normal mode can be in the range $0^0 < \theta_{2,n} < 90^0$ and it is restricted only by the cutoff frequency f_n for that mode. Some frequency components which are very close to the cutoff frequency f_n of the nth mode will propagate at very small propagation angles (i.e., in the range $0^0 - 10^0$). Therefore, the effects of these frequency components are expected to take more time to appear in the received pulse. As a result, the fundamental frequency f_0 of the transmitted pulse must be chosen small enough in order that all frequency components, propagating at various modes and angles, arrive at the receiver within the fundamental period $T_0 = 1/f_0$ seconds.

The resulting output time-domain pulses from the center element of the receive array for $f_0 = 0.4$ Hz and for the two receiver locations are shown in Fig. 3.5.

In order to increase the fundamental period T_0, an attempt was made of using $f_0 = 0.2$ Hz. The transmitted electrical signal for $f_0 = 0.2$ Hz is shown in Fig. 3.6. The number of harmonics required to represent this signal is NFREQ = 201. The resulting output time-domain pulses from the center element of the receive array for
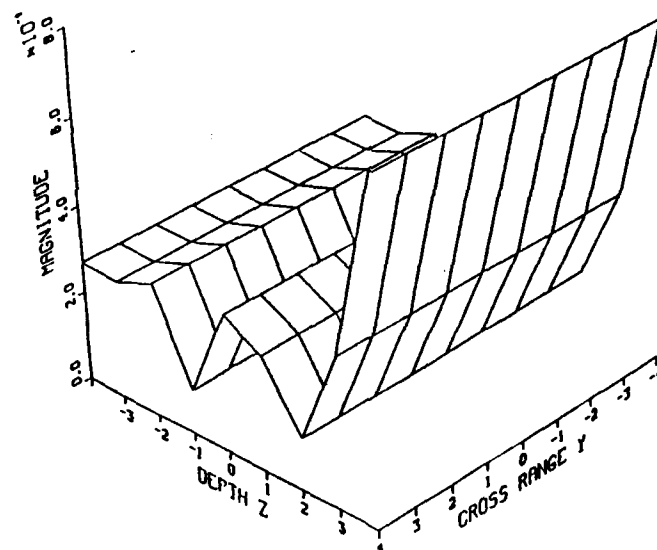
27

CASE: RIGID   FREQUENCY: 250.0 HZ

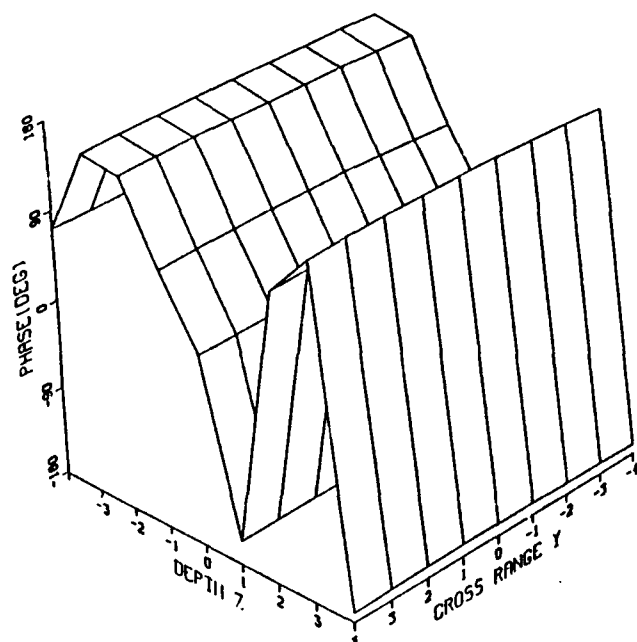ZT: 30.0 M   XR: 1000.0 M   YR: 0.0 M   ZR: 20.0 M

(a)
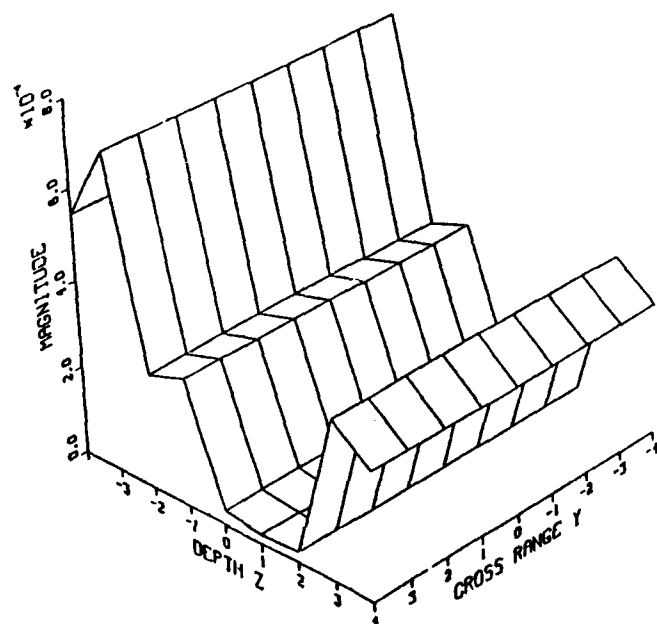
CASE: RIGID   FREQUENCY: 250.0 HZ

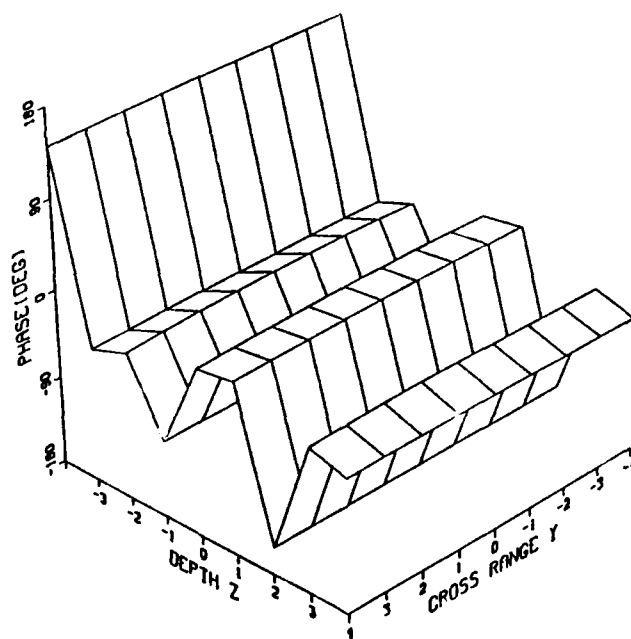ZT: 30.0 M   XR: 1000.0 M   YR: 0.0 M   ZR: 80.0 M

(b)

Figure 3.3 Rigid bottom: Magnitude of the complex acoustic pressure field for Hamming-envelope CW pulse for (a) receiver above the source and (b) receiver below the source.

28

CASE: RIGID   FREQUENCY: 250.0 HZ
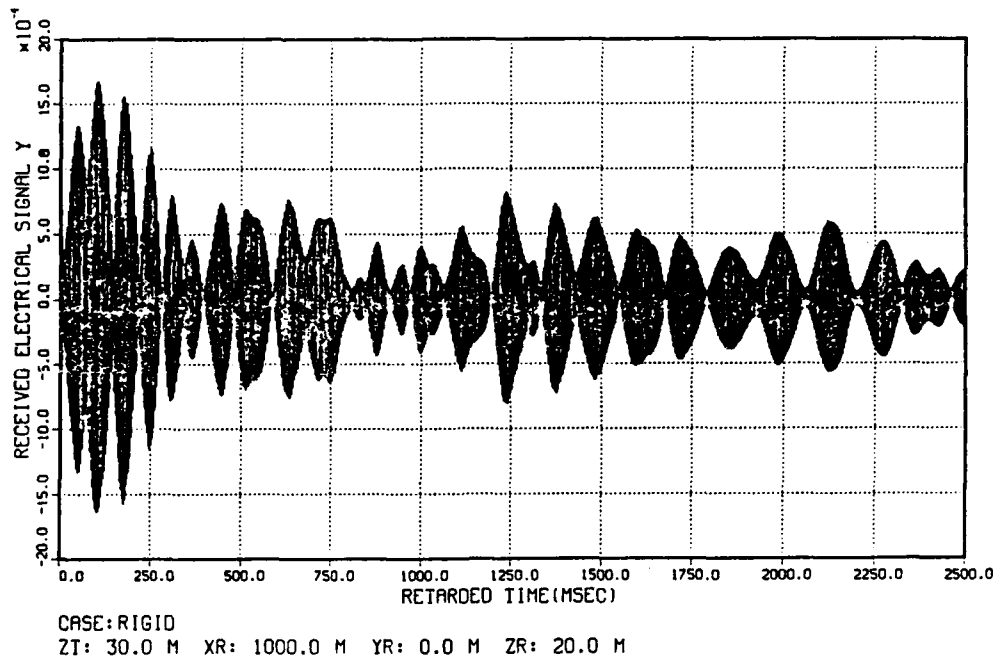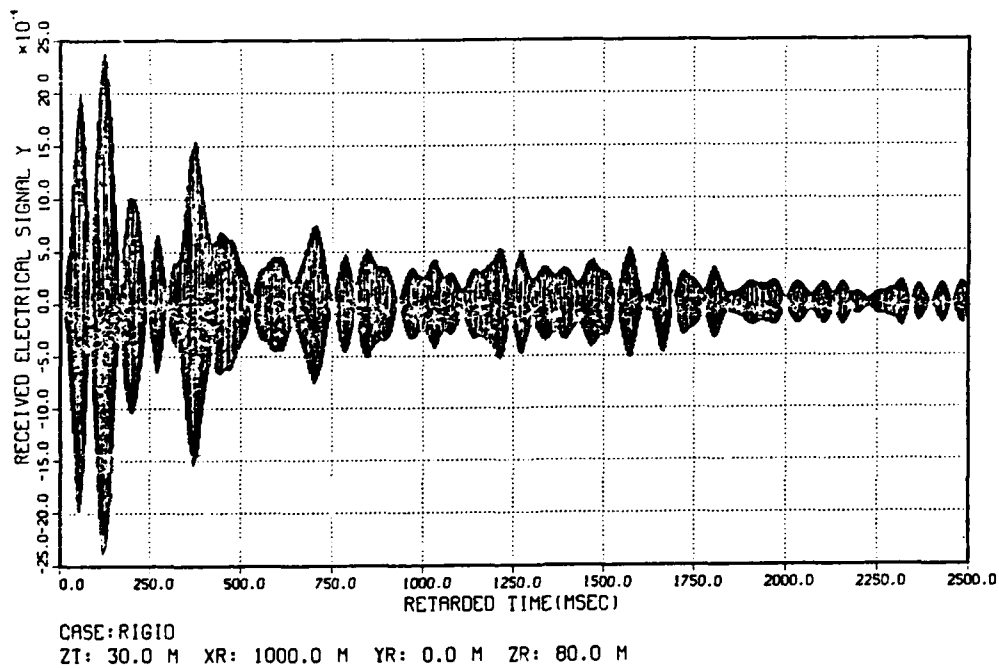
ZT: 30.0 M   XR: 1000.0 M   YR: 0.0 M   ZR: 20.0 M

(a)

CASE: RIGID   FREQUENCY: 250.0 HZ

ZT: 30.0 M   XR: 1000.0 M   YR: 0.0 M   ZR: 80.0 M

(b)

Figure 3.4 Rigid bottom: Phase of the complex acoustic pressure field for Hamming-envelope CW pulse for (a) receiver above the source and (b) receiver below the source.

29

CASE:RIGID
ZT: 30.0 M   XR: 1000.0 M   YR: 0.0 M   ZR: 20.0 M

(a)

CASE:RIGID
ZT: 30.0 M   XR: 1000.0 M   YR: 0.0 M   ZR: 80.0 M

(b)

Figure 3.5 Rigid bottom: Output signal for Hamming-envelope CW pulse ($f_0 = 0.4$ Hz) for (a) receiver above the source and (b) receiver below the source.

TRANSMITTED PULSE
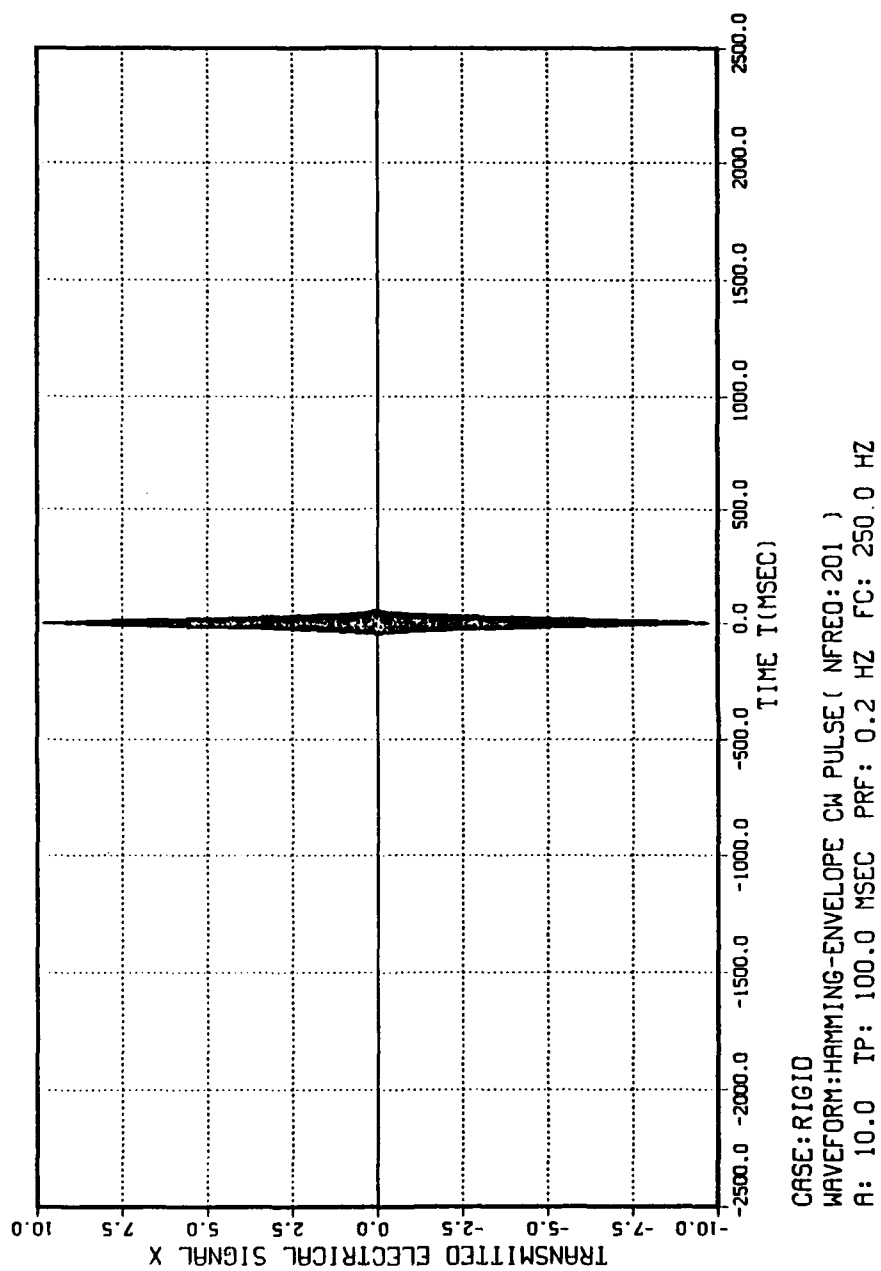
Figure 3.6 Hamming-envelope CW pulse ($f_0 = 0.2$ Hz).

$f_0 = 0.2$ Hz and for the two receiver locations are shown in Fig. 3.7.

The output electrical signals in Figs. 3.5 and 3.7 are plotted as a function of the retarded time, in msec, where the retarded time is defined as

$$t - \frac{\text{HRZRNG}}{c_2} \qquad (3-6)$$

where HRZRNG is the horizontal range between the source and the receive array, and c_2 is the speed of sound in the ocean.

It is evident from the results shown in Fig. 3.7 that the fundamental frequency $f_0 = 0.2$ Hz is not small enough to represent the overall received signal. In order to increase further the fundamental period T_0, an attempt was made of using $f_0 = 0.1$ Hz and both the transmitted and resulting output signal for the receiver above the source are shown in Fig. 3.8. Note the number of harmonics (NFREQ = 401) required to represent this transmitted pulse. However, it must be mentioned that, although this simulation case ($f_0 = 0.1$ Hz) execution was completed, an extremely large memory area and a very long computational time were required. Since it is ineffective for the purposes of the present thesis try to execute such cases, the rigid bottom model was tested for $f_0 = 0.4$ Hz and for short range cases only in the remaining test cases. The output results of the rigid bottom model for $f_0 = 0.4$ Hz are representative enough in order to compare the effectiveness of the two models.

Next, the fluid bottom results are presented. The transmitted electrical signal for $f_0 = 2.5$ Hz is shown in Fig. 3.9. The number of harmonics required to represent this pulse is NFREQ = 17. A graphical representation of the transcendental equation for the frequencies $f = 230$ Hz (lowest), $f = 250$ Hz (carrier) and $f = 270$ Hz (highest) is presented in Figs. 3.10, 3.11, and 3.12, respectively. The parameter THETAC refers to the critical angle θ_c of incidence. The values of the transcendental equation vary from $+\infty$ to $-\infty$ but, in order to present the function clearly, it has been
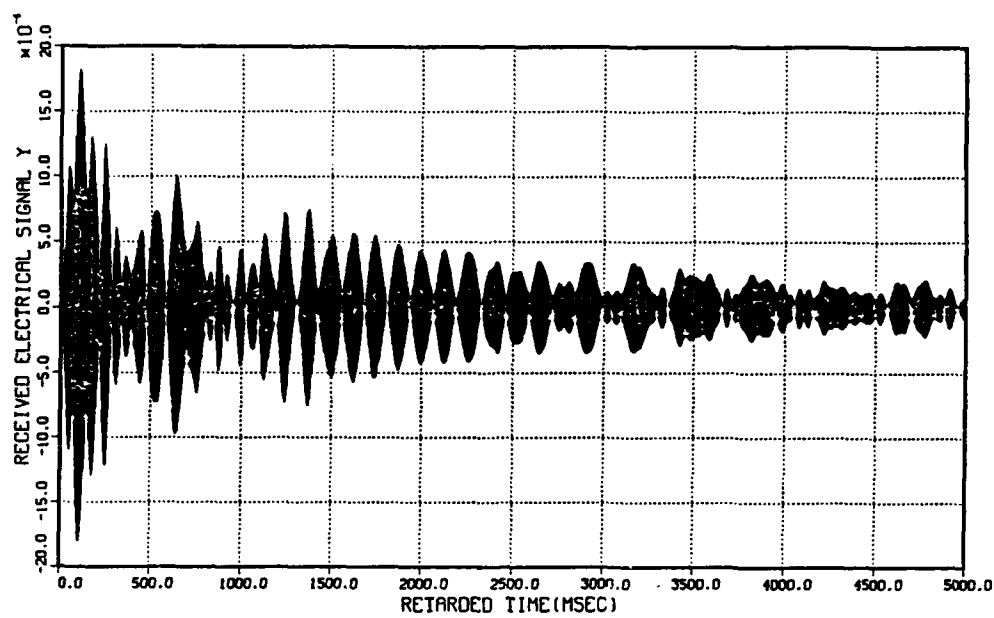
CASE:RIGID
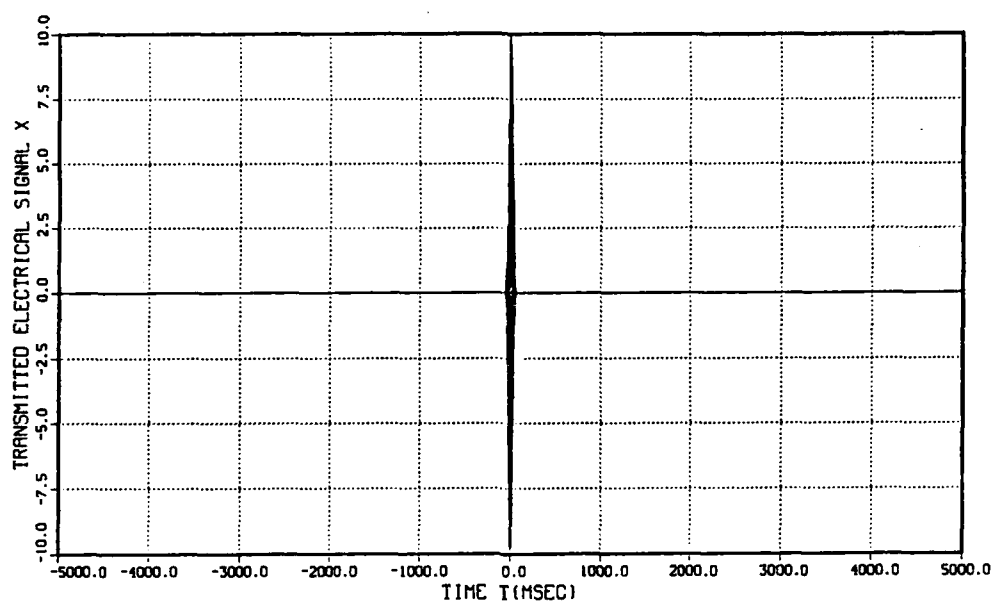ZT: 30.0 M   XR: 1000.0 M   YR: 0.0 M   ZR: 20.0 M

(a)
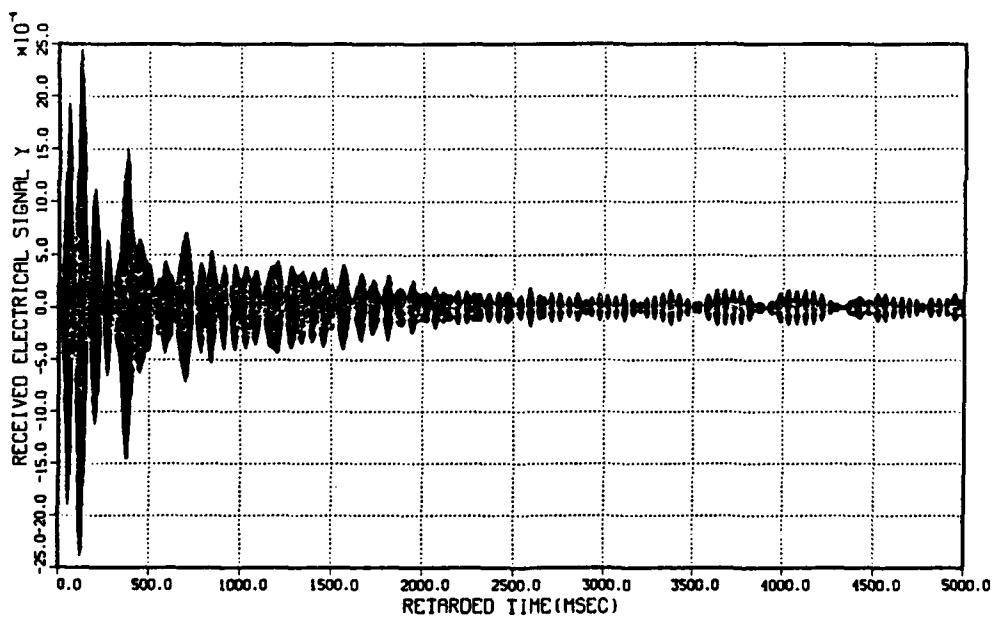
CASE:RIGID
ZT: 30.0 M   XR: 1000.0 M   YR: 0.0 M   ZR: 80.0 M

(b)

Figure 3.7 Rigid bottom: Output signal for Hamming-envelope CW pulse ($f_0 = 0.2$ Hz) for (a) receiver above the source and (b) receiver below the source.
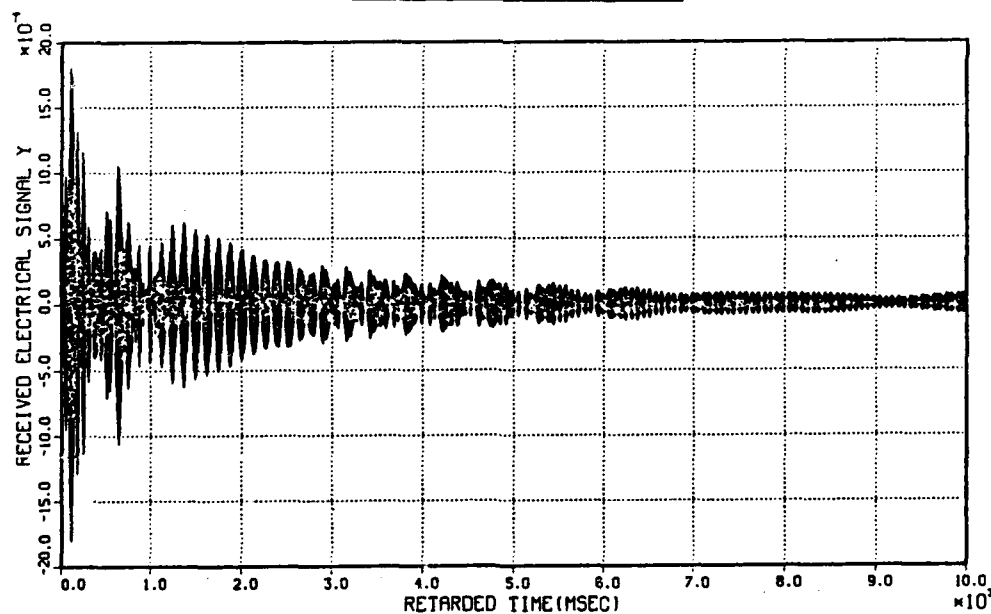
TRANSMITTED PULSE

CASE:RIGID
WAVEFORM:HAMMING-ENVELOPE CW PULSE(NFREO:401)
A: 10.0   TP: 100.0 MSEC   PRF: 0.1 HZ   FC: 250.0 HZ

(a)

OUTPUT PULSE AT ELEMENT (0,0)

CASE:RIGID
ZT: 30.0 M   XR: 1000.0 M   YR: 0.0 M   ZR: 20.0 M

(b)

Figure 3.8 Rigid bottom: (a) Hamming-envelope CW pulse ($f_0 = 0.1$ Hz) and (b) resulting output signal for the receiver above the source.
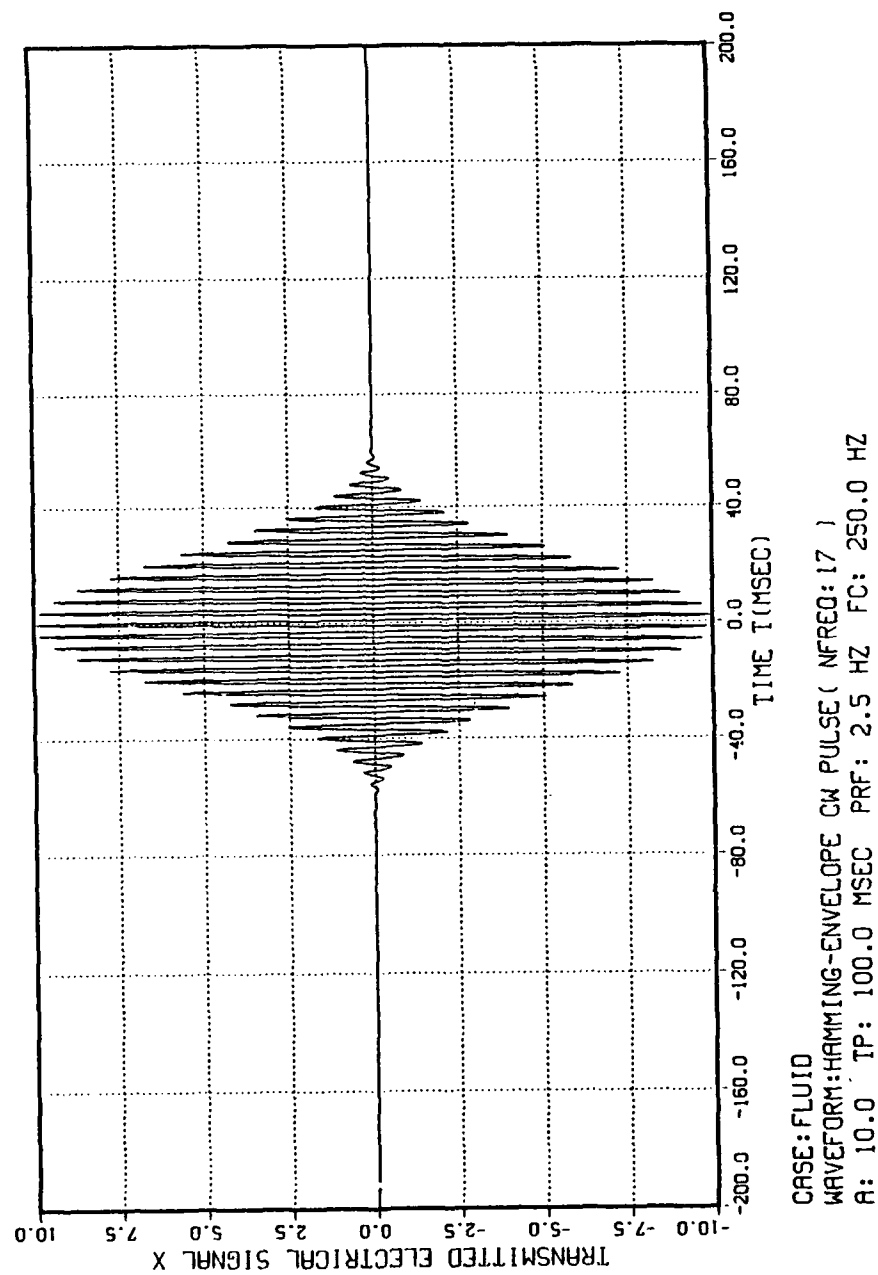
34

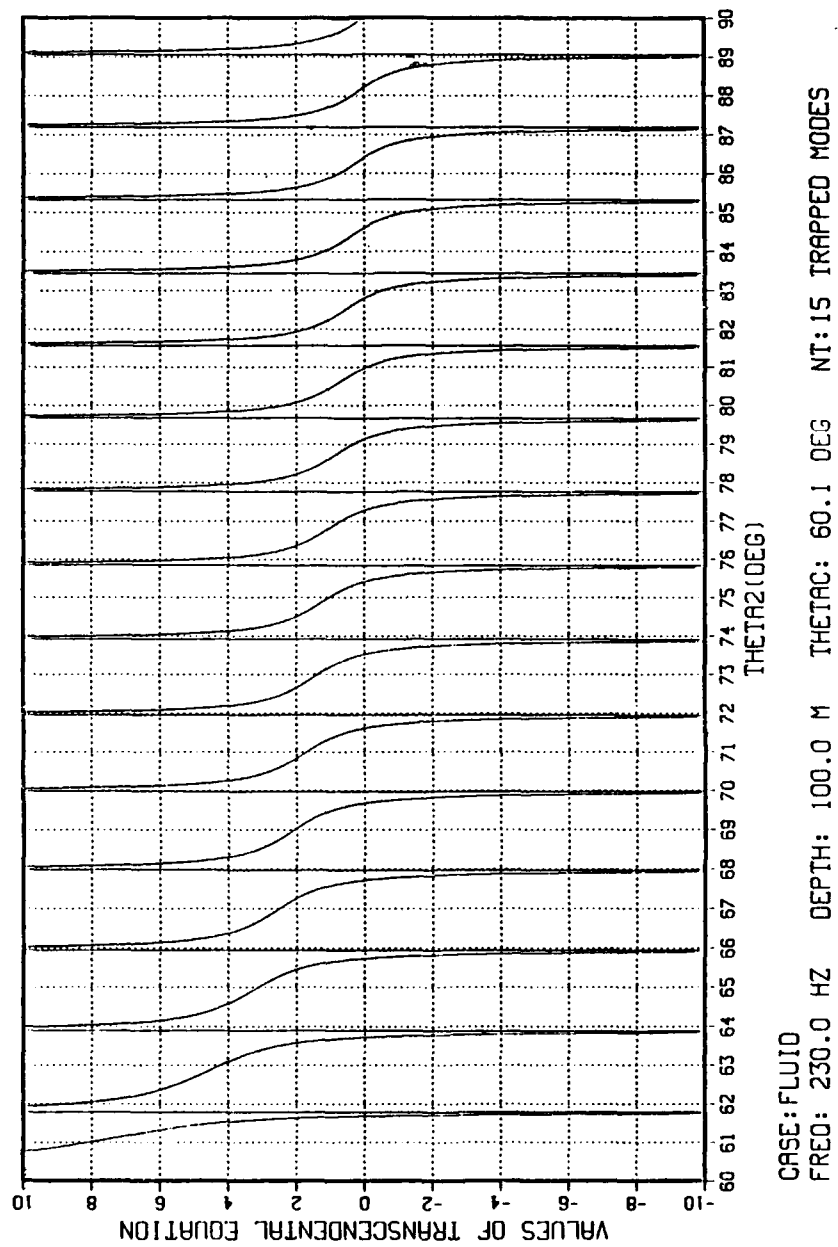Figure 3.9 Hamming-envelope CW pulse($f_0 = 2.5$ Hz).

35

Figure 3.10 Fluid bottom: Transcendental equation for the lowest frequency $f = 230$ Hz.
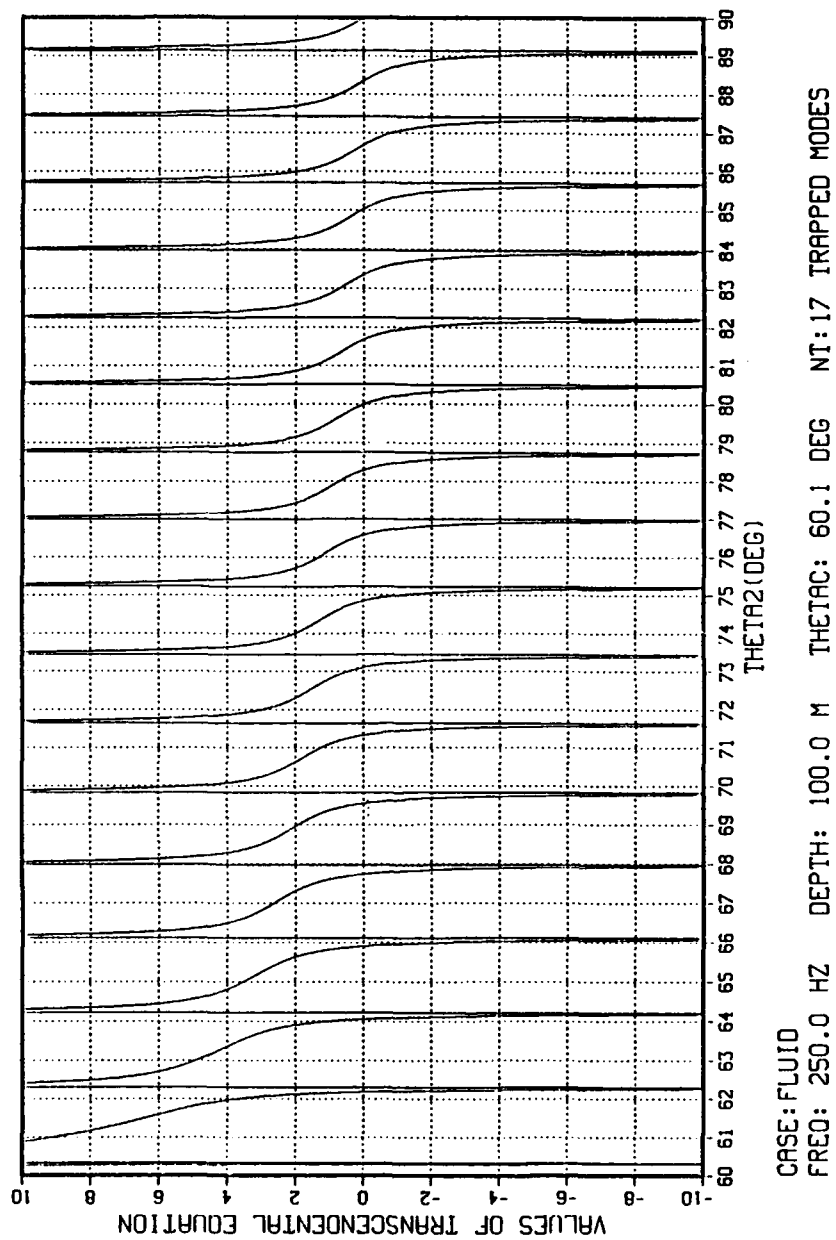
36

Figure 3.11 Fluid bottom: Transcendental equation for the carrier frequency $f = 250$ Hz.
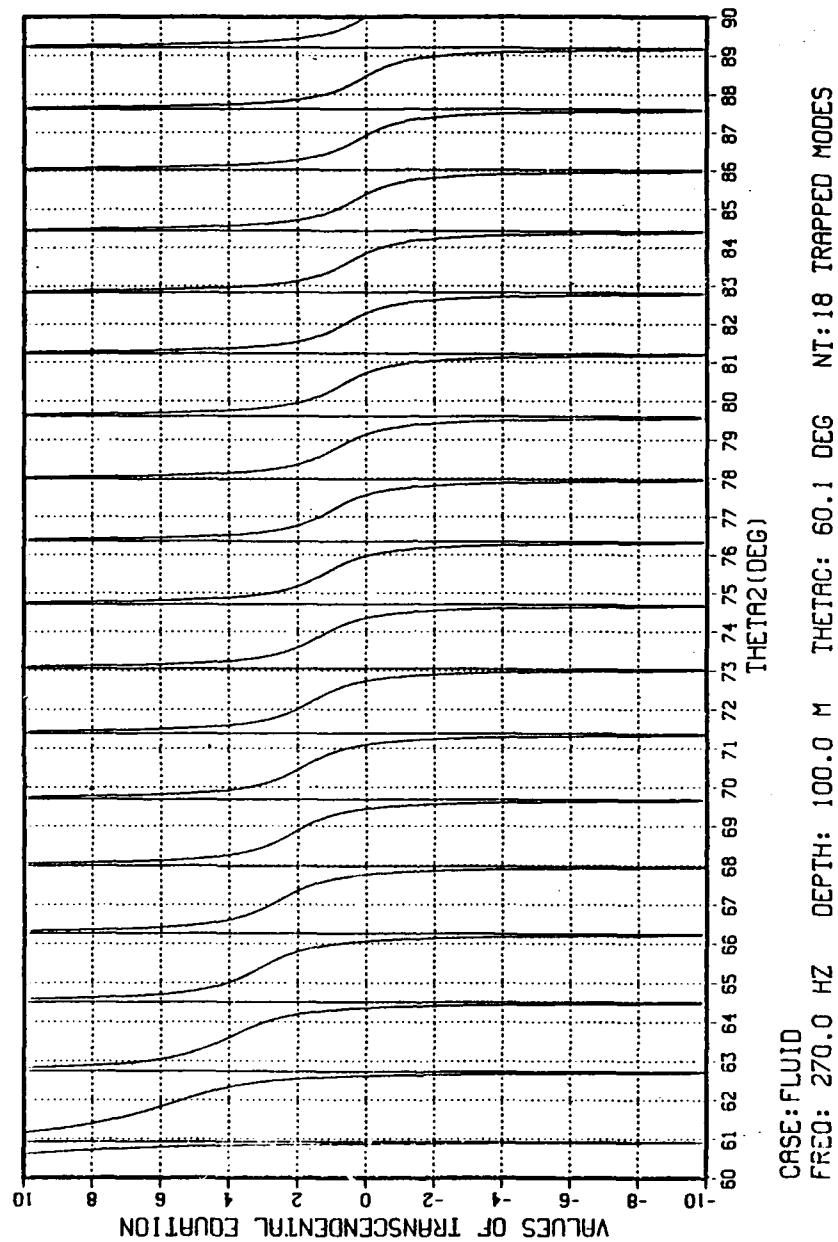
Figure 3.12 Fluid bottom: Transcendental equation for the highest frequency $f = 270$ Hz.

38

truncated in the range of $\pm$ 10. The expected locations of the roots of the equation are easily recognized at the zero-crossing points of the function. The numerical results characterizing the allowed propagating modes for the lowest frequency $f = 230$ Hz, the carrier frequency $f = 250$ Hz and the highest frequency $f = 270$ Hz are shown in Tables 3.4, 3.5 and 3.6.

The notation used in these tables and the involved parameters are as follows:

MODES: Total number of trapped modes N_t [see Eq. (2-19)]

K2: Wave number k_2 [see Eq. (2-3)]

N: Individual mode number

FN: Cutoff frequency f_n for the nth mode [see Eq. (2-18)]

THETA2N: Angle of propagation $\theta_{2,n}$ for the nth mode [see Eq. (2-14)]

KR2N: Propagation vector component $k_{r_{2,n}}$ in the radial direction for the nth mode [see Eq. (2-16)]

KZ2N: Propagation vector component $k_{z_{2,n}}$ in the z-direction for the nth mode [see Eq. (2-17)]

CGR2N: Group velocity $c_{g_{r_{2,n}}}$ in the radial direction for the nth mode [see Eq. (2-20)]

EN: Energy E_n of the nth mode [see Eq. (2-13)]

TR2N: Time of arrival $t_{r_{2,n}}$ of the nth mode [see Eq. (2-11)]

By looking at these tables, it is verified that the roots of the transcendental equation (i.e., the angles of propagation $\theta_{2,n}$, which have been numerically calculated by the computer program) agree with the expected locations determined in Figs. 3.10, 3.11, and 3.12. Note also that the propagating modes are restricted by two factors, i.e., the cutoff frequency f_n and the critical angle of incidence θ_c. Therefore, for the fluid bottom model there are no modes propagating with angles smaller than the critical angle θ_c.

39

DEPTH = 100.0 M   F = 230.0 HZ   MODES = 15   K2 = 0.96342 RAD/M

N	FN (HZ)	THETA2N (DEG)	KR2N (RAD/M)	KZ2N (RAD/M)	CGR2N (M/SEC)	EN	TR2N (SEC)
0	7.527	88.206	0.96295	0.03015	1499.265	52.089	0.666993
1	22.580	86.410	0.96153	0.06033	1497.056	52.053	0.667978
2	37.634	84.607	0.95916	0.09055	1493.360	51.999	0.669631
3	52.688	82.795	0.95581	0.12083	1488.156	51.935	0.671973
4	67.741	80.972	0.95149	0.15118	1481.417	51.869	0.675029
5	82.795	79.135	0.94615	0.18160	1473.111	51.807	0.678835
6	97.849	77.283	0.93979	0.21209	1463.202	51.756	0.683433
7	112.902	75.413	0.93237	0.24264	1451.648	51.720	0.688872
8	127.956	73.523	0.92386	0.27325	1438.404	51.704	0.695215
9	143.010	71.613	0.91424	0.30390	1423.420	51.714	0.702534
10	158.063	69.679	0.90346	0.33458	1406.639	51.758	0.710914
11	173.117	67.719	0.89149	0.36528	1388.003	51.853	0.720459
12	188.171	65.732	0.87829	0.39597	1367.449	52.037	0.731289
13	203.224	63.716	0.86382	0.42662	1344.920	52.415	0.743539
14	218.278	61.676	0.84808	0.45711	1320.415	53.500	0.757338

TABLE 3.4 Fluid bottom: Numerical results for the lowest frequency component.

40

DEPTH = 100.0 M	F = 250.0 HZ	MODES = 17		K2 = 1.04720 RAD/M			
N	FN (HZ)	THETA2N (DEG)	KR2N (RAD/M)	KZ2N (RAD/M)	CGR2N (M/SEC)	EN	TR2N (SEC)
0	7.527	88.345	1.04676	0.03025	1499.374	51.924	0.666945
1	22.580	86.687	1.04545	0.06052	1497.493	51.895	0.667783
2	37.634	85.025	1.04325	0.09082	1494.348	51.852	0.669188
3	52.688	83.355	1.04016	0.12117	1489.924	51.799	0.671175
4	67.741	81.677	1.03617	0.15158	1484.202	51.743	0.673763
5	82.795	79.988	1.03125	0.18205	1477.159	51.688	0.676975
6	97.849	78.287	1.02539	0.21258	1468.768	51.639	0.680843
7	112.902	76.573	1.01857	0.24317	1458.999	51.601	0.685402
8	127.956	74.843	1.01077	0.27381	1447.819	51.576	0.690694
9	143.010	73.096	1.00195	0.30449	1435.192	51.567	0.696771
10	158.063	71.331	0.99210	0.33521	1421.076	51.580	0.703692
11	173.117	69.546	0.98117	0.36595	1405.429	51.621	0.711526
12	188.171	67.739	0.96915	0.39670	1388.203	51.704	0.720356
13	203.224	65.909	0.95598	0.42745	1369.347	51.854	0.730275
14	218.278	64.054	0.94165	0.45817	1348.814	52.142	0.741392
15	233.332	62.177	0.92613	0.48878	1326.586	52.832	0.753815
16	248.385	60.298	0.90961	0.51888	1302.915	59.207	0.767510

TABLE 3.5 Fluid bottom: Numerical results for the carrier frequency component.

41

N	FN (HZ)	THETA2N (DEG)	KR2N (RAD/M)	KZ2N (RAD/M)	CGR2N (M/SEC)	EN	TR2N (SEC)
0	7.527	88.463	1.13057	0.03033	1499.460	51.782	0.666907
1	22.580	86.924	1.12934	0.06068	1497.839	51.759	0.667628
2	37.634	85.382	1.12730	0.09106	1495.130	51.724	0.668838
3	52.688	83.834	1.12443	0.12147	1491.323	51.680	0.670546
4	67.741	82.279	1.12072	0.15194	1486.403	51.632	0.672765
5	82.795	80.716	1.11616	0.18245	1480.352	51.584	0.675515
6	97.849	79.143	1.11073	0.21302	1473.153	51.539	0.678816
7	112.902	77.560	1.10442	0.24364	1464.781	51.501	0.682696
8	127.956	75.964	1.09720	0.27430	1455.213	51.472	0.687185
9	143.010	74.354	1.08907	0.30501	1444.421	51.455	0.692319
10	158.063	72.730	1.07999	0.33576	1432.375	51.452	0.698141
11	173.117	71.090	1.06993	0.36653	1419.043	51.467	0.704700
12	188.171	69.432	1.05888	0.39732	1404.388	51.505	0.712054
13	203.224	67.756	1.04681	0.42813	1388.373	51.577	0.720267
14	218.278	66.060	2.03368	0.45893	1370.957	51.702	0.729418
15	233.332	64.343	1.01946	0.48970	1352.100	51.928	0.739590
16	248.385	62.605	1.00414	0.52039	1331.779	52.410	0.750875
17	263.439	60.853	0.98776	0.55084	1310.060	54.263	0.763324

DEPTH = 100.0 M   F = 270.0 HZ   MODES = 18   K2 = 1.13097 RAD/M

TABLE 3.6 Fluid bottom: Numerical results for the highest frequency component.

The complex acoustic pressure field (magnitude and phase) across the elements of the receive array for the carrier frequency and the two locations of the receiver are shown in Fig. 3.13 and 3.14. It is shown again that the depth of the receiver has a definite effect in the resulting acoustic pressure field.

The resulting output pulses at the center element of the array for the two cases are shown in Fiq. 3.15. The duration of the resulting output pulse is about 200 msec long, while for the rigid bottom model a time window of length 10 sec is not long enough to present the complete output signal for that model. The reason is that the number of allowed propagating modes for the rigid bottom model are about twice as many as for the fluid bottom model. As a result, it takes these additional modes in the rigid bottom model longer to reach the receiver.

In order to investigate further the efficiency of the fluid bottom model, the long range results are presented next. The transmitted signal for $f_0 = 0.8$ Hz is shown in Fig. 3.16. The number of harmonics for this case is NFREQ = 51. The acoustic pressure field (magnitude and phase) across the receiver for the carrier frequency and for the two depths of the receiver is shown in Fiq. 3.17 and 3.18.

The resulting output pulses at the center element of the array for the two depths of the receiver are shown in Fig. 3.19. The duration of the output pulse is about 1000 msec long. Therefore, the output pulse is 10 times longer than the transmitted pulse ($T_P = 100$ msec). The shape of the transmitted pulse is distorted at the receiver due to dispersion effects. These effects are more evident in the long range case compared to the short range results shown in Fig. 3.15. It is also interesting to observe how different the shape of the output pulse is at the same range but at two differrent receiver depths.
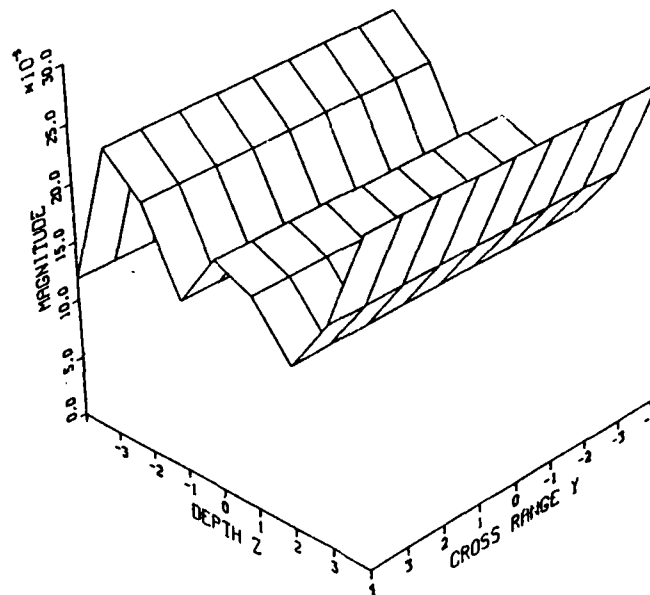
43

CASE:FLUID   FREQUENCY: 250.0 HZ

ZT: 30.0 M   XR: 1000.0 M   YR: 0.0 M   ZR: 20.0 M

(a)
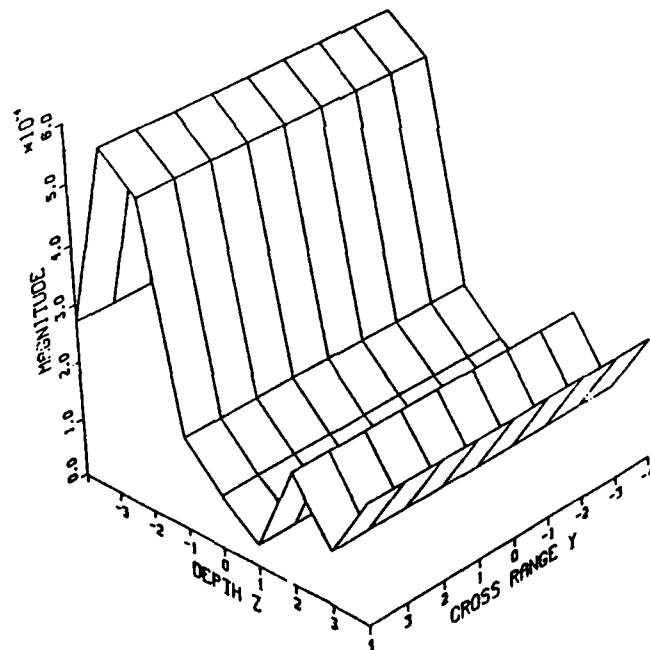
CASE:FLUID   FREQUENCY: 250.0 HZ

ZT: 30.0 M   XR: 1000.0 M   YR: 0.0 M   ZR: 80.0 M

(b)

Figure 3.13 Fluid bottom: Magnitude of the complex acoustic pressure field for Hamming-envelope CW pulse for (a) receiver above the source and (b) receiver below the source.
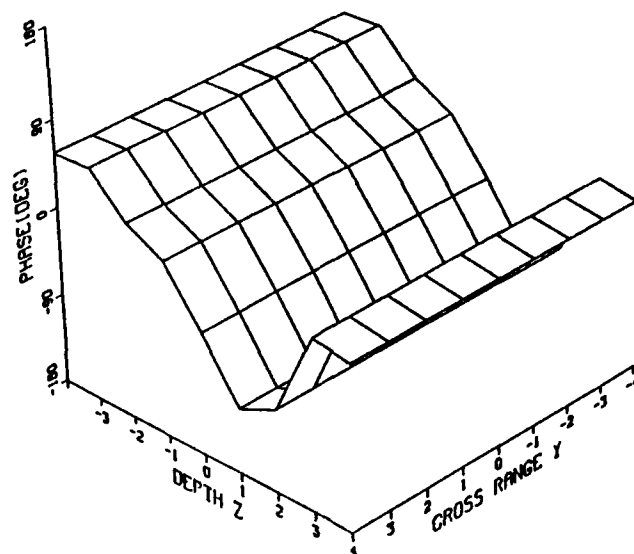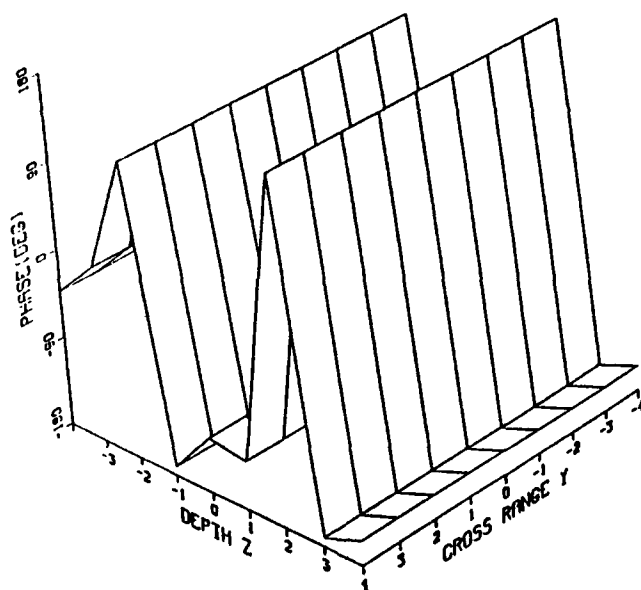
CASE:FLUID   FREQUENCY: 250.0 HZ

ZT: 30.0 M   XR: 1000.0 M   YR: 0.0 M   ZR: 20.0 M

(a)
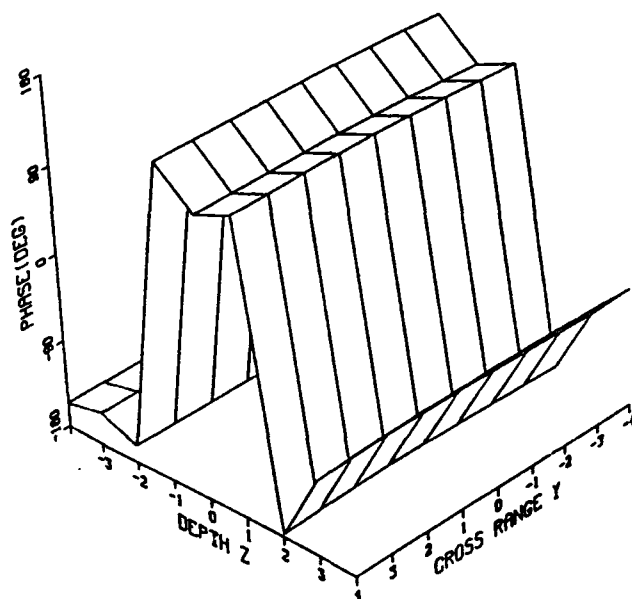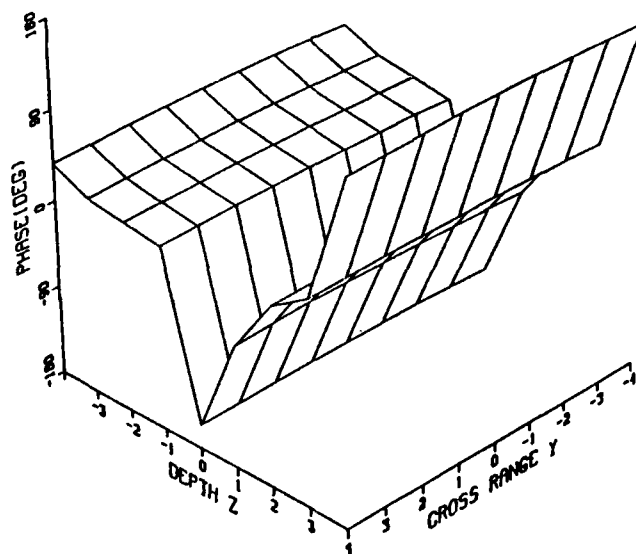
CASE:FLUID   FREQUENCY: 250.0 HZ

ZT: 30.0 M   XR: 1000.0 M   YR: 0.0 M   ZR: 80.0 M

(b)

Figure 3.14 Fluid bottom: Phase of the complex acoustic pressure field
for Hamming-envelope CW pulse for (a) receiver above the source and (b)
receiver below the source.

45

OUTPUT PULSE AT ELEMENT (0,0)

CASE:FLUID
ZT: 30.0 M   XR: 1000.0 M   YR: 0.0 M   ZR: 20.0 M

(a)

CASE:FLUID
ZT: 30.0 M   XR: 1000.0 M   YR: 0.0 M   ZR: 80.0 M
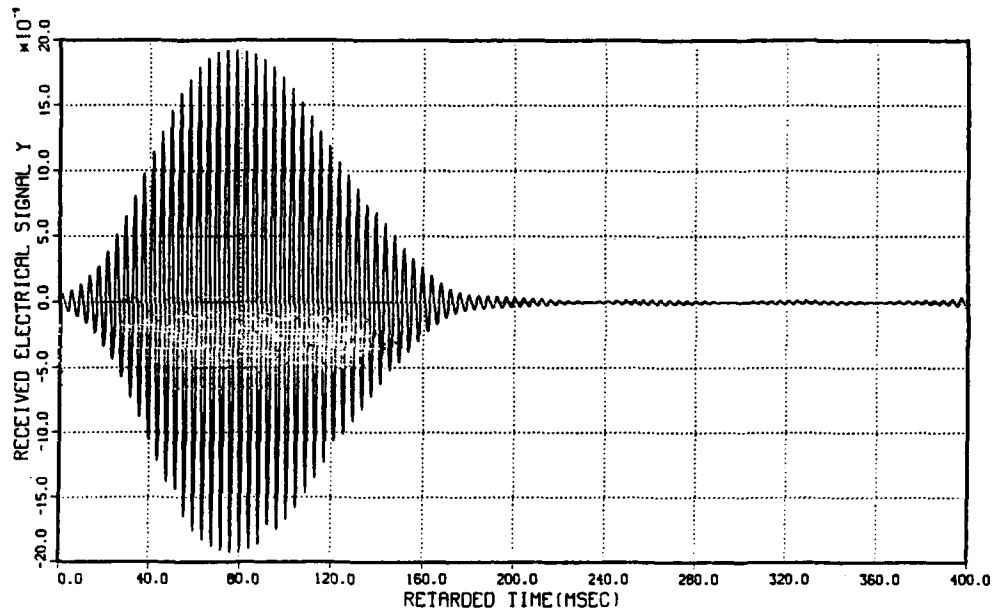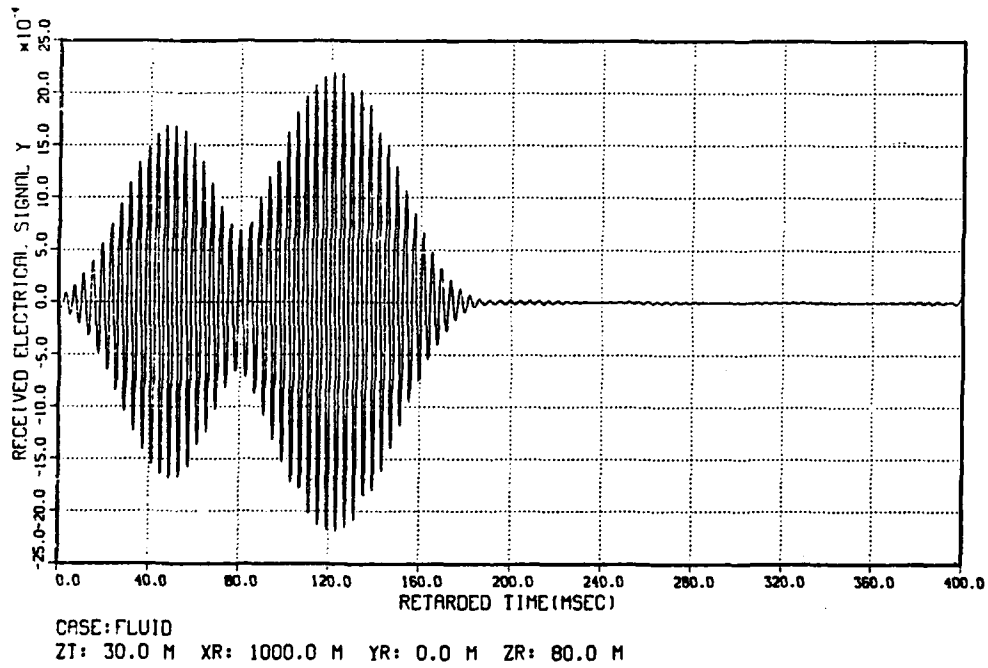
(b)

Figure 3.15 Fluid bottom: Output signal for Hamming-envelope CW pulse ($f_0 = 2.5$ Hz) for (a) receiver above the source and (b) receiver below the source.

46
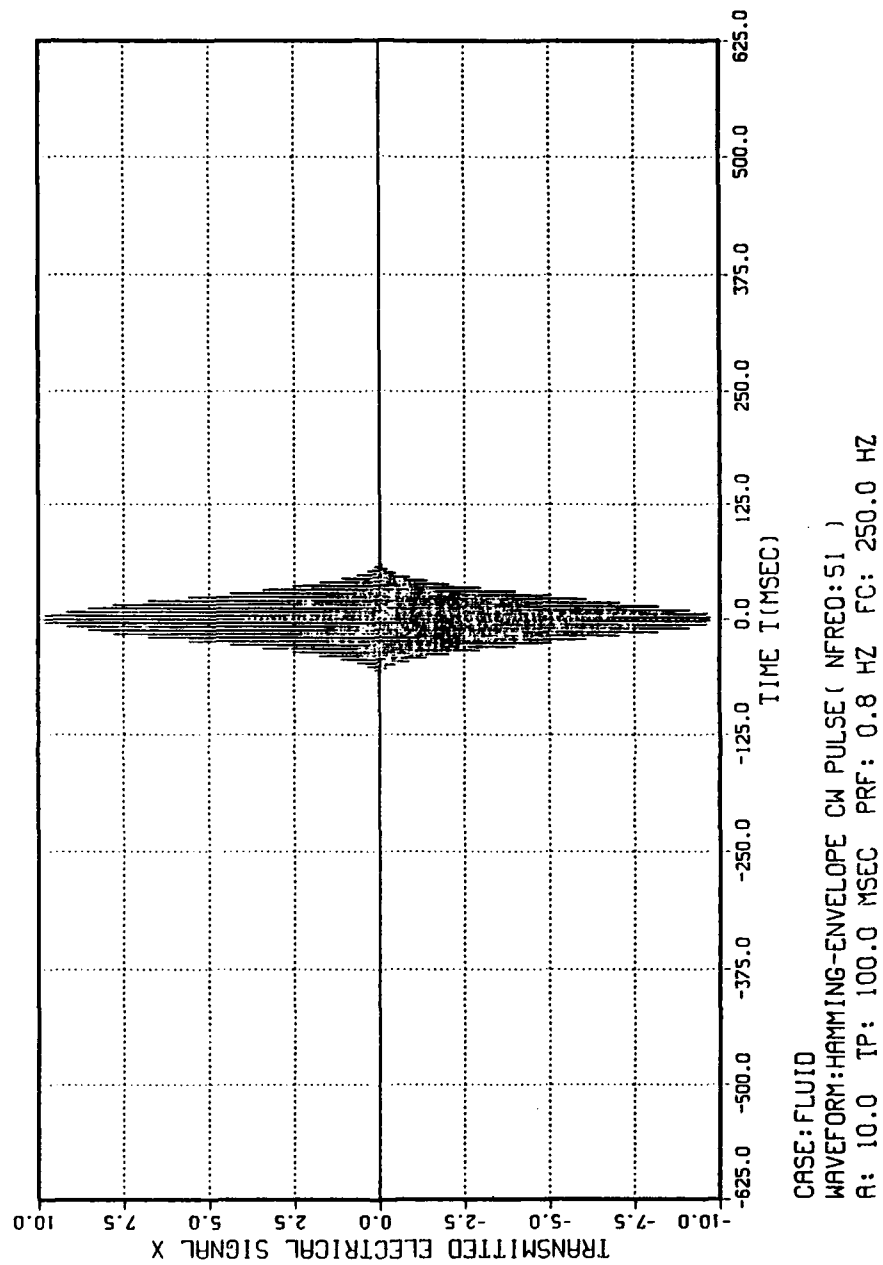
Figure 3.16 Hamming-envelope CW pulse ($f_0 = 0.8$ Hz).
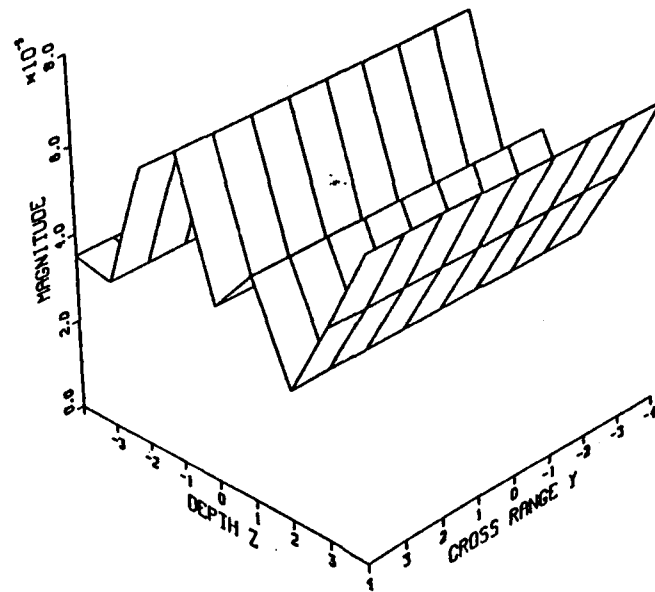
47

CASE:FLUID   FREQUENCY: 250.0 HZ

ZT: 30.0 M   XR: 10000.0 M   YR: 0.0 M   ZR: 20.0 M

(a)
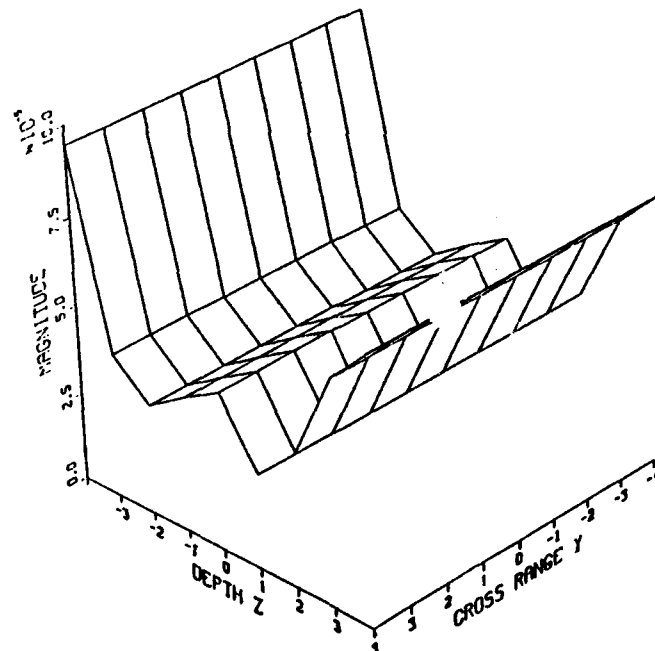
CASE:FLUID   FREQUENCY: 250.0 HZ

ZT: 30.0 M   XR: 10000.0 M   YR: 0.0 M   ZR: 80.0 M

(b)

Figure 3.17 Fluid bottom: Magnitude of the complex acoustic pressure field for Hamming-envelope CW pulse for (a) receiver above the source and (b) receiver below the source.

48

CASE: FLUID   FREQUENCY: 250.0 HZ

ZT: 30.0 M   XR: 10000.0 M   YR: 0.0 M   ZR: 20.0 M

(a)

CASE: FLUID   FREQUENCY: 250.0 HZ

ZT: 30.0 M   XR: 10000.0 M   YR: 0.0 M   ZR: 80.0 M

(b)

Figure 3.18 Fluid bottom: Phase of the complex acoustic pressure field for Hamming-envelope CW pulse for (a) receiver above the source and (b) receiver below the source.

49

CASE: FLUID
ZT: 30.0 M   XR: 10000.0 M   YR: 0.0 M   ZR: 20.0 M

(a)

CASE: FLUID
ZT: 30.0 M   XR: 10000.0 M   YR: 0.0 M   ZR: 80.0 M
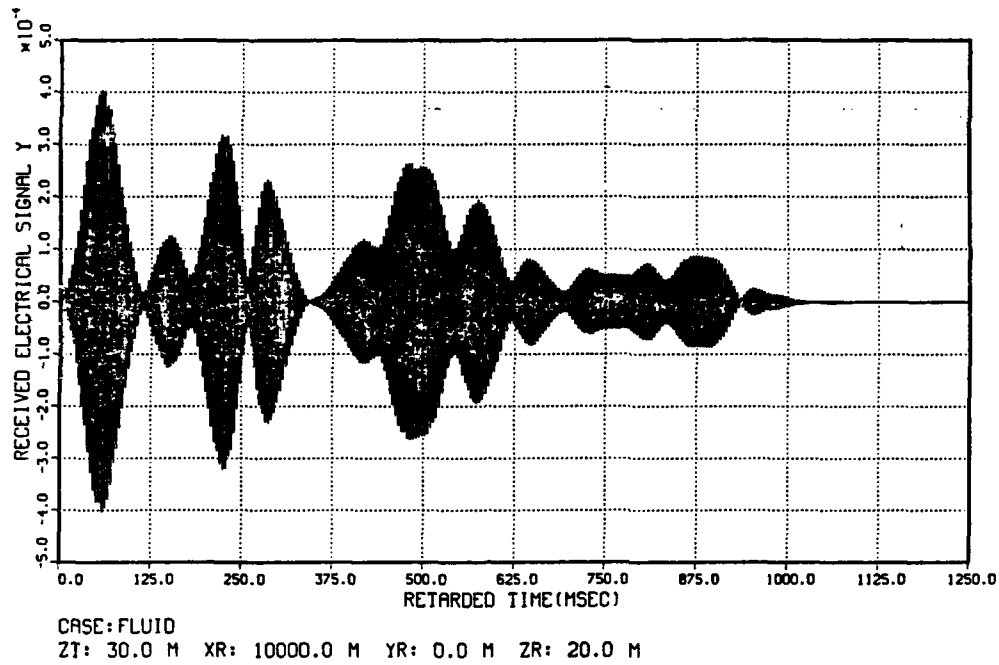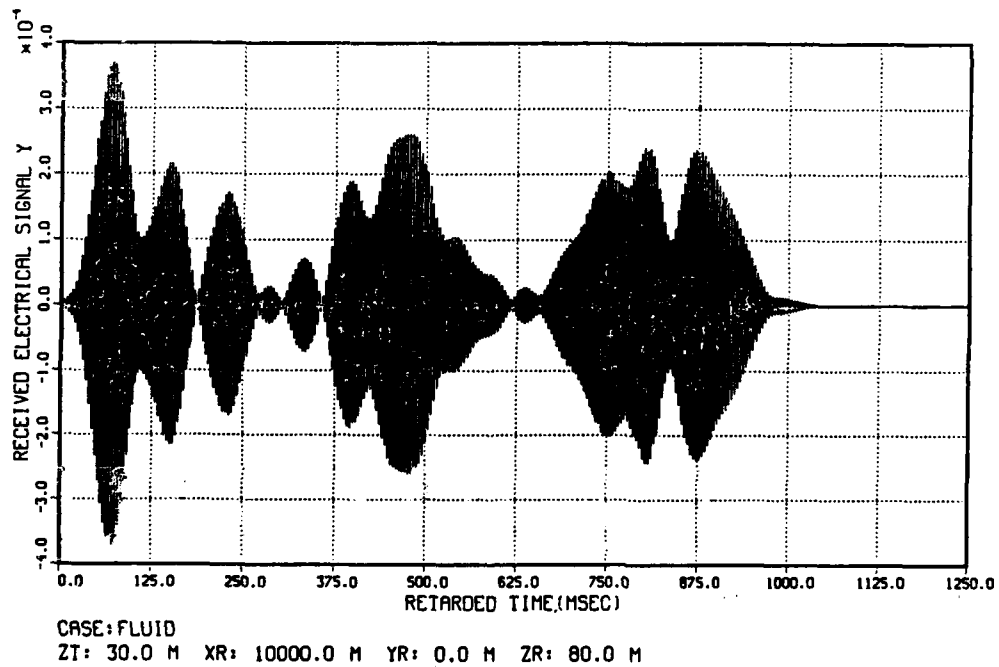
(b)

Figure 3.19 Fluid bottom: Output signal for Hamming-envelope CW pulse ($f_0 = 0.8$ Hz) for (a) receiver above the source and (b) receiver below the source.

50

2. Linear-frequency-modulated (LFM) pulse

The transmitted electrical signal is a Hamming-envelope LFM pulse and it is shown in Fig. 3.20. The characteristics of the pulse and the notation are the same as for the CW pulse case. Additionally, the parameter SWPTBW refers to the *swept bandwidth* of the LFM pulse and the parameter CHIRP defines whether the pulse is an "up chirp" or "down chirp". The transmitted pulse is an "up chirp" with SWPTBW = 80.0 Hz. For the pulse shown in Fig. 3.20, more harmonics are required to represent its complex envelope (NFREQ = 301) compared to the CW pulse shown in Fig. 3.2. This implies that the computer simulation of an LFM pulse is more complicated and more computation time is required for the program execution than for the CW pulse case.

Next, the rigid bottom model results for the short range case are presented. The transmitted Hamming-envelope LFM pulse for $f_0 = 0.4$ Hz is shown in Fig. 3.20. The complex acoustic pressure field across the elements of the receive array for the carrier frequency and for the two locations of the receiver are presented by the 3-D plots in Fig. 3.21 and 3.22.

The resulting output time-domain pulses from the center element of the receive array and for the two receiver locations are shown in Fig. 3.23. These results are similar to the Hamming-envelope CW pulse, i.e., the duration of the resulting pulse is too long to fit into this time window of length $T_0 = 1/f_0 = 2500$ msec. Again, there are some modes propagating at very small angles and, as a result, these modes need a long time to reach the receiver.

Next, the fluid bottom model results are presented. The transmitted electrical signal for the short range case is shown in Fig. 3.24. For this case the number of harmonics is NFREQ = 49. The lowest frequency is $f = 190$ Hz and the highest is $f = 310$ Hz. The complex acoustic pressure field (magnitude and phase) across the
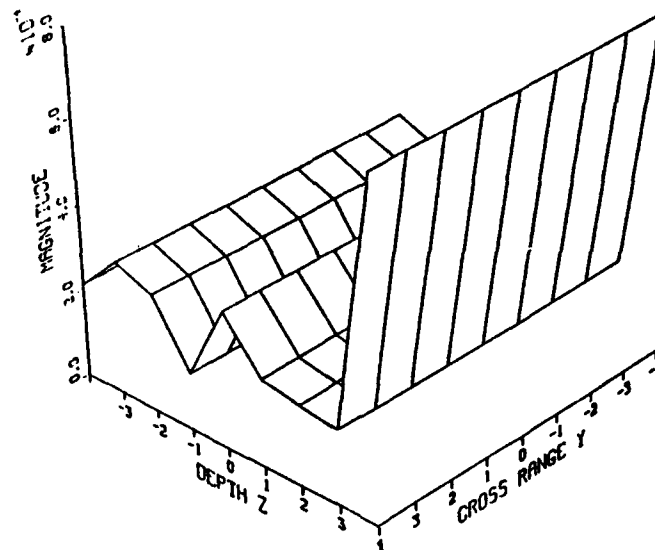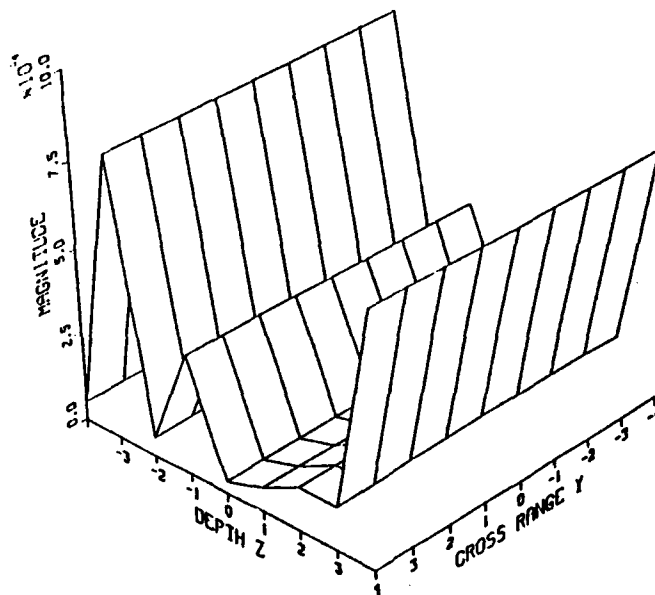
51
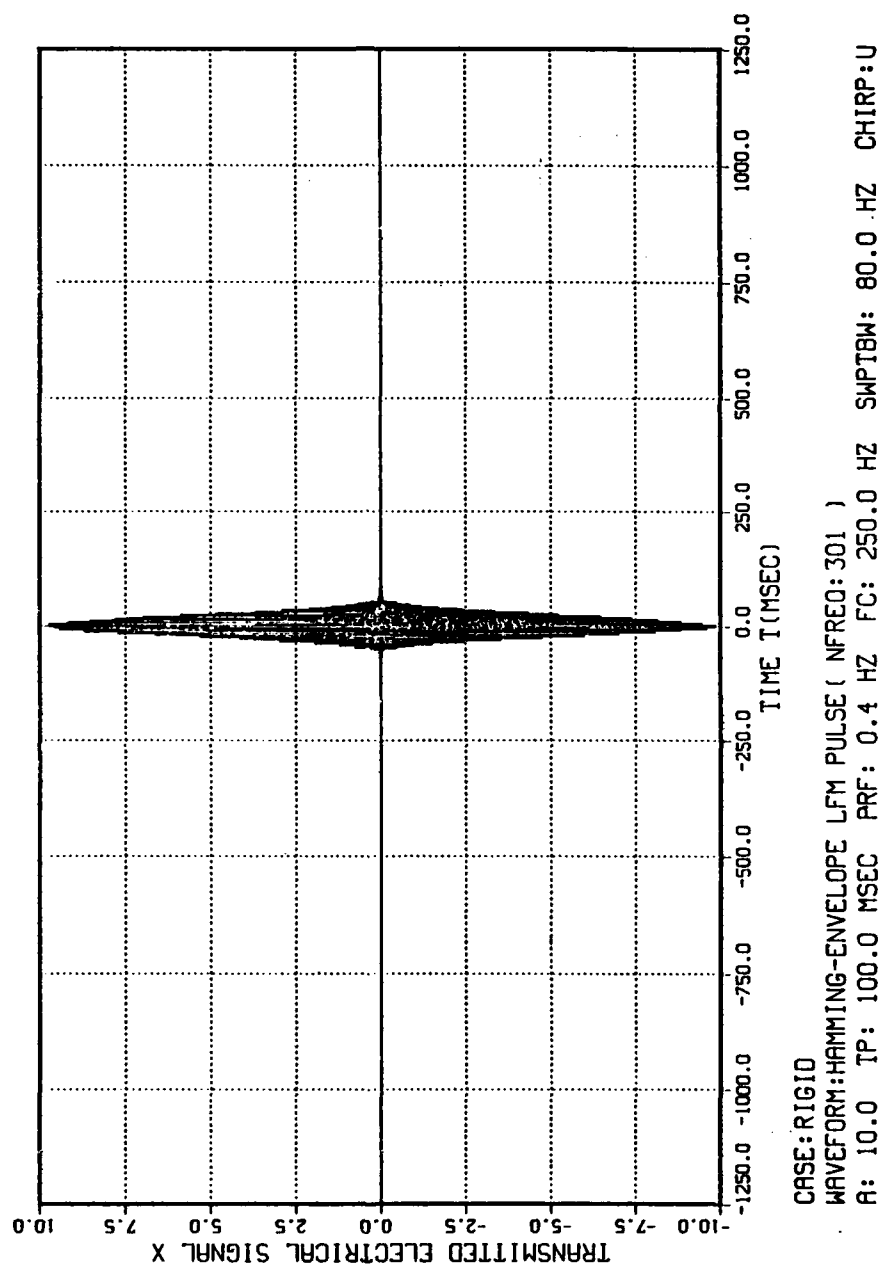
Figure 3.20 Hamming-envelope LFM pulse ($f_0 = 0.4$ Hz).

CASE: RIGID   FREQUENCY: 250.0 HZ

ZT: 30.0 M   XR: 1000.0 M   YR: 0.0 M   ZR: 20.0 M
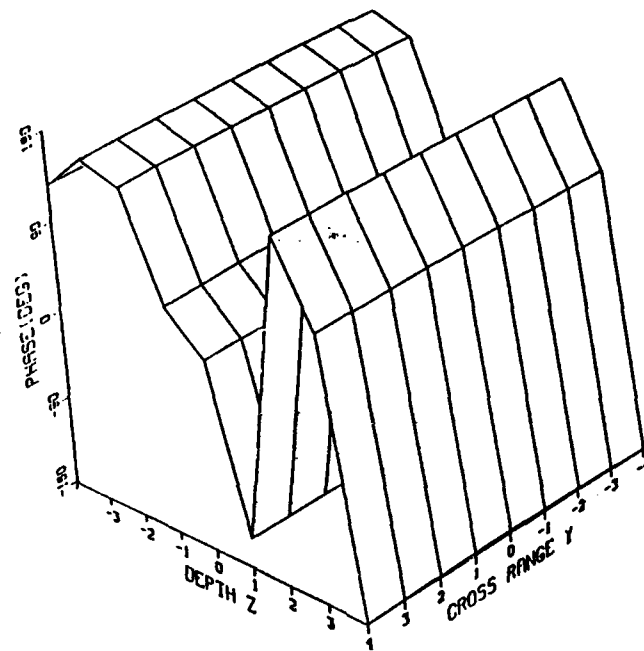
(a)

CASE: RIGID   FREQUENCY: 250.0 HZ

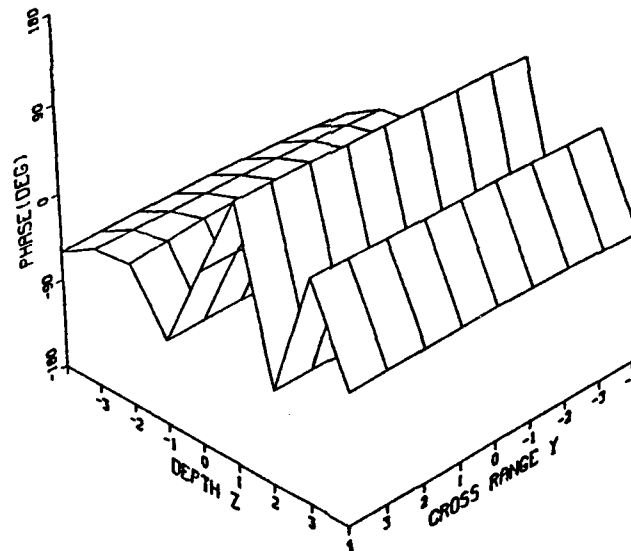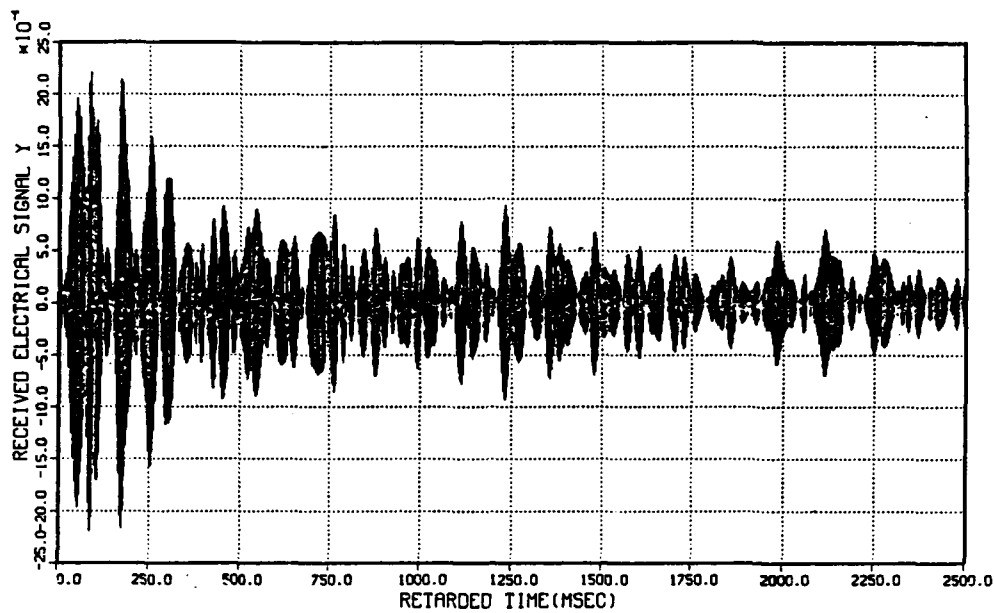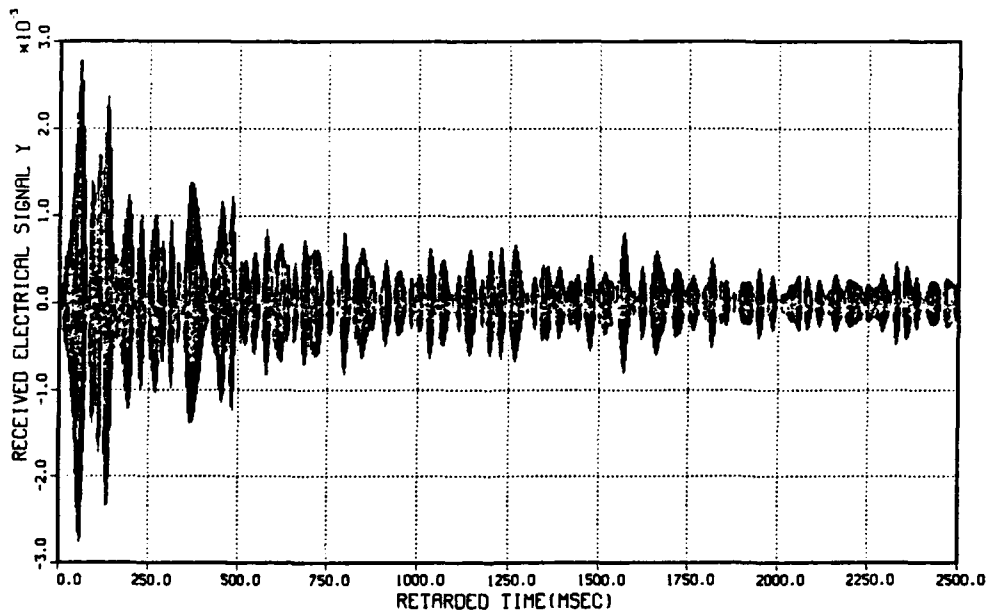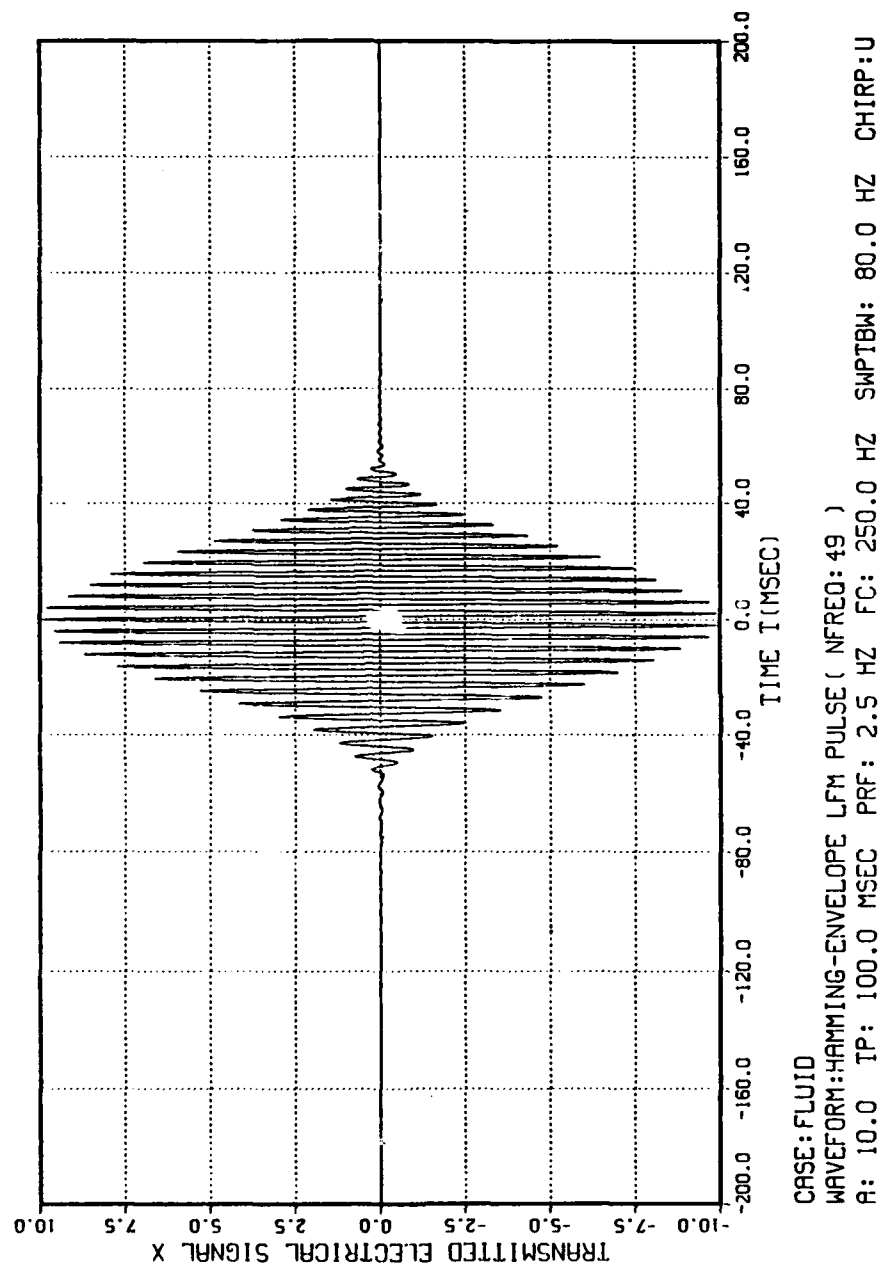ZT: 30.0 M   XR: 1000.0 M   YR: 0.0 M   ZR: 30.0 M

(b)

Figure 3.21 Rigid bottom: Magnitude of the complex acoustic pressure field for Hamming-envelope LFM pulse for (a) receiver above the source and (b) receiver below the source.

53

CASE: RIGID   FREQUENCY: 250.0 HZ

ZT: 30.0 M   XR: 1000.0 M   YR: 0.0 M   ZR: 20.0 M

(a)

CASE: RIGID   FREQUENCY: 250.0 HZ

ZT: 30.0 M   XR: 1000.0 M   YR: 0.0 M   ZR: 80.0 M

(b)

Figure 3.22 Rigid bottom: Phase of the complex acoustic pressure field for Hamming-envelope LFM pulse for (a) receiver above the source and (b) receiver below the source.

54

CASE:RIGID
ZT: 30.0 M   XR: 1000.0 M   YR: 0.0 M   ZR: 20.0 M

(a)

CASE:RIGID
ZT: 30.0 M   XR: 1000.0 M   YR: 0.0 M   ZR: 80.0 M

(b)

Figure 3.23 Rigid bottom: Output signal for Hamming-envelope LFM pulse ($f_0 = 0.4$ Hz) for (a) receiver above the source and (b) receiver below the source.

55

TRANSMITTED PULSE

CASE:FLUID
WAVEFORM:HAMMING-ENVELOPE LFM PULSE (NFREQ:49)
A: 10.0   TP: 100.0 MSEC   PRF: 2.5 HZ   FC: 250.0 HZ   SWPTBW: 80.0 HZ   CHIRP:U

Figure 3.24 Hamming-envelope LFM pulse ($f_0 = 2.5$ Hz).

56

receiver for the carrier frequency and for the two receiver depths is shown in Fig. 3.25 and 3.26.

The resulting output pulses at the center element of the receive array are shown in Fig. 3.27. The output pulse is about 200 msec long and it is twice as long as the transmitted pulse (Fig. 3.24), due to dispersion effects. Note again that the depth where the receiver is located affects greatly the shape of the received signal.

The fluid bottom model results for the propagation of a Hamming-envelope LFM pulse for the long range case are presented next. The transmitted electrical signal for $f_0 = 0.8$ Hz is shown in Fig. 3.28. For this case, the number of harmonics is NFREQ = 151. The complex acoustic pressure field (magnitude and phase) across the receive array for the carrier frequency and the two receiver depths is shown in Fig. 3.29 and 3.30.

The resulting output pulses at the center element of the receiver for the two receiver locations are shown in Fig. 3.31. The output pulse is approximately 1000 msec long as for the Hamming-envelope CW pulse in the long range case. The dispersion effects and the distortion are again more evident in the long range case compared to of the short range case.

The performance of both models (i.e., the rigid bottom and the fluid bottom) for the propagation of the two different pulses (i.e., the CW and the LFM pulse) with the same envelope function (i.e., the Hamming-envelope) has been investigated in this section. Based on the computer simulation results, the conclusions are (i) CW pulse propagation is easier to implement than LFM pulse propagation since less harmonics are involved in the CW pulse representation, (ii) the depth of the receiver affects the shape of the output signal and the complex acoustic field across the array elements, (iii) the transmitted electrical pulse is distorted at the receiver due to dispersion effects, and these are more evident in the long range case, and (iv)
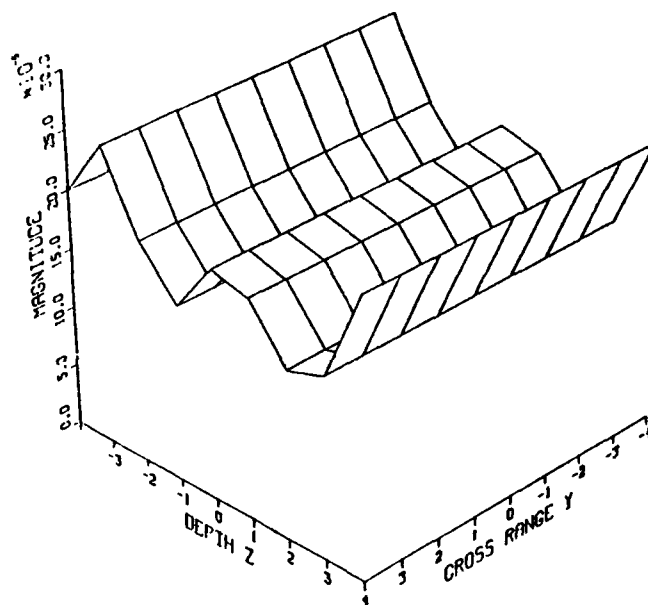
57

CASE:FLUID   FREQUENCY: 250.0 HZ

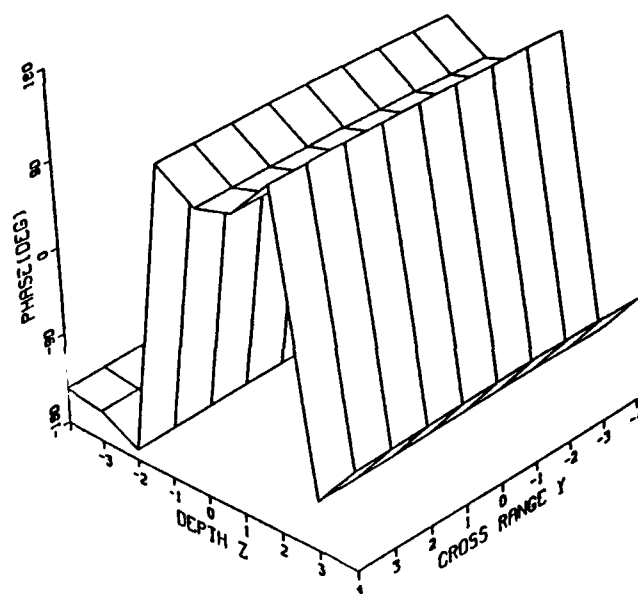ZT: 30.0 M   XR: 1000.0 M   YR: 0.0 M   ZR: 20.0 M

(a)
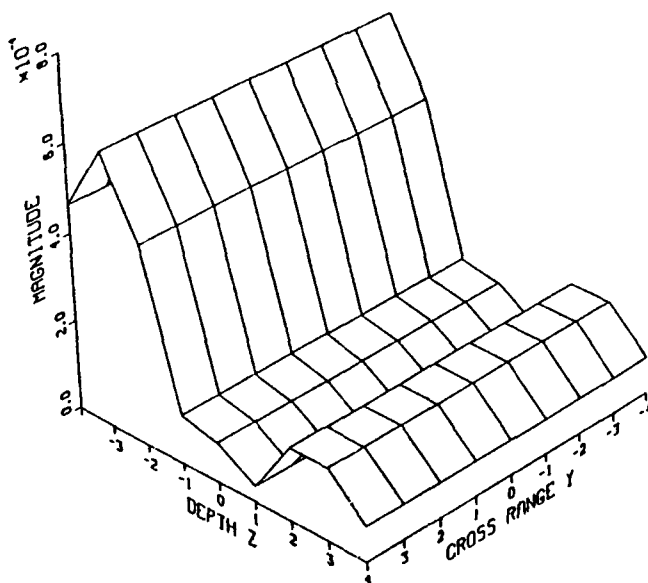
CASE:FLUID   FREQUENCY: 250.0 HZ

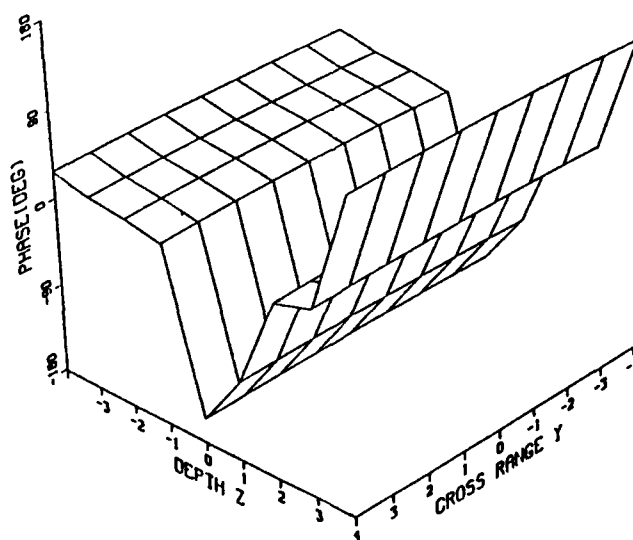ZT: 30.0 M   XR: 1000.0 M   YR: 0.0 M   ZR: 80.0 M

(b)

Figure 3.25 Fluid bottom: Magnitude of the complex acoustic pressure field for Hamming-envelope LFM pulse for (a) receiver above the source and (b) receiver below the source.

CASE:FLUID   FREQUENCY: 250.0 HZ
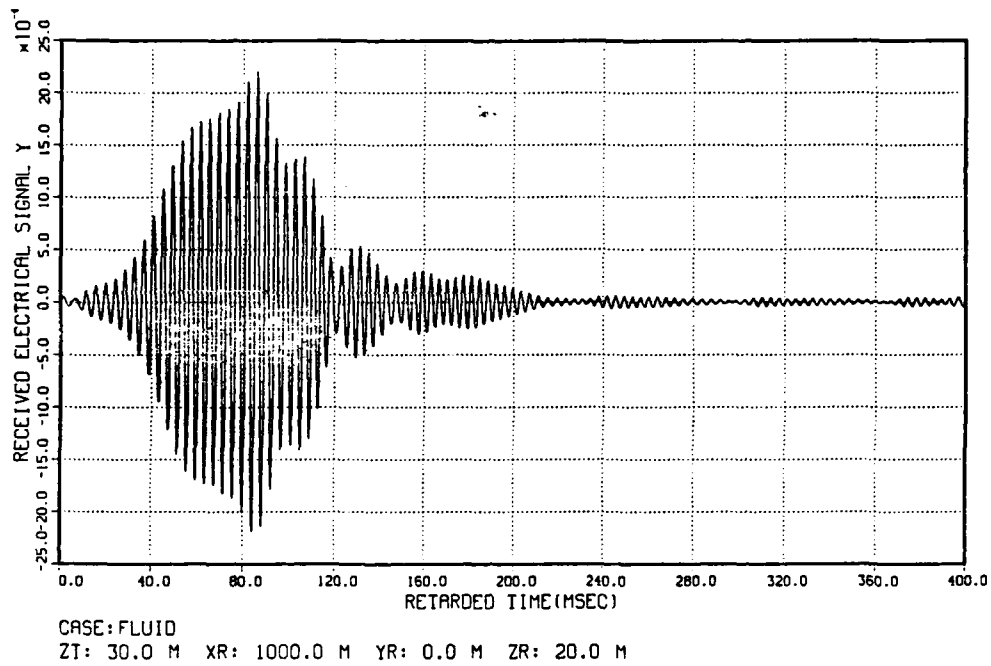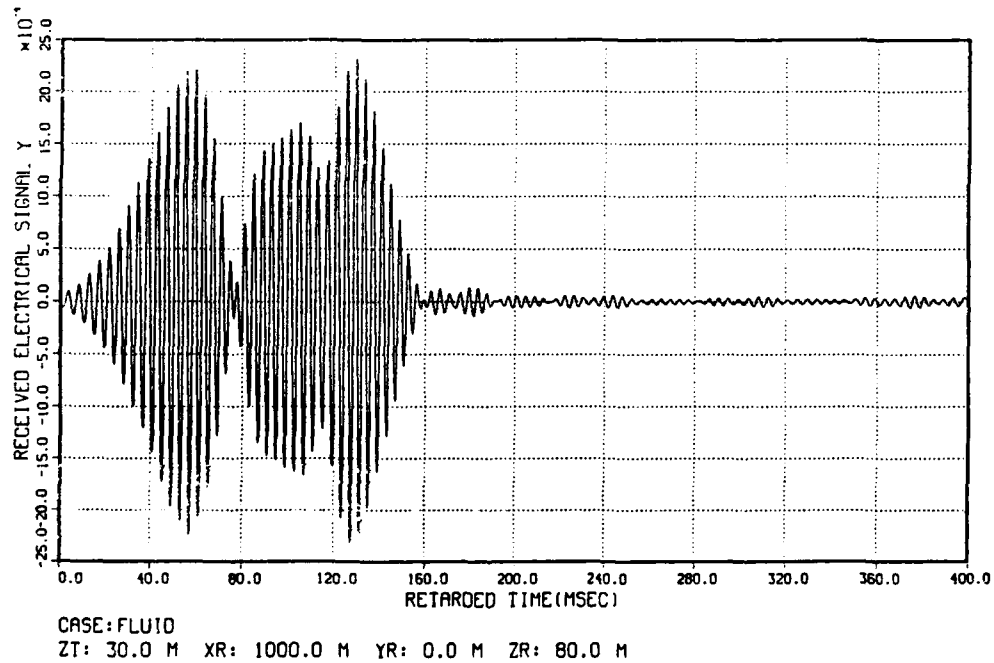
ZT: 30.0 M   XR: 1000.0 M   YR: 0.0 M   ZR: 20.0 M

(a)

CASE:FLUID   FREQUENCY: 250.0 HZ

ZT: 30.0 M   XR: 1000.0 M   YR: 0.0 M   ZR: 80.0 M

(b)

Figure 3.26 Fluid bottom: Phase of the complex acoustic pressure field for Hamming-envelope LFM pulse for (a) receiver above the source and (b) receiver below the source.

59

CASE:FLUID
ZT: 30.0 M   XR: 1000.0 M   YR: 0.0 M   ZR: 20.0 M

(a)

CASE:FLUID
ZT: 30.0 M   XR: 1000.0 M   YR: 0.0 M   ZR: 80.0 M

(b)

Figure 3.27 Fluid bottom: Output signal for Hamming-envelope LFM pulse (f_0 = 2.5 Hz) for (a) receiver above the source and (b) receiver below the source.
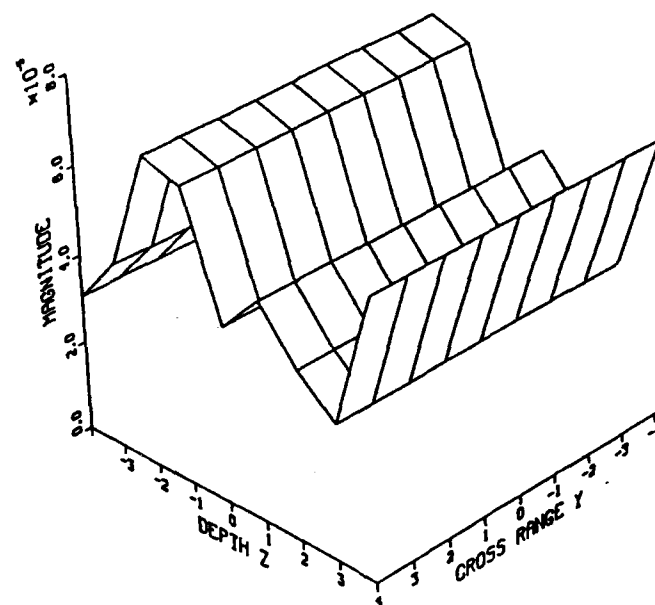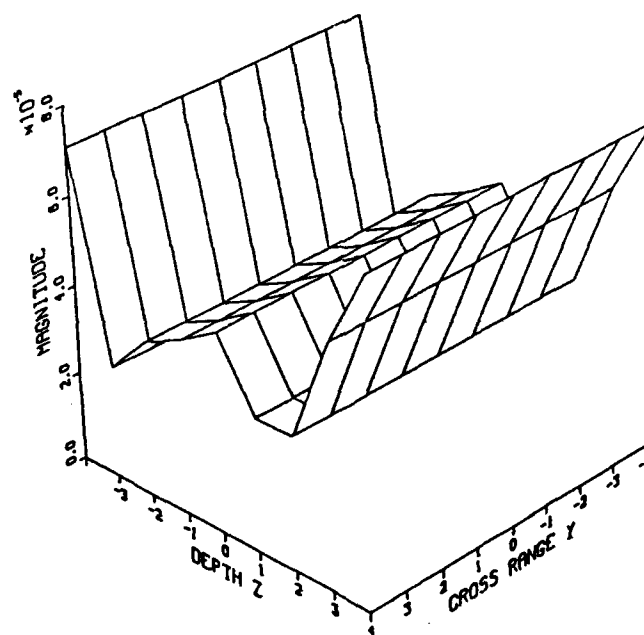
60

TRANSMITTED PULSE

CASE:FLUID
WAVEFORM:HAMMING-ENVELOPE LFM PULSE (NFREQ:151)
A: 10.0 TP: 100.0 MSEC PRF: 0.8 HZ FC: 250.0 HZ SWPTBW: 80.0 HZ CHIRP:U
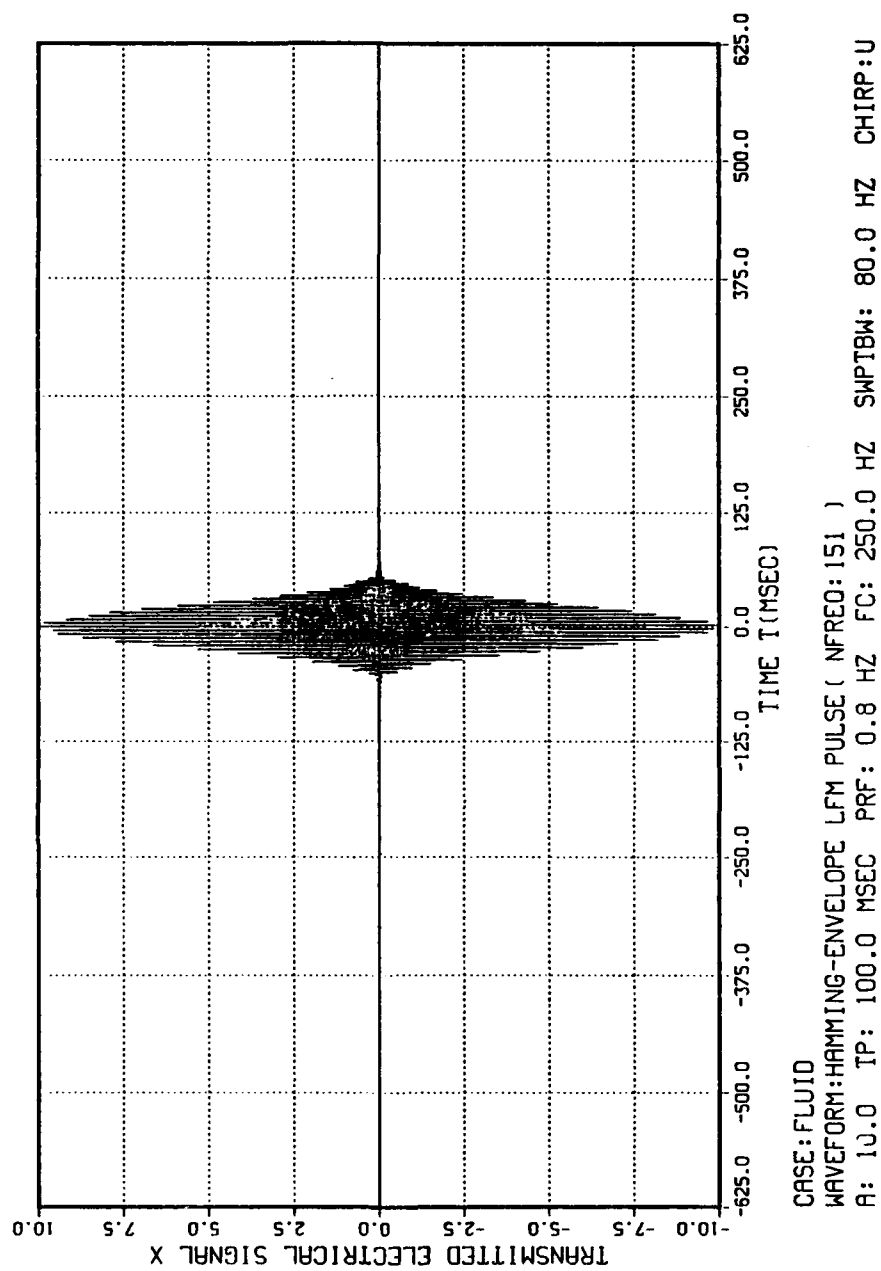
Figure 3.28 Hamming-envelope LFM pulse ($f_0 = 0.8$ Hz).

61

CASE:FLUID   FREQUENCY: 250.0 HZ

ZT: 30.0 M   XR: 10000.0 M   YR: 0.0 M   ZR: 20.0 M

(a)

CASE:FLUID   FREQUENCY: 250.0 HZ

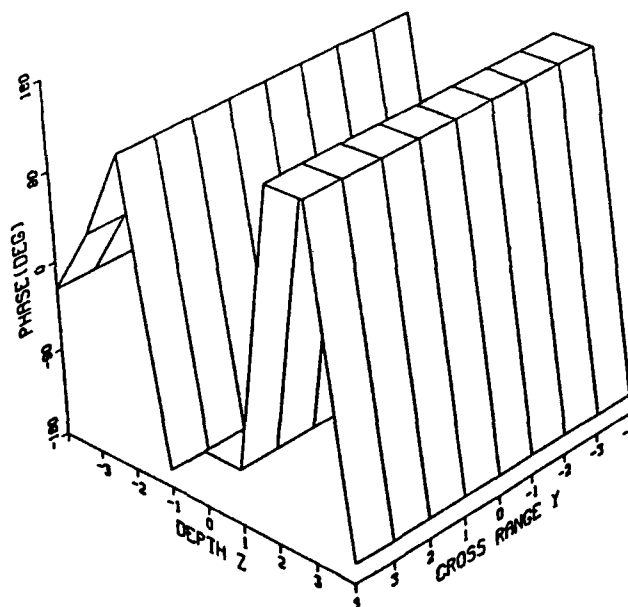ZT: 30.0 M   XR: 10000.0 M   YR: 0.0 M   ZR: 80.0 M

(b)

Figure 3.29 Fluid bottom: Magnitude of the complex acoustic pressure field for Hamming-envelope LFM pulse for (a) receiver above the source and (b) receiver below the source.

62

CASE: FLUID   FREQUENCY: 250.0 HZ

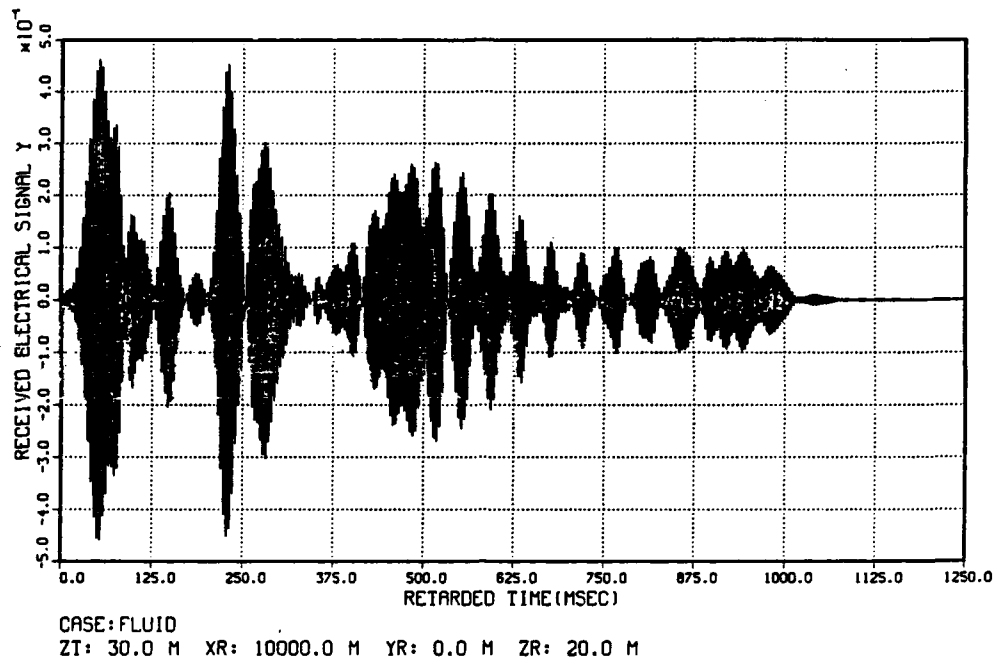ZT: 30.0 M   XR: 10000.0 M   YR: 0.0 M   ZR: 20.0 M

(a)
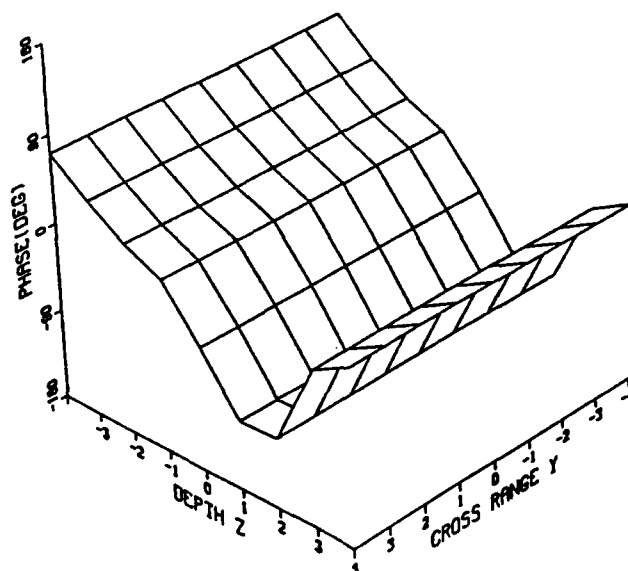
CASE: FLUID   FREQUENCY: 250.0 HZ
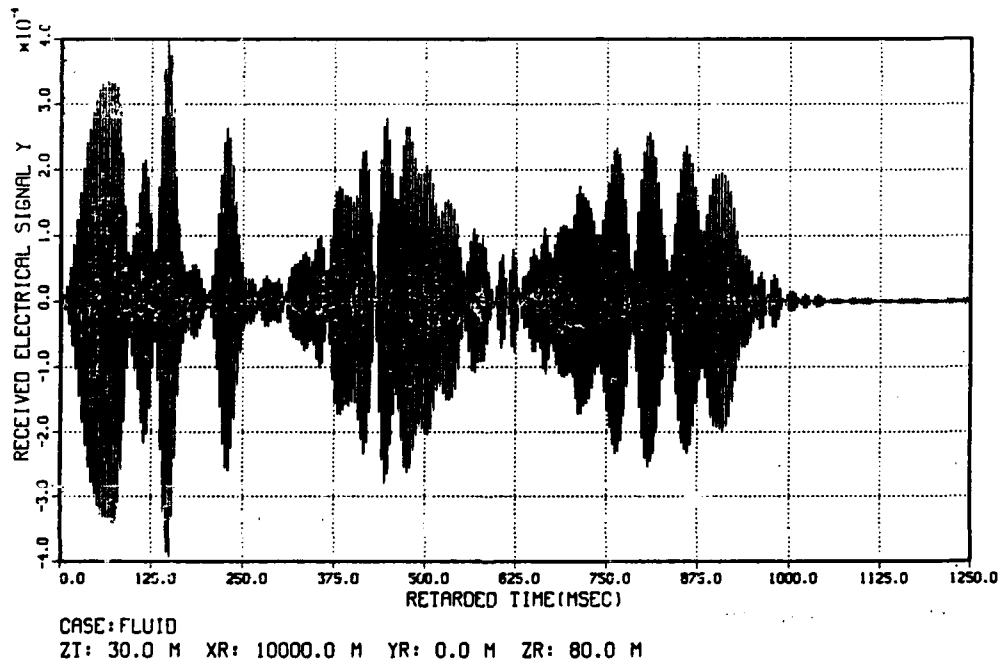
ZT: 30.0 M   XR: 10000.0 M   YR: 0.0 M   ZR: 80.0 M

(b)

Figure 3.30 Fluid bottom: Phase of the complex acoustic pressure field for Hamming-envelope LFM pulse for (a) receiver above the source and (b) receiver below the source.

63

CASE: FLUID
ZT: 30.0 M   XR: 10000.0 M   YR: 0.0 M   ZR: 20.0 M

(a)

CASE: FLUID
ZT: 30.0 M   XR: 10000.0 M   YR: 0.0 M   ZR: 80.0 M

(b)

Figure 3.31 Fluid bottom: Output signal for Hamming-envelope LFM pulse ($f_0 = 0.8$ Hz) for (a) receiver above the source and (b) receiver below the source.

the amplitude of the output time-domain electrical signal depends on the range where the receiver was placed, that is, the amplitude of the output signal in the long range case is smaller compared to the short range case for each model and for the same transmitted electrical signal.

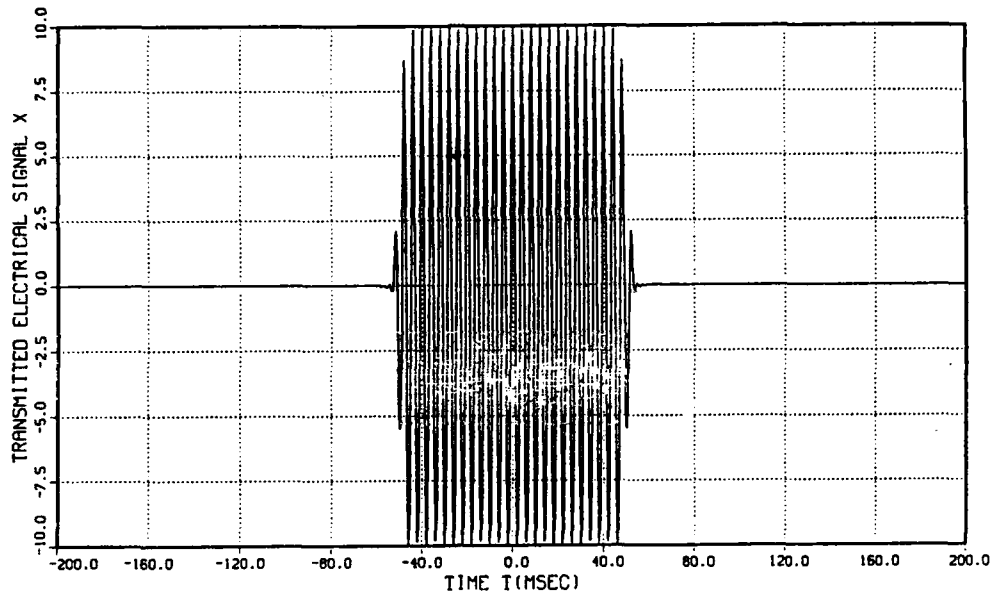## B. RECTANGULAR-ENVELOPE

1. Continuous-wave (CW) pulse

The transmitted electrical signal is a rectangular-envelope CW pulse with Lanczos smoothing and it is shown in Fig. 3.32 for $f_0 = 2.5$ Hz and $f_0 = 0.8$ Hz. These pulses have the same parameter values as with the Hamming-envelope CW pulses shown in Figs. 3.9 and 3.16. It is shown in Fig. 3.32 that for both pulses, more harmonics are required compared to the Hamming-envelope CW pulses. This is due to the discontinuities at the beginning and the end of the rectangular envelope and, therefore, more harmonics are needed in order to represent the pulse accurately.

The propagation of this pulse is investigated using the fluid bottom model for the long range case. The long range case was chosen since this case is generally more realistic and more interesting from an application point of view than the short range case. As in the previous section, the receiver is located at two different depths, i.e., above and below the source. In order to be able to observe the overall received electrical signal, the pulse is transmitted over the fundamental period $T_0 = 1/f_0 = 1/0.8 = 1250$ msec.
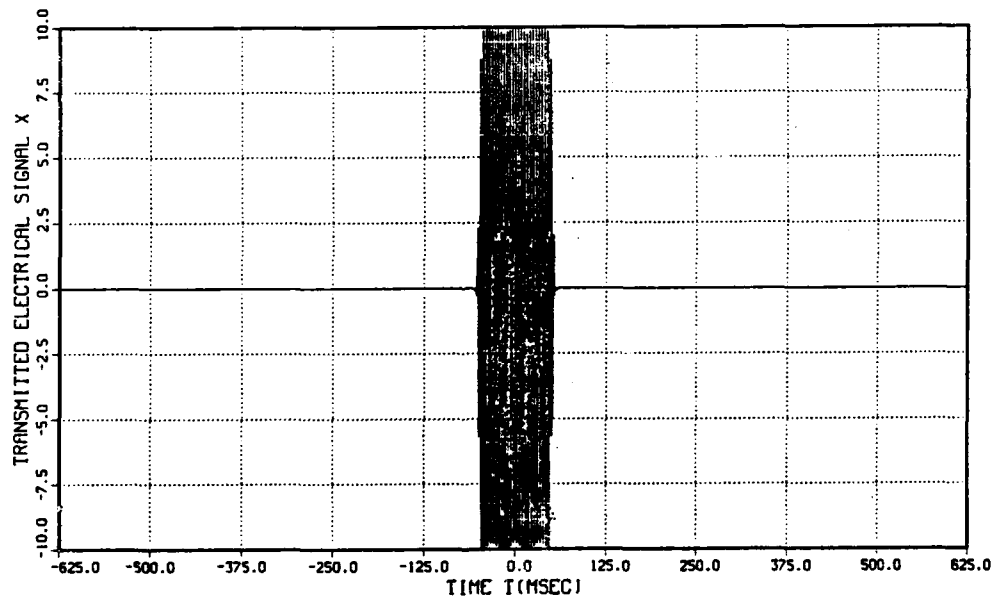
The complex acoustic pressure field (magnitude and phase) across the receive array for the carrier frequency and for both receiver depths is shown in Figs. 3.33 and 3.34. The 3-D plots show how the magnitude and phase of the acoustic pressure changes, over the array elements when the depth of the receiver changes.

The resulting output electrical signal at the center element of the array for
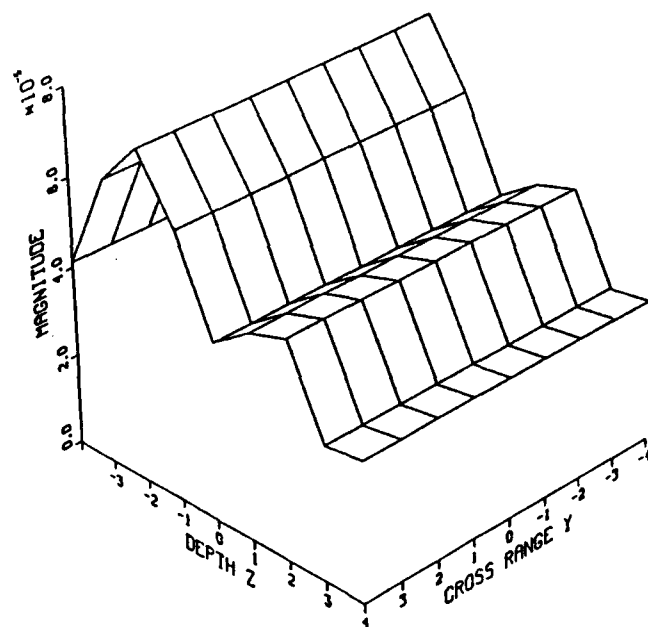
TRANSMITTED PULSE

CASE: FLUID
WAVEFORM: RECTANGULAR-ENVELOPE CW PULSE WITH LANCZOS SMOOTHING (NFREQ: 129)
A: 10.0   TP: 100.0 MSEC   PRF: 2.5 HZ   FC: 250.0 HZ

(a)

CASE: FLUID
WAVEFORM: RECTANGULAR-ENVELOPE CW PULSE WITH LANCZOS SMOOTHING (NFREQ: 401)
A: 10.0   TP: 100.0 MSEC   PRF: 0.8 HZ   FC: 250.0 HZ

(b)

Figure 3.32 Rectangular-envelope CW pulses: (a) $f_0 = 2.5$ Hz and (b) $f_0 = 0.8$ Hz.

66

CASE:FLUID   FREQUENCY: 250.0 HZ

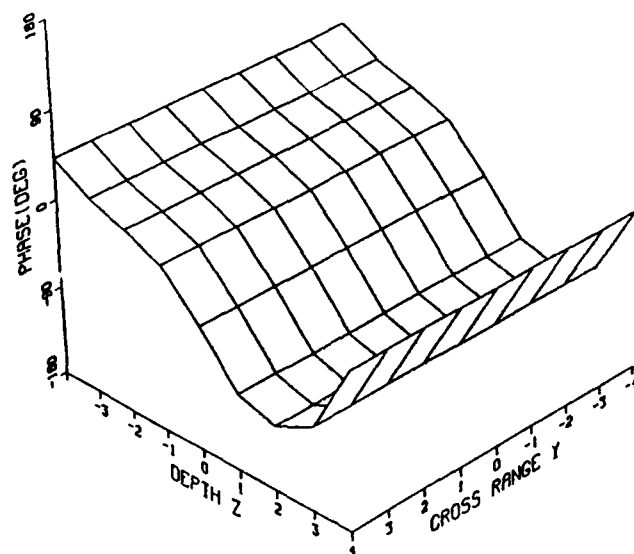ZT: 30.0 M   XR: 10000.0 M   YR: 0.0 M   ZR: 20.0 M

(a)
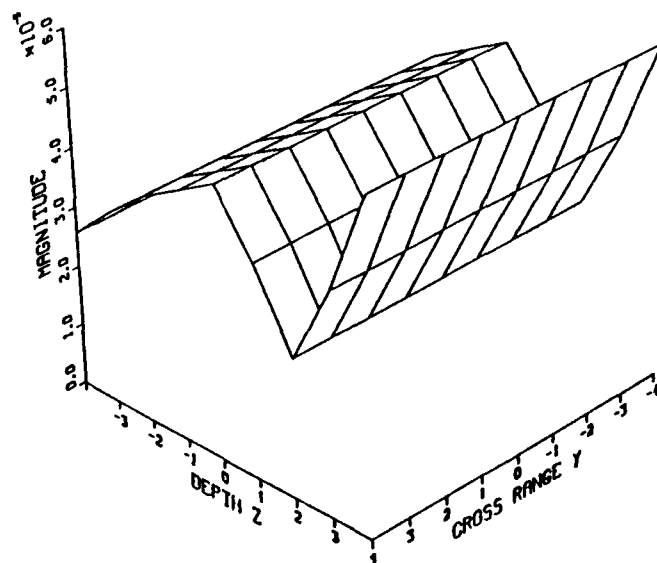
CASE:FLUID   FREQUENCY: 250.0 HZ
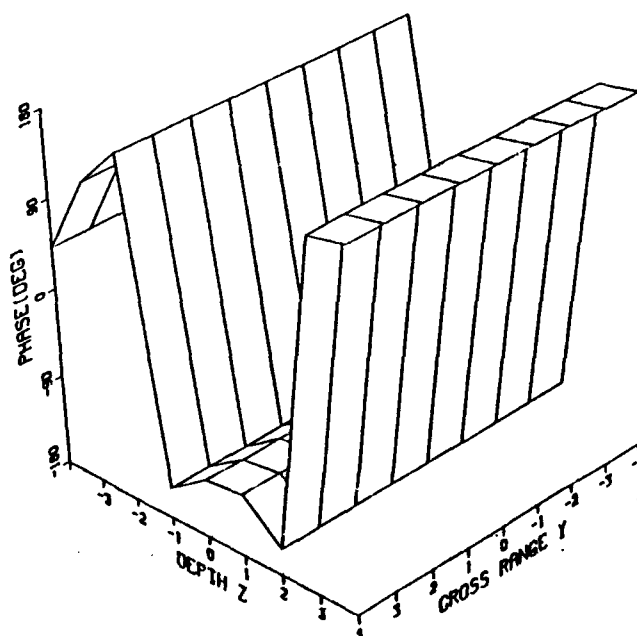
ZT: 30.0 M   XR: 10000.0 M   YR: 0.0 M   ZR: 80.0 M

(b)

Figure 3.33 Fluid bottom: Magnitude of the complex acoustic pressure field for rectangular-envelope CW pulse for (a) receiver above the source and (b) receiver below the source.

67

CASE:FLUID   FREQUENCY: 250.0 HZ

ZT: 30.0 M XR: 10000.0 M YR: 0.0 M ZR: 20.0 M

(a)

CASE:FLUID   FREQUENCY: 250.0 HZ

ZT: 30.0 M XR: 10000.0 M YR: 0.0 M ZR: 80.0 M

(b)

Figure 3.34 Fluid bottom: Phase of the complex acoustic pressure field for rectangular-envelope CW pulse for (a) receiver above the source and (b) receiver below the source.

68

the two receiver depths is shown in Fig. 3.35. As for the Hamming-envelope case, the duration of the output pulse is approximately 1000 msec long, due to dispersion effects. It is also observed that the shape of the received pulse depends greatly on the depth of the receiver.

2. Linear-frequency-modulated (LFM) pulse

The rectangular-envelope LFM pulses with Lanczos smoothing for $f_0 = 2.5$ Hz and $f_0 = 0.8$ Hz are shown in Fig. 3.36. A LFM pulse requires more harmonics in order to represent its complex envelope compared to a CW pulse.

The long range case was also chosen in order to present the performance of the fluid bottom model. The transmitted pulse has a fundamental frequency of $f_0 = 0.8$ msec. The complex acoustic pressure field (magnitude and phase) across the receive array for the carrier frequency and for both receiver depths is shown in Fig. 3.37 and 3.38. The resulting output electrical signal at the center element of the array for the two receiver depths is shown in Fig. 3.39.

The performance of the fluid bottom model under the propagation of the rectangular-envelope CW and LFM pulses for the long range case has been examined in this section. Based on the computer simulation results, the conclusions are (i) the rectangular-envelope function is more complicated to simulate than the Hamming-envelope since more harmonics must be included, (ii) the shape of the complex acoustic pressure field across the receive array and the output electrical signal are affected greatly by the depth of the receiver, and (iii) the CW pulse has been easier to simulate since less computer memory space and computation time are required.
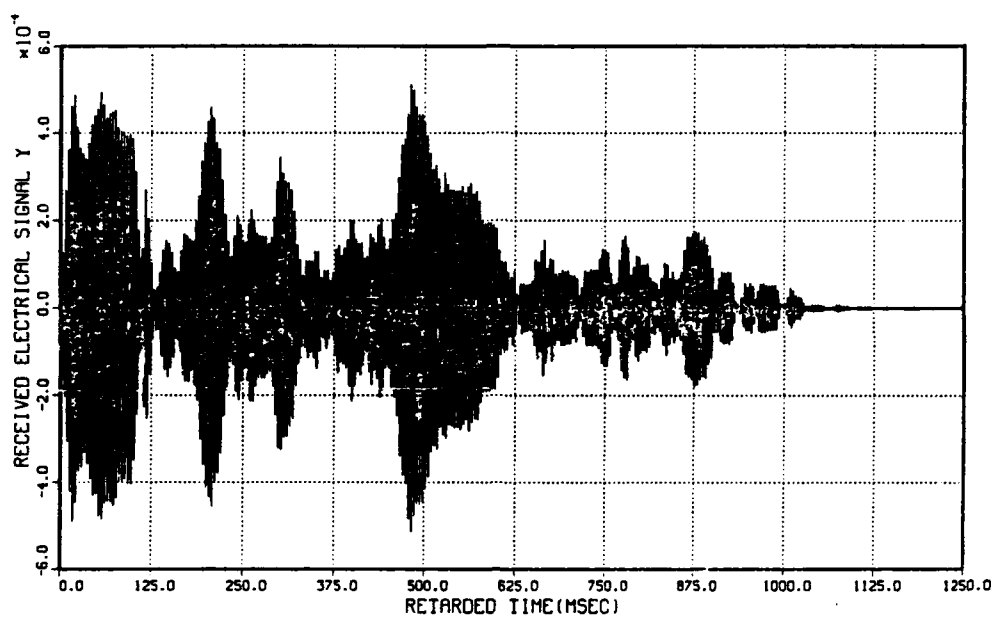
CASE:FLUID
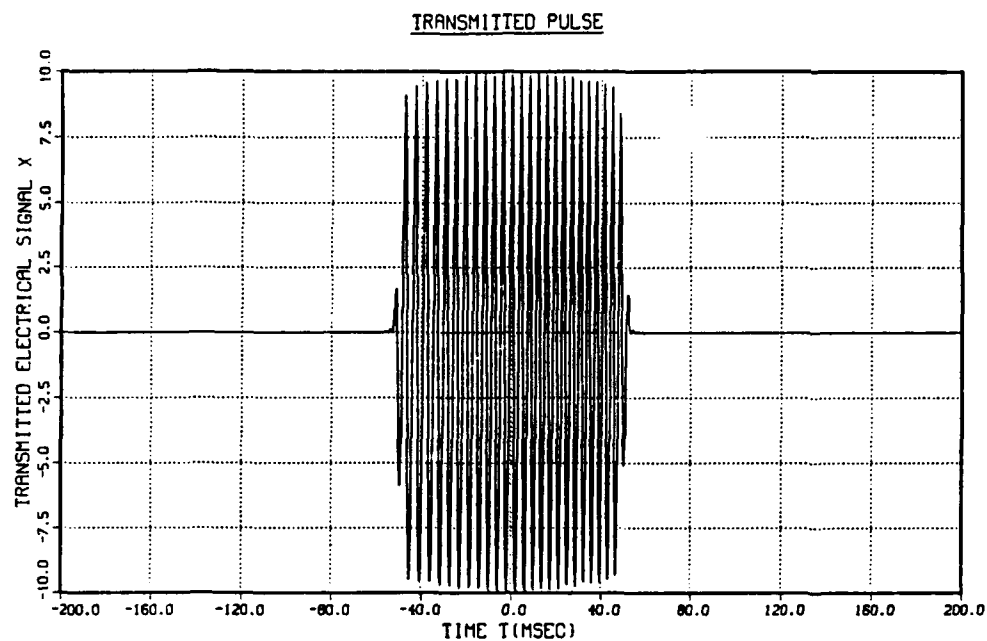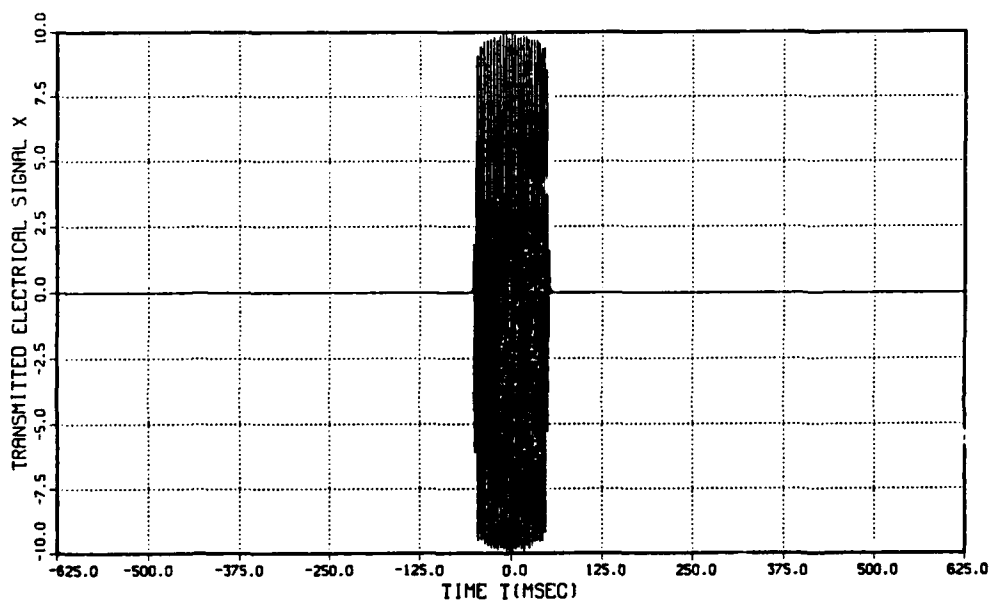ZT: 30.0 M   XR: 10000.0 M   YR: 0.0 M   ZR: 20.0 M

(a)
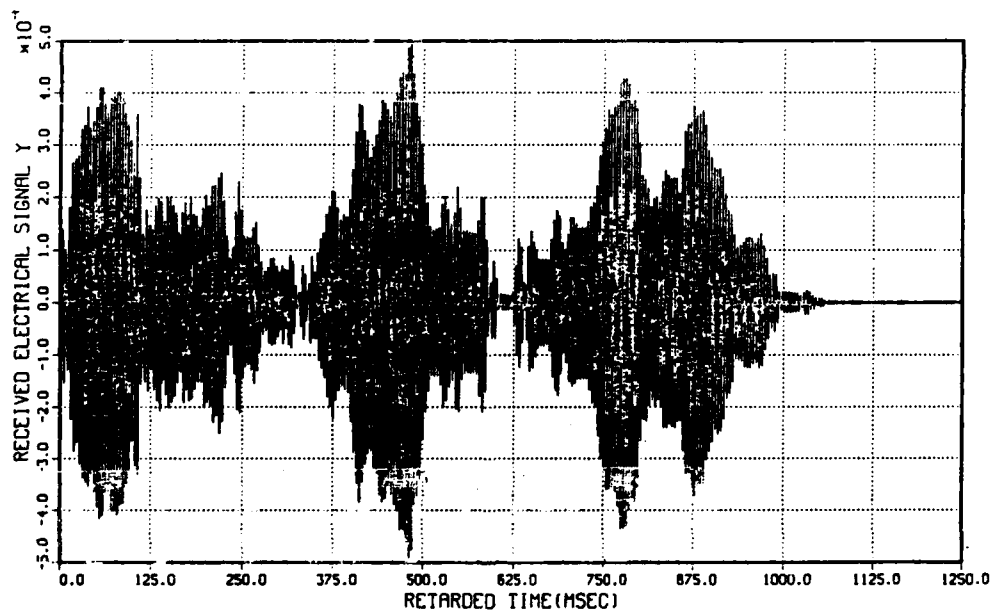
CASE:FLUID
ZT: 30.0 M   XR: 10000.0 M   YR: 0.0 M   ZR: 80.0 M

(b)

Figure 3.35 Fluid bottom: Output signal for rectangular-envelope CW pulse ($f_0 = 0.8$ Hz) for (a) receiver above the source and (b) receiver below the source.

70

CASE:FLUID
WAVEFORM:RECTANGULAR-ENVELOPE LFM PULSE WITH LANCZOS SMOOTHING(NFREQ:161)
A: 10.0   TP: 100.0 MSEC   PRF: 2.5 HZ   FC: 250.0 HZ   SWPTBW: 80.0 HZ   CHIRP:U

(a)

CASE:FLUID
WAVEFORM:RECTANGULAR-ENVELOPE LFM PULSE WITH LANCZOS SMOOTHING(NFREQ:501)
A: 10.0   TP: 100.0 MSEC   PRF: 0.8 HZ   FC: 250.0 HZ   SWPTBW: 80.0 HZ   CHIRP:U
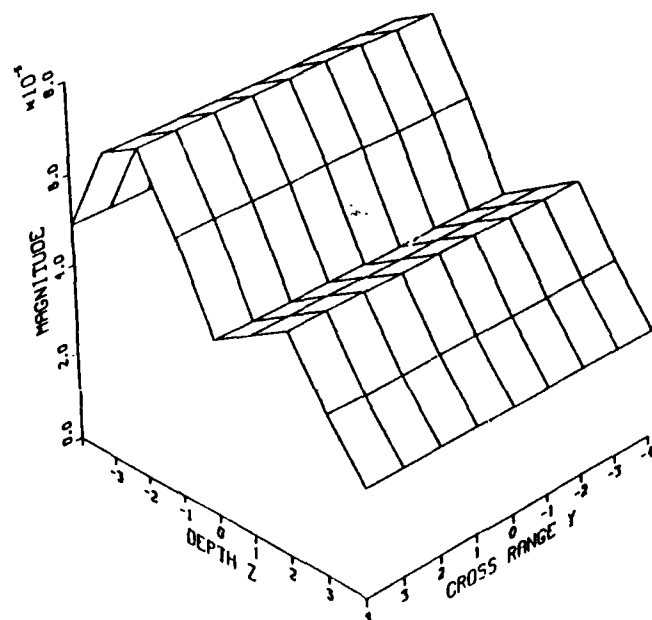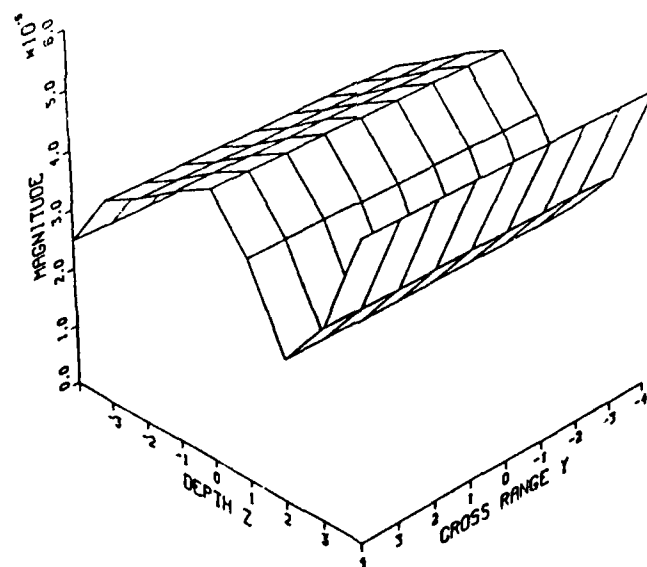
(b)

Figure 3.36 Rectangular-envelope LFM pulses: (a) $f_0 = 2.5$ Hz and (b) $f_0 = 0.8$ Hz.

71

CASE:FLUID   FREQUENCY: 250.0 HZ

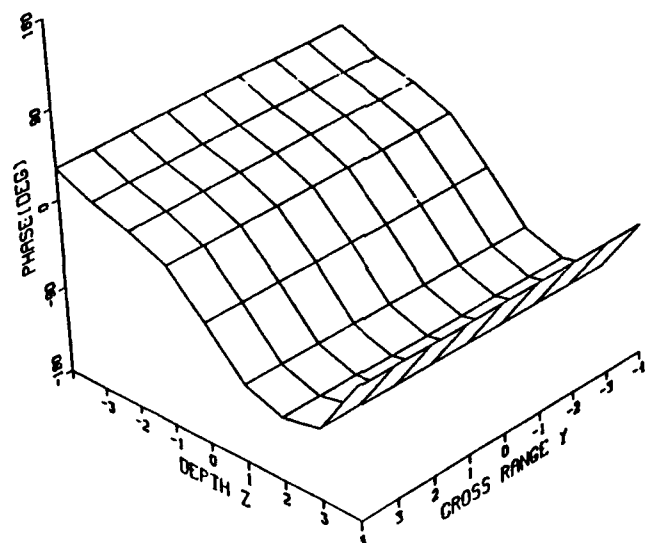ZT: 30.0 M   XR: 10000.0 M   YR: 0.0 M   ZR: 20.0 M

(a)

CASE:FLUID   FREQUENCY: 250.0 HZ

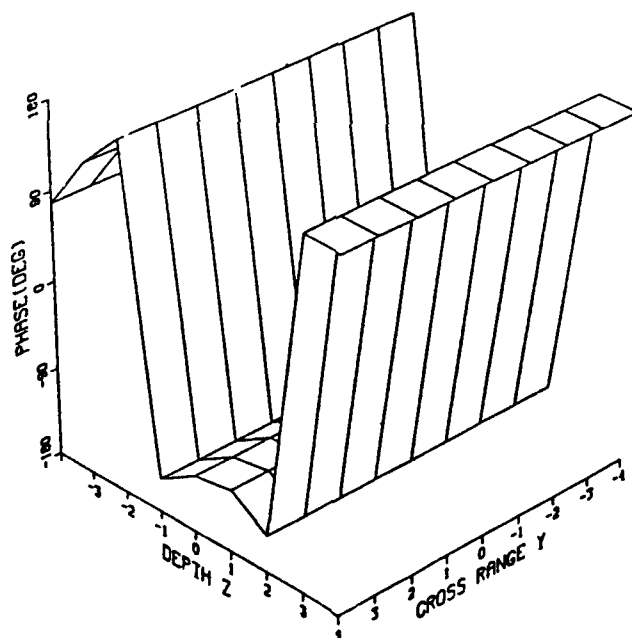ZT: 30.0 M   XR: 10000.0 M   YR: 0.0 M   ZR: 80.0 M

(b)

Figure 3.37 Fluid bottom: Magnitude of the complex acoustic pressure
field for rectangular-envelope LFM pulse for (a) receiver above the source
and (b) receiver below the source.

72

CASE:FLUID   FREQUENCY: 250.0 HZ

ZT: 30.0 M XR: 10000.0 M YR: 0.0 M ZR: 20.0 M

(a)

CASE:FLUID   FREQUENCY: 250.0 HZ

ZT: 30.0 M XR: 10000.0 M YR: 0.0 M ZR: 80.0 M

(b)

Figure 3.38 Fluid bottom: Phase of the complex acoustic pressure field for rectangular-envelope LFM pulse for (a) receiver above the source and (b) receiver below the source.

73

CASE: FLUID
ZT: 30.0 M   XR: 10000.0 M   YR: 0.0 M   ZR: 20.0 M

(a)

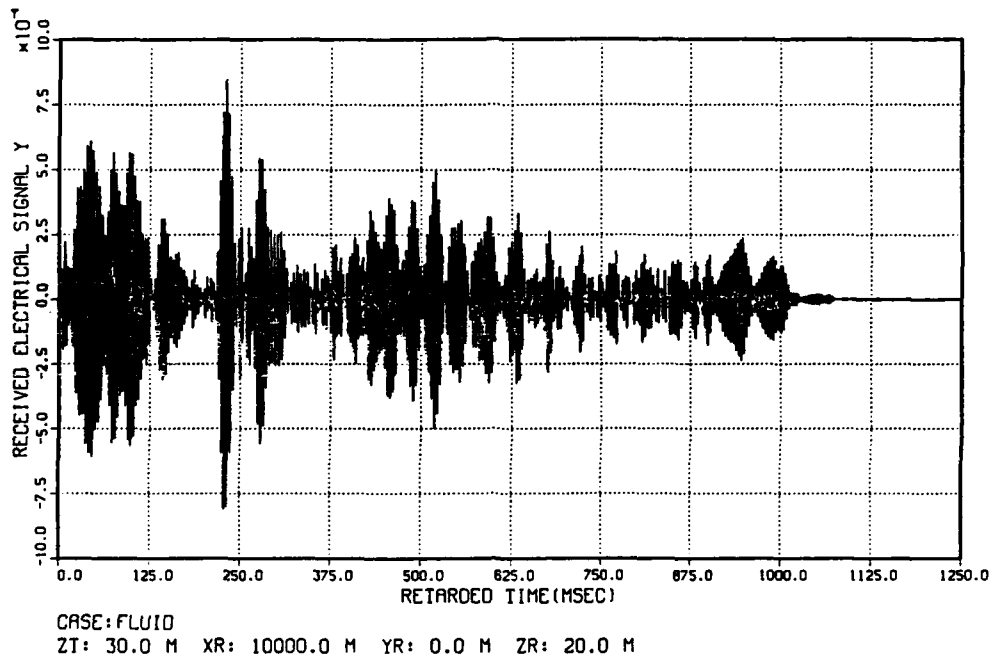CASE: FLUID
ZT: 30.0 M   XR: 10000.0 M   YR: 0.0 M   ZR: 80.0 M
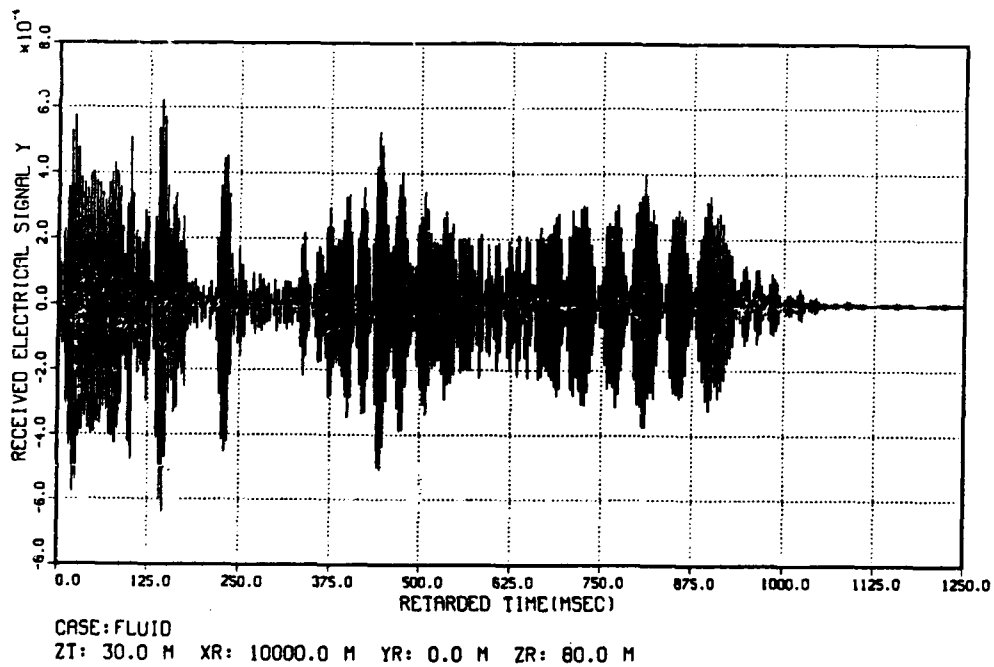
(b)

Figure 3.39 Fluid bottom: Output signal for rectangular-envelope LFM pulse (f_0 = 0.8 Hz) for (a) receiver above the source and (b) receiver below the source.

74

IV. CONCLUSIONS AND RECOMMENDATIONS

The pressure-release surface with a rigid bottom model is a simple ocean waveguide model from an analytical point of view. The mathematical equations of this model are not complicated and they have been relatively easy to program. However, it is well known that this model is not realistic since the rigid bottom assumption is not valid. Also, the computer simulation results of the model have shown that the model is not easily simulated since an extremely large memory area and long computation time are required. The reason is that many normal modes are allowed to propagate. Typically, the number of allowed propagating modes in the rigid bottom model are about twice as many as the the number of trapped modes allowed to propagate in the more realistic fluid bottom model using the same transmitted electrical signal. Therefore, the rigid bottom model simulation results are, in general, unrealistic, since due to the dispersion effects, the duration of the resulting output pulse at the receiver is more than 100 times longer than the transmitted pulse.

The fluid bottom model is more complicated from an analytical point of view since the transcendental equation (Eq. 2–14) is involved. The roots of the transcendental equation must be numerically calculated in order to simulate the model by a computer program. It was known that this model is a more realistic one, compared to the rigid bottom model. The computer simulation results have verified that it performs much more accurately and correctly, than the rigid bottom model [Ref. 8]. Also, the fluid bottom model is easier to implement without extreme memory space and long computation time requirements.

The pulse propagation computer simulation program which has been used to

75

investigate the two models is able to simulate a variety of commonly used envelope functions, such as the (i) rectangular-envelope, (ii) rectangular-envelope with Lanczos smoothing, (iii) Hamming-envelope, and (iv) Hanning-envelope. In this thesis, we have chosen to present the results of the test cases using envelope functions (ii) and (iii) only, as the representative cases from the whole group. The other envelope functions have been tested also and they perform effectively.

It is recommended that no further research work be done on the rigid bottom ocean waveguide model since it is not a very realistic model. However, research work should continue on the fluid bottom ocean waveguide model. For example, work should continue on incorporating the effects of attenuation (sound absorption) and arbitrary sound-speed profiles into the model.

REFERENCES

1. C. S. Clay and H. Medwin, *Acoustical Oceanography*, Wiley, New York, 1977, pp. 288-317.

2. L. E. Kinsler, A. R. Frey, A. B. Coppens, and J. V. Sanders, *Fundamentals of Acoustics*, Wiley, New York, 1982, pp. 430-440.

3. L. J. Ziomek, course notes for EC3450, Acoustic Field Theory, Naval Postgraduate School, Monterey, CA.

4. M. B. Porter, R. L. Dicus, and R. G. Fizell, "Simulations of matched-field processing in a deep-water Pacific environment", *IEEE J. Oceanic Engr.*, Vol. OE-12, 173-181 (1987).

5. A. B. Baggeroer, W. A. Kuperman, and H. Schmidt, "Matched-field processing : Source localization in correlated noise as an optimum parameter estimation problem", *J. Acoust. Soc. Am.*, Vol. 83, 571-587 (1988).

6. Campbell, Peter R. M., Master's Thesis, Naval Postgraduate School, Monterey, CA, June 1989.

7. L. J. Ziomek, *Underwater Acoustics*, Academic Press, Orlando, FL, 1985.

8. L. J. Ziomek, L. A. Souza, and P. R. Campbell, "Pulse propagation in a random ocean – A linear systems theory approach", *OCEANS '89*, September 18-21, 1989, Seattle, Washington USA, pp. 1211-1216.

INITIAL DISTRIBUTION LIST

		No. of Copies
1.	Defense Technical Information Center Cameron Station Alexandria, Virginia 22304-6145	2
2.	Library, Code 0142 Naval Postgraduate School Monterey, California 93943-5002	2
3.	Chairman, Code 62 Department of Electrical and Computer Engineering Naval Postgraduate School Monterey, California 93943-5000	1
4.	Prof. L. J. Ziomek, Code 62Zm Department of Electrical and Computer Engineering Naval Postgraduate School Monterey, California 93943-5000	3
5.	Prof. H-M. Lee, Code 62Lh Department of Electrical and Computer Engineering Naval Postgraduate School Monterey, California 93943-5000	1
6.	Dr. Marshall Orr, Code 1125OA Office of Naval Research 800 N. Quincy St. Arlington, VA 22217	1
7.	Hellenic Navy GEN/B2-III Stratopedo Papagou Holargos Athens, Greece	3

8. Lt. Marinos P. Markopoulos   2
    78 Athinodorou
    K. Helioupolis
    16341 Athens, Greece